UC San Diego

UC San Diego Electronic Theses and Dissertations

Title

Leveraging spaceborne and airborne lidar to characterize the morphology and evolution of eroding Arctic coasts in a changing climate

Permalink

https://escholarship.org/uc/item/5cp43226

ISBN

9798173720870

Author

Bryant, Marnie

Publication Date

2026-10-30

Peer reviewed|Thesis/dissertation

eScholarship.org Powered by the California Digital Library
University of California

UNIVERSITY OF CALIFORNIA SAN DIEGO

Leveraging spaceborne and airborne lidar to characterize the morphology and evolution of eroding Arctic coasts in a changing climate

A dissertation submitted in partial satisfaction of the
requirements for the degree Doctor of Philosophy

in

Earth Sciences

by

Marnie Bryant

Committee in charge:

Adrian Borsa, Chair
Ian Eisenman
Helen Amanda Fricker
Armin Schwartzman
Adam Young

2026

Copyright

Marnie Bryant, 2026

All rights reserved.

The Dissertation of Marnie Bryant is approved, and it is acceptable in quality and form for publication on microfilm and electronically.

University of California San Diego

2026

EPIGRAPH

It is important to draw wisdom from many different places. If we take it from only one place, it becomes rigid and stale.

-Uncle Iroh, *Avatar the Last Airbender*

TABLE OF CONTENTS

Dissertation Approval Page iii

Epigraph iv

Table of Contents v

List of Figures viii

List of Tables xii

Acknowledgements xiii

Vita xv

Abstract of the Dissertation xvi

Chapter 1 Introduction 1
1.1 Motivation 1
1.2 Drivers of Arctic shoreline change 3
1.3 Quantifying shoreline morphology and change with elevation data 4
1.4 Research objectives 5
1.5 Acknowledgments 6

References 8

Chapter 2 Multiple modes of shoreline change along the Alaskan Beaufort Sea observed using ICESat-2 altimetry and satellite imagery 11
2.1 Introduction 12
2.2 Data and Methods 14
2.2.1 Study Area 14
2.2.2 Time-varying environmental conditions 16
2.2.3 Shoreline identification from satellite multispectral imagery 17
2.2.4 Elevation profiles from ICESat-2 altimetry 19
2.3 Results 23
2.3.1 Environmental conditions 23
2.3.2 Imagery-derived shoreline position and retreat rates 24
2.3.3 Cross-validation of ICESat-2 altimetry and Planet imagery-derived shoreline positions 27
2.3.4 Topographic change from satellite altimetry 28
2.4 Discussion 33
2.4.1 Spatiotemporal variability in shoreline change in the context of previous observations 33
2.4.2 Drivers of spatiotemporal variability in imagery-derived shoreline change . 34
2.4.3 Drivers of morphologic change observed from ICESat-2 altimetry 35

2.4.4 Potential and challenges using ICESat-2 for shoreline characterization 38
2.5 Conclusions 39
2.6 Code and Data Availability 41
2.7 Author contributions 41
2.8 Competing interests 42
2.9 Acknowledgements 42
2.10 Supplementary material 43

References 50

Chapter 3 Unsupervised classification of topographic shores type from airborne lidar in the East Chukchi Sea 55
3.1 Introduction 56
3.2 Data and Methods 58
3.2.1 Study area 58
3.2.2 Elevation transect generation and processing 58
3.2.3 Clustering 64
3.3 Results 72
3.3.1 Functional clustering 72
3.3.2 Parameter Clusters 73
3.3.3 Unrepresented Features 80
3.4 Discussion 81
3.4.1 Physical interpretation of clusters 81
3.4.2 Spatial distribution of clusters 81
3.4.3 Subjective choices in the classification method and opportunities for improvement 82
3.5 Conclusions 83
3.6 Acknowledgments 84
3.7 Supplementary Figures 85

References 86

Chapter 4 Variations in shoreline change between shore types on the East Chukchi Sea . 89
4.1 Introduction 90
4.2 Data and Methods 92
4.2.1 Historical shoreline change rates 92
4.2.2 Meteorological datasets 93
4.2.3 Shoreline composition from ShoreZone 96
4.2.4 Comparing rates between shore types 97
4.3 Results 99
4.3.1 Overview of shoreline change rates 99
4.3.2 Historic meteorological conditions 99
4.3.3 Shoreline composition 103
4.3.4 Shoreline change across different shore types 105
4.4 Discussion 112

4.4.1 Meteorological drivers of large-scale variations in shoreline change 112
4.4.2 Variations in shoreline change rates between topographic classes 114
4.5 Conclusion 116
4.6 Acknowledgments 117
4.7 Supplementary material 118

References 120

Chapter 5 Conclusions 123
5.1 Summary of findings 123
5.2 Looking forward: large-scale morphologic monitoring from space 124
5.3 Closing remarks 126

LIST OF FIGURES

Figure 1.1: The primary mechanisms and consequences of Arctic coastal erosion, from Fritz et al. (2017) 2

Figure 1.2: Pan-Alaskan permafrost presence (from Jorgenson (2022)) and shoreline change rates in Northern Alaska (from Gibbs et al. (2024)). The study sites covered in this dissertation are marked. 6

Figure 2.1: Overview of the Study Area on the Alaskan Beaufort Sea Coast 14

Figure 2.2: Planet Labs imagery (©2024 Planet Labs Inc) used to estimate shoreline positions. Shorelines delineated using Otsu thresholding are overlain and show good agreement with the visible land-water boundary. 20

Figure 2.3: Shorelines derived from Planet images, overlain on imagery from 07/25/2020 (©2024 Planet Labs Inc). The locations of the three ICESat-2 ground tracks are also shown. 26

Figure 2.4: Time series of the position of upper and lower boundaries and coastal boundaries from ICESat-2 and the land-water boundary derived from Planet. 27

Figure 2.5: Comparison between shoreline change estimates from Planet and shoreline change estimates from the upper and lower boundaries derived from ICESat-2 28

Figure 2.6: Detailed view of the ICESat-2 sampling location from 2018 satellite imagery (©2024 Google Earth CNES/Airbus) and ICESat-2 elevation data for each sampling site 29

Figure 2.7: ICESat-2 ATL03 photon data show small-scale features, including (a) returns over what may be a toppled block material at the base of the bluff at ground track 3r and (b) Surface ponding in the drained lake basin at ground track 2r. 32

Figure 2.8: Normalized distribution of scene-wide NDWI values for Planet images 43

Figure 2.9: Illustration of the boundaries and elevation estimates described in Section 2.4 43

Figure 2.10: RMS error between our SlideRule-derived elevations and the source ATL03 photon information for ground track 3r 44

Figure 2.11: RMS error between our SlideRule-derived elevations and the source ATL03 photon information for ground track 2r 45

Figure 2.12: RMS error between our SlideRule-derived elevations and the source ATL03 photon information for ground track 1r 46

Figure 2.13: 2007 aerial photography from NOAA ShoreZone (Harper and Morris, 2014) captured near the sites our ICESat-2 ground tracks 47

Figure 2.14: Long and short-term regional shoreline change rates along the Alaskan Beaufort Sea Coast near Drew point from previous work, along with the 3-year and year-to-year regional rates derived in this work 48

Figure 3.1: An overview of the study area and elevation data on the northwestern coast of Alaska 59

Figure 3.2: An example of how the local sea_slope and $land_slope$ variables are calculated for a given point x_i 60

Figure 3.3: Our estimated W (a)) and H (b) parameters were smoothed alongshore, and outliers were removed. 64

Figure 3.4: Profiles were smoothed and then decomposed into two components: normalized functions and scaling parameters 65

Figure 3.5: An example of functional alignment. a: $\hat{h}_2$ is aligned to $\hat{h}_1$ by warping its domain using the warping function $\gamma(x)$ (b) 66

Figure 3.6: The FDASRSF workflow. 67

Figure 3.7: Distribution of silhouette scores for different cluster numbers for the form clustering. The median of each cluster and the overall median of the dataset is shown. 73

Figure 3.8: The final form clusters. Top: The center of each cluster and aligned normalized profiles. Bottom: The original profiles corresponding to each cluster 74

Figure 3.9: Map of the final transects labeled according to their a) form class and b) parameter class. The locations of the features shown in Figure 3.17 are indicated 74

Figure 3.10: Size distribution of along-shore units corresponding to each form cluster . . . 75

Figure 3.11: The distribution of silhouette scores for increasing k values for the parameter clustering step for each form cluster. The median of each cluster and the overall median of the dataset is shown 76

Figure 3.12: The distribution of parameters and their corresponding parameter cluster label for each form cluster. 76

Figure 3.13: The transects corresponding to the parameter clusters for Form cluster 0 77

Figure 3.14: Along-shore unit size distribution for the parameter clusters in Form Cluster 0 77

Figure 3.15: transects corresponding to the parameter clusters for Form Cluster 1 78

Figure 3.16: Along-shore unit size distribution for the parameter clusters in Form Cluster 1 79

Figure 3.17: Notable features not represented in our classification 80

Figure 3.18: The median silhouette score as a function of k for the 10 sets of seeds tested. The seed set with the maximum score for each k was used for the final evaluation in Figure 3.7 85

Figure 3.19: The distribution of parameters for Form Cluster 1 when split into 3 parameter clusters. 85

Figure 4.1: An overview of our study area with historical shoreline change rates from Gibbs et al. (2024). The location of the 5-m isobath where the wave model from Engelstad et al. (2024b) was generated is shown. 91

Figure 4.2: Historic retreat rates from USGS (Gibbs et al., 2024) and their measurement errors 99

Figure 4.3: Alongshore distribution of 30-year statistics from CARRA2 100

Figure 4.4: The characteristic wave field estimated from the USGS DWDB 101

Figure 4.5: Summary of metrics derived from the USGS downscaled wave database 102

Figure 4.6: Mean summer temperature (a) and rainfall (b) averaged from June 1st-October 31st average over 1980-2010. c) The shoreline change rates are plotted for comparison. 104

Figure 4.7: The primary material types of a) the supratidal zone and b) the intertidal zone. Historic shoreline change rates from USGS are also plotted for reference. . . . 105

Figure 4.8: The full material types of a) the supratidal zone and b) the intertidal zone. See table 4.2 for the letter code definitions. Historic shoreline change rates from USGS are also plotted for reference. 106

Figure 4.9: Permafrost presence from ShoreZone for a) the supratidal and b) the intertidal zone. Historic shoreline change rates from USGS are also plotted for reference. 107

Figure 4.10: The distribution of shoreline change rates for transects classified as a) Form Class 0 and b) Form class 1. The number of sampled transects and median for each class is shown. 107

Figure 4.11: Comparisons of the distribution of shoreline change rates across both classes with the KS test statistic and p-value for a) the original distributions and b) the distributions after removing the median. 108

Figure 4.12: The estimated median shoreline change rates and their propagated uncertainties for a) The form classes and b) the parameter classes. The standard deviation (σ) and 95% confidence interval are shown. 109

Figure 4.13: Shoreline change rate distributions across our parameter classes. The number of sampled transects and median for each class is shown. 109

Figure 4.14: Pairwise comparisons of shoreline change rates between different parameter classes. The p-value from a 2-sample KS test (modified using Bonferroni correction) is shown. Pairs with significantly low p-values are highlighted. . . 110

Figure 4.15: Pairwise comparisons of shoreline change rates between different parameter classes after removing their medians. 111

Figure 4.16: Along-shore shoreline change rates overlain over our a) form classes and b) parameter classes. 113

Figure 4.17: Inputs used for the USGS Downscaled Wave Database 118

Figure 4.18: An overview of the cross-shore segmentation from ShoreZone 119

Figure 4.19: The relative fraction of the shoreline that is composed of each sediment class in a) the supratidal zone and b) the intertidal zone. 119

Figure 5.1: EDGE's dense sampling transforms observations of permafrost-driven shoreline erosion events, offering new insight into the processes behind these high-impact, episodic events. 125

LIST OF TABLES

Table 2.1. Observation intervals from Planet imagery and ICESat-2. The number of open water days (owd) spanned by each acquisition is listed in parenthesis. 20

Table 2.2. Summary of environmental variables from ERA-5 (Hersbach et al., 2020) . . . 24

Table 2.3. Estimated shoreline change between each successive image observation date in each of the three regions identified in Figure 3, as well as across the whole study area. The mean and range are listed. 26

Table 2.4. Onshore heights and slopes derived from the identified upper and lower boundaries for each ICESat-2 observation. 30

Table 2.5. The dates of all images used for the cluster uncertainty analysis described in Section 2.2, along with the standard deviation of the residuals derived from each cluster. The total number of images from each date is listed in parenthesis 48

Table 2.6. North-South change in the upper and lower boundaries estimated from ICESat-2 and the land-water boundaries estimated from Planet at each sampled ICESat-2 location 49

Table 3.1. Parameters used for our modified CliffDelineaTool algorithm 63

Table 4.1. Summary of meteorological datasets used and the derived quantities 92

Table 4.2. Material class code compiled from ShoreZone. Note that the bedrock class (R) had no subcodes present in our study region 97

ACKNOWLEDGEMENTS

I would like to acknowledge the following people and groups:

My advisor Adrian, for providing steady guidance and support while also giving me the freedom to explore my research interests. I don't think you knew what you were signing up for when you agreed to take me on, but I am very grateful that you did.

My co-advisor Helen, for giving me an inside view on what it means to be involved in satellite missions and for being a consistent advocate for me and for permafrost representation in NASA Cryosphere research.

To my committee members, for serving as a resource and pointing me in the right direction when I wasn't sure what information I needed.

To my collaborators for providing thorough feedback on my research and writing and for helping fill my knowledge gaps.

To the multiple research groups within and beyond Scripps who welcomed me and taught me so much: the SIO hydrogeology lab, the SIO glaciology group, the SIO rocky coast group, and the Permafrost Coastal Systems Network (PerCS-Net).

To my undergraduate research mentors from The Sigma and Radioglaciology groups at Stanford. While my PhD research went in a different direction from my internship, I continued on to a PhD largely due to your support.

To my friends both at and beyond SIO. In particular, my housemate and friend Emily, who was a constant source of camaraderie, support, and fun distractions as we navigated our PhDs together.

To my family, for supporting my journey and always keeping an open door for me to visit (which I did quite often)

and finally, to my partner Nick, who has patiently waited all this for me to complete my PhD and come home. Thank you for your unwavering support and for always providing a safe space for me when I needed a break from my work.

Chapter 1 adapts the introduction of: Bryant, M. B., Borsa, A. A., Anderson, E. J., Masteller,

C. C., Michaelides, R. J., Siegfried, M. R., and Young, A. P. (2025). Multiple modes of shoreline change along the Alaskan Beaufort Sea observed using ICESat-2 altimetry and satellite imagery. The Cryosphere, 19:1825–1847. The dissertation author was the primary researcher and author on this paper. The paper is licensed under a Creative Commons Attribution 4.0 License, which allows for adaptation and re-use with proper attribution.

Chapter 2 is a reprint, in full, of: Bryant, M. B., Borsa, A. A., Anderson, E. J., Masteller, C. C., Michaelides, R. J., Siegfried, M. R., and Young, A. P. (2025). Multiple modes of shoreline change along the Alaskan Beaufort Sea observed using ICESat-2 altimetry and satellite imagery. The Cryosphere, 19:1825–1847. The dissertation author was the primary researcher and author on this paper. The paper is licensed under a Creative Commons Attribution 4.0 License, which allows for adaptation and re-use with proper attribution.

Chapters 3 and 4 are based on unpublished research done in collaboration with A. Borsa and A.Young. The dissertation author was the primary researcher on this project.

VITA

2019	Bachelor of Science in Physics (Astrophysics), University of California Santa Cruz
2021	Teaching Assistant, Scripps Institution of Oceanography, University of California San Diego
2026	Doctor of Philosophy in Earth Sciences, Scripps Institution of Oceanography, University of California San Diego

PUBLICATIONS

Michaelides, R. J., **Bryant, M. B.**, Siegfried, M. R., and Borsa, A. A.: Quantifying Surface-Height Change Over a Periglacial Environment With ICESat-2 Laser Altimetry, Earth Space Sci., 8, e2020EA001538, https://doi.org/10.1029/2020EA001538, 2021.

Bryant, M. B., Borsa, A. A., Anderson, E. J., Masteller, C. C., Michaelides, R. J., Siegfried, M. R., and Young, A. P.: Multiple modes of shoreline change along the Alaskan Beaufort Sea observed using ICESat-2 altimetry and satellite imagery, The Cryosphere, 19, 1825–1847, https://doi.org/10.5194/tc-19-1825-2025, 2025.

ABSTRACT OF THE DISSERTATION

Leveraging spaceborne and airborne lidar to characterize the morphology and evolution of eroding Arctic coasts in a changing climate

by

Marnie Bryant

Doctor of Philosophy in Earth Sciences

University of California San Diego, 2026

Adrian Borsa, Chair

Decreasing sea ice extent, increasing storm activity, and warming weather conditions are driving widespread erosion of Arctic permafrost coasts. This erosion threatens infrastructure, indigenous cultural practices, and regional economic development. It also leads to the influx of carbon and other compounds into the ocean, with implications both for ocean ecology and global carbon cycling. Understanding the drivers of Arctic coastal erosion is crucial for resilience efforts and carbon modeling, but the processes driving erosion are complex and hard to accurately quantify. Airborne and spaceborne lidar provide a way to quantify Arctic shore zone morphology, which is an important factor in modulating local shoreline change. This dissertation focuses on using cross-shore elevation profiles from lidar to capture spatiotemporal variations in coastal morphology

and relate different shore types to the dynamic response of the shoreline to spatiotemporal variations in ocean and atmospheric forcings. In Chapter 2, we demonstrate the potential for the satellite ICESat-2 to be combined with multispectral imagery to measure variable shoreline change across three distinct shore types on the Alaskan Beaufort Sea coast. In Chapter 3, we introduce a framework to systematically classify profiles from airborne lidar into physically distinct shore types using k-means clustering, and demonstrate its utility of the Western Chukchi Sea coast. In Chapter 4, we combine these elevation-based shore types with historical shoreline change data, sediment maps, and meteorological datasets to investigate the potential drivers of spatial variability in long-term shoreline trends. We conclude that remotely sensed elevation datasets can be used to meaningfully quantify shoreline morphology in the Arctic, but that this data must be used in conjunction with environmental forcings and other shoreline properties in order to better understand the sensitivity of local shorelines to a changing Arctic.

Chapter 1

Introduction

1.1 Motivation

Arctic coastlines are among the most rapidly eroding coastlines in the world. Pan-Arctic shoreline change rates over the second half of the 20th century have been estimated to be -0.5 m a^{-1} (where negative shoreline change indicates retreat) (Lantuit et al., 2012), while local, single-year local shoreline change estimates in Northern Alaska have reached up to -66.7 m (Bryant et al., 2025). These coastlines are vulnerable because they consist largely of permafrost, which is sediment that stays below 0°C year-round. Decreasing sea ice extent (Baranskaya et al., 2021; Overeem et al., 2011), increasing air (Baranskaya et al., 2021; Serreze and Barry, 2011) and ocean (Timmermans and Labe, 2023) temperatures, and increasing storm frequency (Baranskaya et al., 2021; Erikson et al., 2020; Manson and Solomon, 2007) are all driving rapid thaw and erosion of permafrost coasts.

Coastal erosion has far-reaching impacts on both the environment and coastal communities, as illustrated in Figure 1.1. As permafrost thaws, frozen organic material is decomposed, leading to the release of carbon dioxide and methane into the air and ocean. Increased atmospheric uptake of these compounds contribute to increased atmospheric warming (Fritz et al., 2017; Irrgang et al., 2022). Increased carbon input into the ocean from coastal erosion reduces the carbon dioxide uptake from the atmosphere, further increasing atmospheric carbon dioxide concentrations (Nielsen et al., 2024). In addition, the input of carbon and other land-bound compounds into the ocean impacts

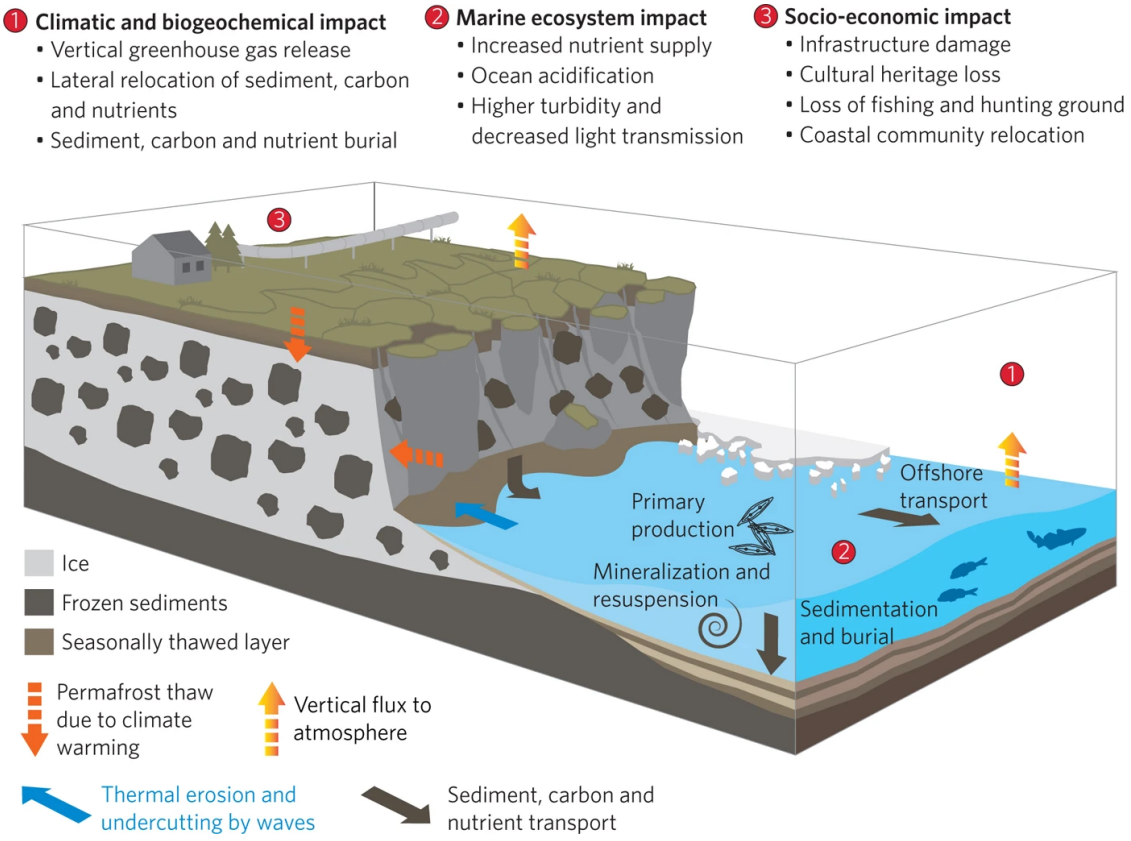


Figure 1.1: The primary mechanisms and consequences of Arctic coastal erosion, from Fritz et al. (2017)

the local marine ecosystem by contributing to ocean acidification and primary production (Fritz et al., 2017; Popova et al., 2012; Semiletov et al., 2016; Terhaar et al., 2021). Finally, erosion threatens coastal communities through damage to infrastructure and cultural sites, loss of economic opportunity, and loss of access to traditional navigation routes and subsistence practices (e.g., Brady and Leichenko, 2020; Irrgang et al., 2022). Accurate monitoring and forecasting of coastal retreat rates are needed to inform carbon cycling models and coastal resilience efforts.

1.2 Drivers of Arctic shoreline change

Arctic coastlines consist largely of permafrost and seasonally frozen sediments, which makes them susceptible to both thermal and mechanical erosion processes. Permafrost can be ice-rich (high pore ice content), ice-poor (low pore ice content), or contain no ice. Permafrost can also contain excess ice, or large volumes of frozen water without sediment. During the open water season, i.e., when the coasts are not sheltered by sea ice, the shoreline is subjected to warm ocean temperatures and mechanical energy from waves, driving ground ice thaw and erosion through thermal abrasion (Aré, 1988; Baranskaya et al., 2021; Günther et al., 2013). Above the water line, warm air temperatures, high winds (Baranskaya et al., 2021; Günther et al., 2013), and precipitation (Zwieback et al., 2018) can drive top-down ground-thawing and erosion through thermal denudation. In additional to thermal-mechanical erosion, along-shore sediment transport can lead to either the depletion or growth of beaches, barrier islands, and spits. Observational studies (Nielsen et al., 2020) and models (e.g., Nielsen et al., 2020; Rolph et al., 2022) have demonstrated the correspondence between environmental forcings and decadal-scale retreat over regional scales ($\sim$100s of km).

While large-scale changes are driven by environmental forcings, small-scale variability is influenced by local variations in shoreline morphology, with different shore types being dominated by different erosion and accretion processes. For example, steep coastal bluffs are predominately subjected to erosion from thermal abrasion at their base and thermal denudation above the water line (Aré, 1988; Baranskaya et al., 2021; Günther et al., 2013; Irrgang et al., 2022). High rates of thermal abrasion can lead to bluff collapse events, where a cohesive block detaches from the

shoreline. These blocks can temporarily shelter the shoreline from additional wave activity, but tend to disintegrate over the span of several days (Barnhart et al., 2014; Overeem et al., 2011) or weeks (Jones et al., 2018). Coastal beaches and dunes, on the other hand, are subject to erosion or accretion depending on alongshore sediment transport patterns. Decadal-scale studies of regional shoreline change (Baranskaya et al., 2021; Farquharson et al., 2018; Irrgang et al., 2018) have shown variable rates between different shore types such as bluffs and sand and gravel beaches. In addition to variations in shoreline type, observations of erosion rates and simulated wave run-up models in both temperate (Earlie et al., 2018) and Arctic (Rolph et al., 2022) environments have suggested that wave-driven retreat is sensitive to shoreline geometric attributes such as beach slope and the elevation of the beach-cliff junction.

Over time, erosion, accretion and ground thaw can drive changes in shoreline morphology which can in turn affect retreat rates, causing either positive or negative feedback loops. For example, surface subsidence due to ground thaw in flood-prone areas and the shrinking of beaches and barrier islands protecting the coast can both lead to accelerated thaw and erosion (Farquharson et al., 2018; Irrgang et al., 2018). Thaw slump formation (Lim et al., 2020b) and beach and barrier island growth due to sediment deposition can lead to the stabilization or advancement of the shoreline (Erikson et al., 2020; Farquharson et al., 2018; Irrgang et al., 2018). In areas that are undergoing rapid changes, shoreline morphology can therefore not be assumed to be static.

1.3 Quantifying shoreline morphology and change with elevation data

Quantifying the relationship between Arctic shoreline morphology and change requires high resolution, up-to-date estimates of shoreline position, topography and morphologic type, which can be inferred from elevation measurements. Elevation measurements from airborne lidar (e.g., Jones et al., 2013) and aerial photogrammetry (e.g., Gibbs et al., 2019; Lim et al., 2020a,b) have been used to qualitatively characterize the shoreline, provide high-resolution estimates of shoreline position, capture short-term topographic change, and enable comparisons of retreat rates between

different geomorphic units (e.g., Lim et al., 2020a) on seasonal (e.g., Gibbs et al., 2019; Lim et al., 2020a) to multi-year (e.g., Jones et al., 2013) timescales and over km-scale areas (e.g., Lim et al. 2020a). The increasing availability of mid to high resolution space borne elevation measurements such as radar interferometry (e.g., TANDEM-X), stereo photogrammetry (e.g., ArcticDEM), and altimetry (e.g., ICESat-2 and the upcoming EDGE mission) provides the opportunity to characterize coastal morphology at regional to pan-Arctic scales and provide a time series of morphologic change over time. While airborne elevation studies typically use qualitative descriptors and manual identification to describe coastal morphology, large-scale, repeat measurements from satellites will need an automated, quantitative method to systematically classify the coastline.

1.4 Research objectives

This dissertation focuses on the following research questions:

1. How can we efficiently quantify coastal morphology using lidar?
2. How does morphology influence the rate of shoreline change for given environmental conditions?

To answer these questions, I use a combination of airborne and space borne lidar. The Ice, Cloud and land Elevation Satellite 2 (ICESat-2) mission provides an example of the potential of space borne lidar for shoreline characterization and monitoring, while airborne lidar provides a large volume of high-fidelity data on which to test new algorithms that could eventually be applied to satellite data. The work is broken down into the following chapters:

- **Chapter 2** presents a case study of the application of spaceborne lidar altimetry measurements from ICESat-2 and high-resolution multispectral imagery to highlight short-term, local variability across different shore types on a section Alaskan Beaufort Sea coast (shown in Figure 1.2).
- **Chapter 3** presents a k-means-based method to systematically classify elevation profiles

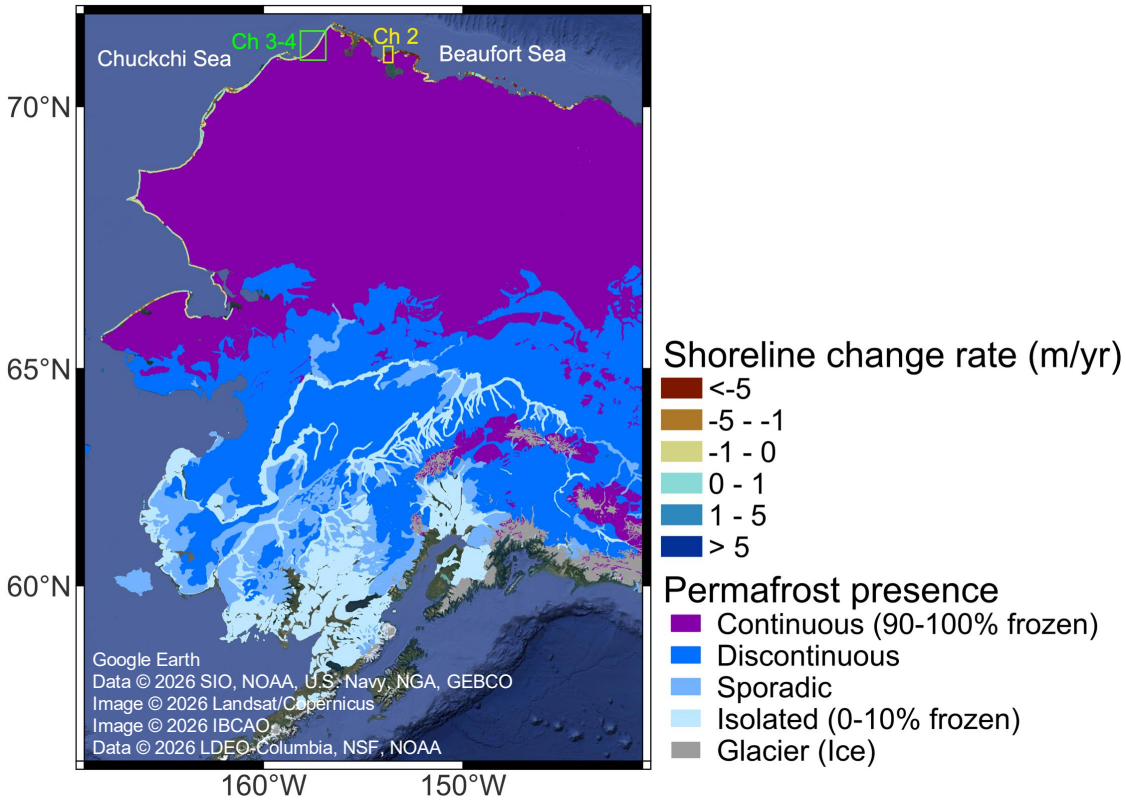


Figure 1.2: Pan-Alaskan permafrost presence (from Jorgenson (2022)) and shoreline change rates in Northern Alaska (from Gibbs et al. (2024)). The study sites covered in this dissertation are marked.

from airborne lidar into different shore types and demonstrates it over a stretch of the western Chukchi sea coast (shown in Figure 1.2).

- **Chapter 4** combines these derived shore types, long-term historic retreat rates, and long-term meteorologic data to understand the drivers in spatial variability in shoreline change rates along the western Chukchi Sea coast.

- **Chapter 5** will summarize and discuss our findings and highlight avenues for future work.

1.5 Acknowledgments

Material from this chapter is adapted from the introduction of the following publication:

Bryant, M. B., Borsa, A. A., Anderson, E. J., Masteller, C. C., Michaelides, R. J., Siegfried,

M. R., and Young, A. P. (2025). Multiple modes of shoreline change along the Alaskan Beaufort Sea observed using ICESat-2 altimetry and satellite imagery. The Cryosphere, 19:1825–1847.

The dissertation author was the primary researcher and author on this paper. The paper is licensed under a Creative Commons Attribution 4.0 License, which allows for adaptation and re-use with proper attribution.

References

Aré, F. E. (1988). Thermal abrasion of sea coasts (part I). *Polar Geography and Geology*, 12(1):1–1.

Baranskaya, A., Novikova, A., Shabanova, N., Belova, N., Maznev, S., Ogorodov, S., and Jones, B. M. (2021). The Role of Thermal Denudation in Erosion of Ice-Rich Permafrost Coasts in an Enclosed Bay (Gulf of Kruzenstern, Western Yamal, Russia). *Frontiers in Earth Science*, 8:566227.

Barnhart, K. R., Anderson, R. S., Overeem, I., Wobus, C., Clow, G. D., and Urban, F. E. (2014). Modeling erosion of ice-rich permafrost bluffs along the Alaskan Beaufort Sea coast. *Journal of Geophysical Research: Earth Surface*, 119(5):1155–1179.

Brady, M. B. and Leichenko, R. (2020). The impacts of coastal erosion on Alaska's North Slope communities: A co-production assessment of land use damages and risks. *Polar Geography*, 43(4):259–279.

Bryant, M. B., Borsa, A. A., Anderson, E. J., Masteller, C. C., Michaelides, R. J., Siegfried, M. R., and Young, A. P. (2025). Multiple modes of shoreline change along the Alaskan Beaufort Sea observed using ICESat-2 altimetry and satellite imagery. *The Cryosphere*, 19:1825–1847.

Earlie, C., Masselink, G., and Russell, P. (2018). The role of beach morphology on coastal cliff erosion under extreme waves. *Earth Surface Processes and Landforms*, 43(6):1213–1228.

Erikson, L. H., Gibbs, A. E., Richmond, B. M., Storlozzi, C. D., Jones, B. M., and Ohman, K. A. (2020). Changing Storm Conditions in Response to Projected 21st Century Climate Change and the Potential Impact on an Arctic Barrier Island–Lagoon System—A Pilot Study for Arey Island and Lagoon, Eastern Arctic Alaska. Technical Report, U.S. Geological Service.

Farquharson, L., Mann, D., Swanson, D., Jones, B., Buzard, R., and Jordan, J. (2018). Temporal and spatial variability in coastline response to declining sea-ice in northwest Alaska. *Marine Geology*, 404:71–83.

Fritz, M., Vonk, J. E., and Lantuit, H. (2017). Collapsing Arctic coastlines. *Nature Climate Change*, 7(1):6–7.

Gibbs, A. E., Nolan, M., Richmond, B. M., Snyder, A. G., and Erikson, L. H. (2019). Assessing patterns of annual change to permafrost bluffs along the North Slope coast of Alaska using high-resolution imagery and elevation models. *Geomorphology*, 336:152–164.

Gibbs, A. E., Ohman, K. A., Coppersmith, R., and Richmond, B. M. (2024). National Assessment of Shoreline Change: A GIS compilation of updated vector shorelines and associated shoreline change data for the north coast of Alaska, U.S. Canadian border to Icy Cape (ver. 2.0, September 2024). U.S. Geological Survey data release, 10.5066/F72Z13N1.

Günther, F., Overduin, P. P., Sandakov, A. V., Grosse, G., and Grigoriev, M. N. (2013). Short- and long-term thermo-erosion of ice-rich permafrost coasts in the Laptev Sea region. *Biogeosciences*, 10(6):4297–4318.

Irrgang, A. M., Bendixen, M., Farquharson, L. M., Baranskaya, A. V., Erikson, L. H., Gibbs, A. E., Ogorodov, S. A., Overduin, P. P., Lantuit, H., Grigoriev, M. N., and Jones, B. M. (2022). Drivers, dynamics and impacts of changing Arctic coasts. *Nature Reviews Earth & Environment*, 3(1):39–54.

Irrgang, A. M., Lantuit, H., Manson, G. K., Günther, F., Grosse, G., and Overduin, P. P. (2018). Variability in Rates of Coastal Change Along the Yukon Coast, 1951 to 2015. *Journal of Geophysical Research: Earth Surface*, 123(4):779–800.

Jones, B. M., Farquharson, L. M., Baughman, C. A., Buzard, R. M., Arp, C. D., Grosse, G., Bull, D. L., Günther, F., Nitze, I., Urban, F., Kasper, J. L., Frederick, J. M., Thomas, M., Jones, C., Mota, A., Dallimore, S., Tweedie, C., Maio, C., Mann, D. H., Richmond, B., Gibbs, A., Xiao, M., Sachs, T., Iwahana, G., Kanevskiy, M., and Romanovsky, V. E. (2018). A decade of remotely sensed observations highlight complex processes linked to coastal permafrost bluff erosion in the Arctic. *Environmental Research Letters*, 13(11):115001.

Jones, B. M., Stoker, J. M., Gibbs, A. E., Grosse, G., Romanovsky, V. E., Douglas, T. A., Kinsman, N. E. M., and Richmond, B. M. (2013). Quantifying landscape change in an arctic coastal lowland using repeat airborne LiDAR. *Environmental Research Letters*, 8(4):045025.

Jorgenson, T. (2022). Permafrost Characteristics of Alaska. [Feature Layer]. Scale not given. "Alaska Permafrost Zones." https://www.arcgis.com/home/item.html?id=4fb081bf8de242d9ada3afbe3bf03684overview. (August 24, 2026).

Lantuit, H., Overduin, P. P., Couture, N., Wetterich, S., Aré, F., Atkinson, D., Brown, J., Cherkashov, G., Drozdov, D., Forbes, D. L., Graves-Gaylord, A., Grigoriev, M., Hubberten, H.-W., Jordan, J., Jorgenson, T., Ødegård, R. S., Ogorodov, S., Pollard, W. H., Rachold, V., Sedenko, S., Solomon, S., Steenhuisen, F., Streletskaya, I., and Vasiliev, A. (2012). The Arctic Coastal Dynamics Database: A New Classification Scheme and Statistics on Arctic Permafrost Coastlines. *Estuaries and Coasts*, 35(2):383–400.

Lim, M., Whalen, D., J. Mann, P., Fraser, P., Berry, H. B., Irish, C., Cockney, K., and Woodward, J. (2020a). Effective Monitoring of Permafrost Coast Erosion: Wide-scale Storm Impacts on Outer Islands in the Mackenzie Delta Area. *Frontiers in Earth Science*, 8:561322.

Lim, M., Whalen, D., Martin, J., Mann, P. J., Hayes, S., Fraser, P., Berry, H. B., and Ouellette, D. (2020b). Massive Ice Control on Permafrost Coast Erosion and Sensitivity. *Geophysical Research Letters*, 47(17):e2020GL087917.

Manson, G. K. and Solomon, S. M. (2007). Past and future forcing of Beaufort Sea coastal change.

Atmosphere-Ocean, 45(2):107–122.

Nielsen, D. M., Chegini, F., Maerz, J., Brune, S., Mathis, M., Dobrynin, M., Baehr, J., Brovkin, V., and Ilyina, T. (2024). Reduced Arctic Ocean CO2 uptake due to coastal permafrost erosion. *Nature Climate Change*, 14(9):968–975.

Nielsen, D. M., Dobrynin, M., Baehr, J., Razumov, S., and Grigoriev, M. (2020). Coastal Erosion Variability at the Southern Laptev Sea Linked to Winter Sea Ice and the Arctic Oscillation. *Geophysical Research Letters*, 47(5):e2019GL086876.

Overeem, I., Anderson, R. S., Wobus, C. W., Clow, G. D., Urban, F. E., and Matell, N. (2011). Sea ice loss enhances wave action at the Arctic coast: Sea ice loss enhances erosion. *Geophysical Research Letters*, 38(17):n/a–n/a.

Popova, E. E., Yool, A., Coward, A. C., Dupont, F., Deal, C., Elliott, S., Hunke, E., Jin, M., Steele, M., and Zhang, J. (2012). What controls primary production in the Arctic Ocean? Results from an intercomparison of five general circulation models with biogeochemistry. *Journal of Geophysical Research: Oceans*, 117(C8):2011JC007112.

Rolph, R., Overduin, P. P., Ravens, T., Lantuit, H., and Langer, M. (2022). ArcticBeach v1.0: A physics-based parameterization of pan-Arctic coastline erosion. *Frontiers in Earth Science*, 10:962208.

Semiletov, I., Pipko, I., Gustafsson, Ö., Anderson, L. G., Sergienko, V., Pugach, S., Dudarev, O., Charkin, A., Gukov, A., Bröder, L., Andersson, A., Spivak, E., and Shakhova, N. (2016). Acidification of East Siberian Arctic Shelf waters through addition of freshwater and terrestrial carbon. *Nature Geoscience*, 9(5):361–365.

Serreze, M. C. and Barry, R. G. (2011). Processes and impacts of Arctic amplification: A research synthesis. *Global and Planetary Change*, 77(1-2):85–96.

Terhaar, J., Lauerwald, R., Regnier, P., Gruber, N., and Bopp, L. (2021). Around one third of current Arctic Ocean primary production sustained by rivers and coastal erosion. *Nature Communications*, 12(1):169.

Timmermans, M. L. and Labe, Z. (2023). NOAA Arctic Report Card 2023: Sea Surface Temperature.

Zwieback, S., Kokelj, S. V., Günther, F., Boike, J., Grosse, G., and Hajnsek, I. (2018). Sub-seasonal thaw slump mass wasting is not consistently energy limited at the landscape scale. *The Cryosphere*, 12(2):549–564.

Chapter 2

Multiple modes of shoreline change along the Alaskan Beaufort Sea observed using ICESat-2 altimetry and satellite imagery

Abstract

Arctic shorelines are retreating rapidly due to declining sea ice cover, increasing temperatures, and increasing storm activity. Shoreline morphology may influence local retreat rates, but quantifying this relationship requires repeat estimates of shoreline positions and morphologic properties. Here we use a novel combination of shoreline boundaries from multispectral imagery from Planet and topographic profiles from ICESat-2 satellite altimetry to compare year-to-year changes in shoreline position and morphology across different shoreline types, focusing on an 8 km stretch of the Alaskan Beaufort Sea Coast during the 2019-2021 open water seasons. We consider temporal and spatial variability in shoreline change in the context of environmental forcings from ERA5 and morphologic classifications from the ShoreZone database. We find a mean spatially averaged shoreline change rate of -16.5 m a^{-1} over 3 years, with local estimates ranging from -66.7 m to +18.6 m in a single year. We posit that annual and km-scale variability in shoreline change can be explained by the response of different geomorphic units to time-varying wave and ocean conditions. Ice-rich coastal bluffs and inundated tundra exhibited high retreat that is likely driven by high temperatures and wave exposure, while the stretch of shoreline with vegetated peat in front of a large breached thermokarst lake remained relatively stable. Our topographic profiles

from ICESat-2 sample three distinct shoreline types (a bluff, a small drained lake basin, and a dune in front of a large drained lake basin) that exhibit different patterns of shoreline change (both in terms of position and morphology) over the three-year study period. Analysis of altimetry-derived morphologic parameters such as elevation and slope and small-scale features such as toppled blocks and surface ponding provide insight on specific erosion and accretion processes that drive shoreline change. We conclude that repeat altimetry measurements from ICESat-2 and multispectral imagery provide complementary observations that illustrate how both the position and the topography of the shoreline are changing in response to a changing Arctic.

2.1 Introduction

This chapter demonstrates the utility of The Ice, Cloud and land Elevation Satellite 2 (ICESat-2) laser altimeter for measuring short-term shoreline change. ICESat-2 collects repeat cross-shore elevation profiles, providing the potential to expand on previous elevation-based work with satellite altimetry and transform our understanding of Arctic shoreline morphology and change. ICESat-2's Advanced Topographic Laser Altimeter System (ATLAS) emits a laser pulse at 532 nm (green light), and provides elevations of individual surface-reflected photons in the ATL03 data product (Neumann et al., 2019).The laser pulse generated by ATLAS is split into 3 pairs of beams, illuminating a total of 6 ground tracks that are nominally centered around a reference ground track. Each beam within a pair is separated by 90 m across-track (i.e., perpendicular to the orbital motion of the satellite), and each pair is separated by 3.3 km. ATLAS's 11 m diameter footprint (Magruder et al., 2021), 70 cm along-track sampling at full resolution (Markus et al., 2017), and centimeter-to-decimeter vertical precision (Brunt et al., 2021) allows for high resolution measurements of shoreline topography. Xie et al. (2021) and Liu et al. (2022) demonstrated the potential for using ICESat-2 altimetry to classify the shoreline by geometric unit, although these studies focused only on one-time characterization. The ICESat-2 repeat-track orbit revisits the same ground track every 91 days, which enables measurement of annual and potentially sub-annual changes in shoreline position, elevation, and shoreline morphology. Several higher-level data products have been derived

from the ATL03 photon product to reduce data volume and provide more easily interpretable elevation estimates for different applications, such as vegetation (Neuenschwander et al., 2023), land ice (Smith et al., 2023), and inland water (Jasinski et al., 2023). However, the resolution of these higher-level data products ($\geq$ 20 m) is not sufficient to accurately describe complex Arctic landscapes (Michaelides et al., 2021) or measure the sub-10 meter changes in shoreline position that characterize much of the Arctic (Lantuit et al., 2012). New processing techniques are needed to generate coastal elevation transects from ICESat-2 photon data (ATL03).

Here, we present a case study demonstrating how repeat altimetry from ICESat-2 can be utilized in tandem with satellite imagery to track annual shoreline change and provide insight on short-term and local shoreline processes. We implement a processing pipeline to generate high-resolution elevation profiles from ICESat-2 photon data and extract shoreline boundaries that can be compared with those derived from satellite multispectral imagery. We demonstrate the utility of higher resolution ICESat-2 elevation data over the 2019–2021 open water seasons to investigate changes in cross-shore topography over time. We focus on the shoreline surrounding Drew Point, Alaska, where shoreline change rates are both high (averaging -22 m a^{-1} over the last decade) and variable (-48.8 m a^{-1} to 0 m a^{-1} on $\sim$ 10 m length scales) (Jones et al., 2018), and multiple shoreline types (including coastal bluffs and drained lake basins) are present (Jones et al., 2009). We quantify annual variations in sea ice cover, wave activity, and ocean and air temperatures to establish year-to-year environmental forcings on the shoreline. Next, we derive shoreline positions and annual shoreline change from satellite multispectral imagery from Planet and evaluate temporal and spatial variations in the shoreline response to these forcings. We then analyze ICESat-2 elevation profiles and discuss the inferred shoreline type, topographic change, and potential causes of these observed shoreline changes. We also compare our ICESat-2 derived change estimates with imagery-derived change estimates. We conclude with a discussion of the advantages and challenges of characterizing shoreline structure and change with ICESat-2 altimetry and how it can be leveraged with other datasets to better understand Arctic shoreline evolution.

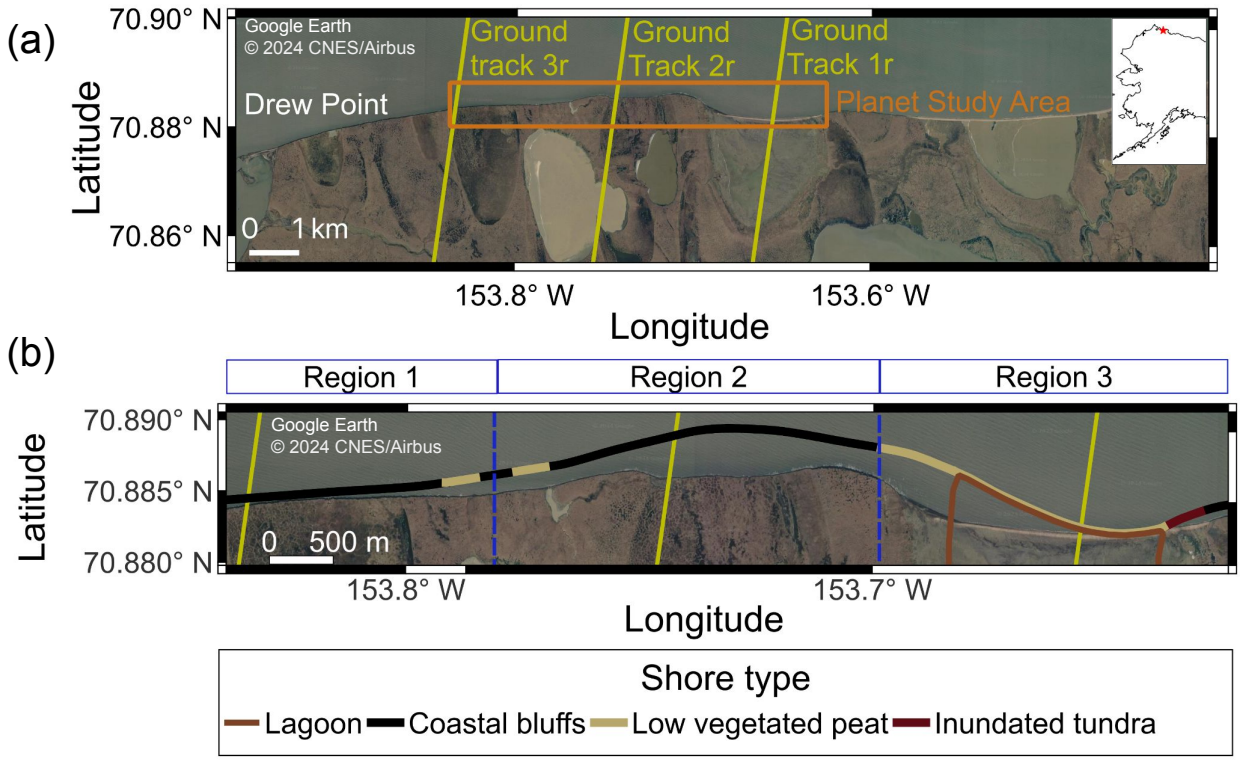


Figure 2.1: a) Overview of the Study Area on the Alaskan Beaufort Sea Coast, with the extent of the Planet imagery used and location of the ICESat-2 ground tracks indicated. b) A close-up of the study area and shore-type classifications of the 2007 shoreline from ShoreZone (Harper and Morris, 2014). We divide our study area into 3 regions based on geography and shoreline type. Background imagery is from 2018, ©2024 Google Earth CNES/Airbus

2.2 Data and Methods

2.2.1 Study Area

Our study focused on an $\sim$ 8 km stretch of coast to the east of Drew Point on the North Slope of Alaska (Fig. 2.1). This study area largely consists of exposed ice-rich bluffs with narrow beaches along the coast and thermokarst lakes and drained lake basins onshore (Gibbs and Richmond, 2015; Jorgenson et al., 2014). Most of the shoreline in this region is less than 3 m high, although the bluffs near drew point reach as high as 6 m (Gibbs and Richmond, 2015). Erosion is largely driven by thermal mechanical notching of bluffs, followed by bluff collapse (Barnhart et al., 2014; Gibbs and Richmond, 2015; Jones et al., 2018). The area around Drew Point is among the most rapidly

retreating locations in the Arctic, with decadal-scale shoreline change rates in excess of -10 m a^{-1} (Gibbs and Richmond, 2015; Jones et al., 2009) and evidence that retreat rates are increasing in recent years (Jones et al., 2009, 2018). Jones et al. (2018) found highly variable change in this study area, with mean shoreline change averaged over a 9 km stretch of shoreline varying from -6.7 m to -22.0 m per open water season between 2007 and 2016. Although they found that the greatest retreat occurred in the year with most storms and warmest air temperatures, they did not find a robust relationship between spatially averaged retreat rates and open water days, storm activity, air temperature, permafrost temperature, or sea surface temperature over the entirety of the 10-year study period. Maximum local retreat was 2–3 times higher than spatially averaged retreat, pointing to the potential influence of local controls (such as morphology) on shoreline change.

We divide our study area into three regions (Fig. 2.1b.) with repeated cross-shore ICESat-2 profiles. We delineate these regions primarily based on visual analyses of 2018 optical imagery collected by CNES Airbus that was accessed through Google Earth and draw from Gibbs and Richmond (2015), Jones et al. (2009), and the ShoreZone database (Harper and Morris, 2014) to describe the morphological setting of each region. ShoreZone includes a classification of variable-length segments of the shoreline based on aerial photography taken in 2007. These classifications are based on the substrate and morphology of the shoreline as well as the dominant erosion and accretion processes thought to be present. Given the high amount of shoreline retreat in the last decade (Jones et al., 2018), specific local features identified by ShoreZone in 2007 may have been removed or modified, but we expect the general morphologic setting to be consistent with current conditions. Region 1, the westernmost portion of the study area, primarily consists of steep, ice-rich coastal bluffs (Gibbs and Richmond, 2015; Harper and Morris, 2014; Jones et al., 2009). ShoreZone indicates the sporadic presence of low, vegetated peat-rich sediment, which are likely the remnants of old drained lake basins (Jones et al., 2009) that have since been removed by erosion. Region 2 consists of the headlands and is characterized as the same shoreline types as Region 1 (coastal bluffs and drained lake basins). Region 3 is a large breached thermokarst lake (Gibbs and Richmond, 2015; Jones et al., 2009) that is classified in ShoreZone as a large lagoon behind a narrow strip of

low vegetated peat. The easternmost portion of this shoreline is classified as an inundated tundra environment, where the nearshore elevation is below sea-level, and there has been significant thaw subsidence and flooding.

2.2.2 Time-varying environmental conditions

To investigate drivers of year-to-year variations in shoreline positions, we considered ocean wave conditions, air temperature, and sea ice concentration from the European Centre for Medium-Range Weather Forecasts Reanalysis v5 (ERA5) dataset (Hersbach et al., 2020). ERA5 provides hourly estimates of atmospheric and sea ice conditions at 0.25° resolution and wave conditions at 0.5° resolution.

Sea ice and ocean waves

During the open water season, waves transport heat and mechanical energy to the base of permafrost bluffs, driving retreat via thermal and mechanical abrasion (Aré, 1988; Baranskaya et al., 2021; Wobus et al., 2011). The vast majority of shoreline retreat along the Beaufort Sea Coast occurs during the open water season, and the length of the open water season has been proposed as first-order predictor of retreat rates (Overeem et al., 2011). For each year, we estimated the duration of the open water season from the ERA5 sea daily mean sea ice concentration. Following Overeem et al. (2011), we defined the open water season as the period over which the daily mean sea ice concentration is $< 15\%$. The open water season spans the period starting from the first day sea ice falls below 15% for at least two consecutive days to the first day sea ice remains above 15% for at least two consecutive days. We also counted the total number of open water days (owd) spanned by each pair of Planet and ICESat-2 acquisitions, including single-day breakup events that occur outside of the open water season.

The majority of wave-driven retreat is thought to occur during storms with large waves (Barnhart et al., 2014), although time lapse imagery has shown that thermal erosion and bluff collapse can occur even under relatively calm conditions (wave heights < 0.3 m) as long as waves make contact with the base of the bluffs (Overeem et al., 2011; Wobus et al., 2011). Thus, we

considered both the frequency of extreme wave events and total wave exposure over the open water season. We calculated the integral of the squared hourly significant wave height (H_s) as a proxy for cumulative wave energy. We defined the count of extreme events as the number of hours for which $H_s \geq 1.4$ m, corresponding to the upper 5% of wave heights over the 3-year study period.

Air and sea surface temperature

Ocean temperatures are an important driver of thermal mechanical erosion, as warm temperatures are required to melt frozen sediments, which are then removed by waves. Modeling of ice-rich bluffs by Barnhart et al. (2014) showed that large retreat events only occur when ocean temperatures exceed 0 °C. Subaerial retreat, which drives the loss of sediment from the upper shoreline via permafrost thaw, is driven by warm air temperatures (Baranskaya et al., 2021; Barnhart et al., 2014; Wobus et al., 2011).

We aggregated daily mean air temperature from ERA5 between 1 June and 31 October of each year (following Jones et al. (2018)) and the daily mean sea surface temperature for each open water season, when the base of the shoreline is exposed to the ocean. For both the air and sea surface temperature for each measurement period, we calculated the number of accumulated degree days of thaw (ADDT), defined as the sum of daily temperatures > 0 °C. We also recorded the mean air and ocean temperature between 1 June and 31 October of each year.

2.2.3 Shoreline identification from satellite multispectral imagery

We estimated annual shoreline positions using 3 m multispectral (red, green, blue, near-IR) images from Planet Labs' Super Dove, Dove R, and Dove Classic satellite constellations (Planet Team, 2023). We used four images, each collected near the beginning of each open water season from 2019 to 2022 (Table 2.1, Fig. 2.2). Frequent cloud cover in 2019 necessitated the use of imagery from 25 June, when a small amount of snow or ice remained visible near the shoreline.

Historically, shoreline change has been estimated from satellites via manual delineation of the shoreline (Farquharson et al., 2018; Günther et al., 2015; Irrgang et al., 2018; Jones et al., 2009). Recent workflows such as CoastSat (Vos et al., 2019) have been developed to automatically

detect the shorelines at sub-pixel resolution, but they have focused on lower-latitude beaches and may not perform well in Arctic regions where sea ice is present. Here, we implement our own shoreline detection method, following some of the same steps as Vos et al. (2019). For each image, we calculated the normalized differenced water index (NDWI) from the green (G) and near-IR (NIR) bands:

$$NDWI = \frac{G - NIR}{G + NIR} \tag{2.1}$$

We identified the NDWI threshold corresponding to the land-water boundary using Otsu's method, which determines the threshold that divides a set of pixels into two classes such that the inter-class variance is maximized (Otsu, 1979) (see the histograms in Fig. 2.8). We identified the sub-pixel land-water boundary from our NDWI images using a marching squares algorithm implemented in matplotlib contour in Python (Hunter, 2007). We found that calculating our threshold using all image pixels resulted in an adequate shoreline estimate for all four of our images, such that an initial identification of land and water pixels (as is done in Vos et al. (2019)) is not necessary. We visually identified and masked out regions where the shoreline appeared to be misidentified due to an ambiguous land-water boundary (shaded regions in Fig. 2.3). In order to improve the visual agreement of the derived shorelines with the visible shoreline in imagery and to ensure regular along-shore sampling intervals, we smoothed each shoreline using a 30 m along-shore running mean and sampled every 10 m alongshore to produce our final shoreline segments (Fig. 2.2). Finally, we estimated shoreline change using an approach similar to the USGS Digital Shoreline Analysis Software (Himmelstoss et al., 2021). In this workflow, a reference shoreline (hereafter referred to as the baseline) is selected. Cross-shore transects are generated at regular intervals along-shore that are perpendicular to this baseline. The change between consecutive shorelines is then calculated along these transects. We created a baseline by smoothing the raw 2020 shoreline with a 60 m along-shore running mean in order to assure adjacent cross-shore transects did not intersect on the time interval of our study site. Transects were generated every 10 m along the baseline using a modified version

of the SDS_transects routine (Vos, 2024) from the CoastSat Toolbox (Vos et al., 2019) that generates transects that bisect the shoreline. The change along each transect was calculated between each successive shoreline.

The estimated shorelines are subject to uncertainty from image geolocation errors, tidal- and storm-driven wave runup influences on the land-water boundary, and errors in the threshold determined with Otsu's method. The tides in this region tend to be less than 0.2 m, but storm surges can result in temporary relative sea level increases of 1.4 m (Jones et al., 2018). However, given that much of this region consists of steep bluffs with narrow, or no beaches (Gibbs and Richmond, 2015)), changes in the local relative sea level are not expected to have a large impact on the observed land-water boundary. To estimate the uncertainty in our shoreline estimates, we identified six clusters of three to six images (25 images in total) taken within a week of one another in the early summer (mid June through late July). Modeling of coastal bluff retreat in this region by Barnhart et al. (2014) suggests that large ($>$ 2.5 m) erosion events are concentrated in late summer (late July-late September) and driven by storms. Therefore, we do not expect large retreat events during early summer, such that the dominant source of change over short periods will be transient signals such as relative sea level changes and geolocation offsets. We calculated the cross-shore difference between each shoreline position and the mean position of its cluster and pooled the residuals across all shorelines (Table 2.5). We defined our shoreline estimation uncertainty to be the standard deviation of the pooled residuals.

2.2.4 Elevation profiles from ICESat-2 altimetry

Outside of the poles, the majority of ICESat-2 revisits between 2019 and 2022 were off-pointed from their nominal ground track location to increase aerial coverage, such that subsequent revisits did not cover the same ground location. However, "Target of Opportunity" requests over the North Slope of Alaska resulted in exact repeats of every fifth reference ground track starting in April 2019. We analyzed repeat ICESat-2 elevation profiles from three ground tracks (ground tracks 3r, 2r, and 1r, labeled in Fig. 2.1 a.) from a single reference ground track crossing our study area. Due

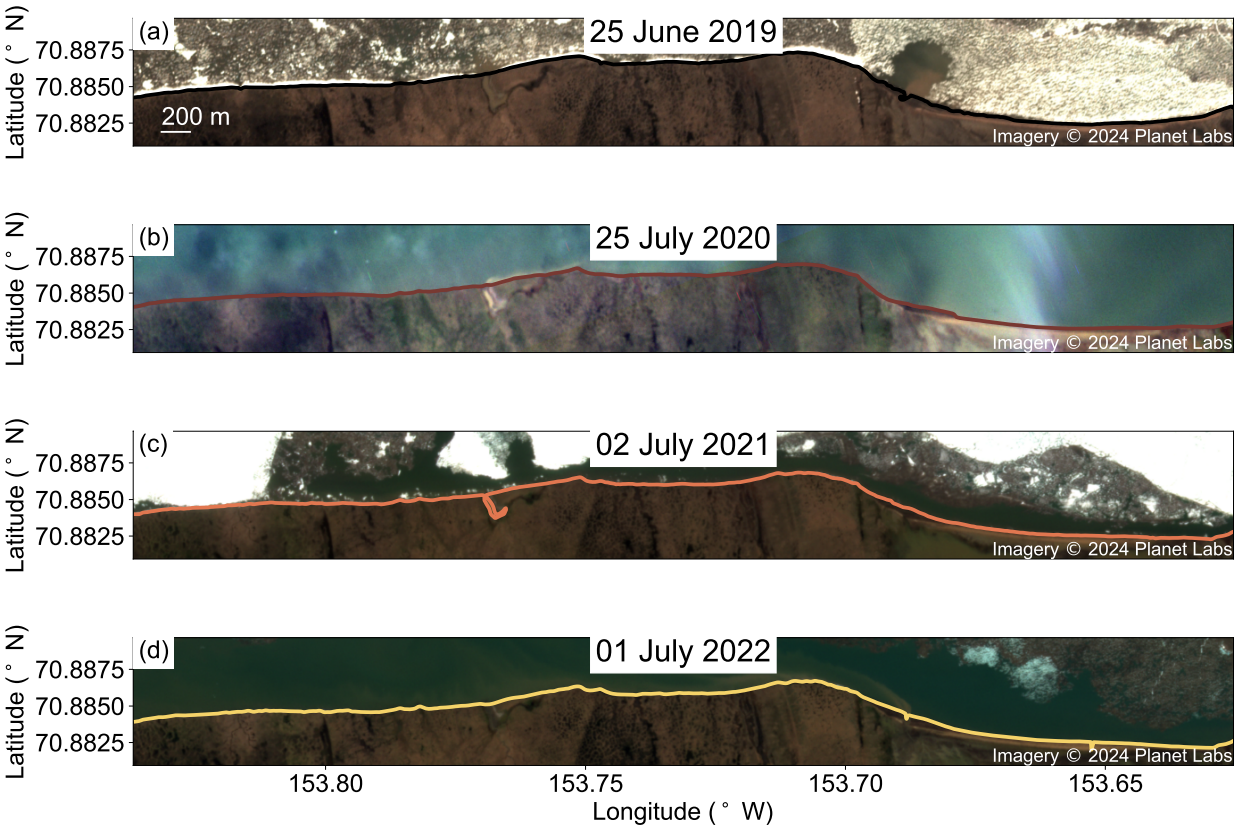


Figure 2.2: Planet Labs imagery (©2024 Planet Labs Inc) used to estimate shoreline positions. Shorelines delineated using Otsu thresholding are overlain and show good agreement with the visible land-water boundary.

Table 2.1: Observation intervals from Planet imagery and ICESat-2. The number of open water days (owd) spanned by each acquisition is listed in parenthesis.

Interval	Planet dates	ICESat-2 dates
2019 – 2020	25 June 2019 – 25 July 2020 (154 owd)	07 April 2019 (weak) – 04 January 2020 (strong) (138 owd)
2020 – 2021	25 July 2020 – 02 July 2021 (97 owd)	04 January 2020 (strong) – 02 July 2021 (strong) (111 owd)
2021 – 2022	02 July 2021 – 01 July 2022 (91 owd)	02 July 2021 (strong) – 31 December 2021 (weak) (91 owd)

to frequent cloud cover in the summer and fall, as well as the relatively low surface reflectivity of the snow-free tundra, the majority of observation dates with sufficient surface-reflected photons to accurately identify the surface occurred in the winter (January and April), with 2021 being the only year with available snow-free profiles. We selected four observation dates spanning the 2019–2021 open water seasons (Table 2.1), resulting in 12 individual profiles.

For each profile, we used 200 m of cross-shore ATL03 photons (Neumann et al., 2023) for our analysis. Each photon from ATL03 is assigned a confidence code ranging from 0 (noise) to 4 (high confidence) to indicate how likely it is to be a transmitted photon that was reflected from the surface (i.e. a signal photon). From each ATL03 profile, we selected all high-confidence (confidence score = 4) and medium-confidence (confidence score = 3) photons for further processing. These photon data were plotted and inspected to provide a qualitative analysis of small-scale features. We used the SlideRule Python Client (Shean et al., 2023) to run a customized version of the ATLAS/ICESat-2 L3A Land Ice Height (ATL06) algorithm (Smith et al., 2019), which estimates surface elevations using an iterative process of filtering and linear fitting of individual photon elevations. In this process, a linear fit is performed over fixed-length along-track segments of signal photons, outliers are filtered out based on a specified window above and below the linear surface, and the remaining photons are re-fit. This process is iterated using a successively narrower outlier window, until either it converges or the outlier window reaches a user-specified minimum value. The reported elevation for each segment is the height of the midpoint of the final linear interpolation. SlideRule provides the RMS error between the photons used in the final fitting and the final linear fit, as well as the photon-level elevation error that is propagated through the linear fit. The photon elevation error is assumed to be uniform for a given segment, and is estimated as the maximum of the segment RMS error and the robust spread of photons as defined by Smith et al. (2019). This robust spread is based on the vertical distribution of signal photon heights and the estimated rate of background photons (i.e., photons that are not surface signals).

For coastal applications, a high along-track resolution is preferable to capture abrupt elevation changes at the shoreline. However, shorter segments may not provide enough photons for

a robust linear fit, and may result in height estimates that are subject to along-track variations in photon density. A longer segment length results in a smoother profile, at the cost of not capturing small-scale features. In order to strike a balance between these two considerations, we implemented the SlideRule ATL06 algorithm for 10-m long segments spaced every 2 m along track, such that consecutive segments overlapped by 80%. A 10 m section was only considered valid if it contained at least five signal photons and if those photons were distributed over at least 1 m along-track. Bright surfaces such as surface ponds can lead to afterpulses in the ATL03 data, which appear as secondary surfaces starting $\sim$0.45 m below the true surface (Arndt and Fricker, 2024; Lu et al., 2021). The original ATL06 algorithm sets the minimum height of the outlier window to be 3 m, which leads to the inclusion of these afterpulses in the final surface elevation estimate. To avoid including afterpulses in our analysis, our custom ATL06 processing allows for an outlier window height as narrow as 0.80 m (i.e., 0.4 m above and below the identified surface).

To estimate shoreline change from our custom ICESat-2 elevation profiles, we needed to reliably identify shoreline boundaries from derived elevation profiles. The presence of sea ice and snow in three of the ICESat-2 tracks prevents the accurate identification of a land-water boundary. Instead, we identified the boundaries of the backshore, defined here as the relatively steep region between the beach or ocean and the onshore region. We manually identified the point corresponding to the backshore/onshore boundary (henceforth referred to as the "upper shoreline") and backshore/beach boundary (the "lower shoreline") based on the visual breaks in the along-track slope (see Fig. 2.9). Since beaches in this region are very narrow when present (Gibbs and Richmond, 2015), we expect the lower shoreline from ICESat-2 to be similar to the land-water boundary. We identified the intersection between each ICESat-2 track and the corresponding imagery-derived shoreline and compared the shoreline positions and cross-shore retreat estimates derived from Planet and the two ICESat-2 boundaries. Under the assumption that the majority of the observed position change in our ICESat-2 boundaries is due to cross-shore change, we projected our ICESat-2-derived change estimate into the local cross-shore direction. The local cross-shore vector was based off of the baseline transect (as defined in Section 3.2) that was located closest to

the geographic midpoint of the four ICESat-2 transects associated with each ground track.

In order to characterize the morphology of each profile, we calculated both the backshore elevation and the backshore slope. The backshore elevation was defined as the elevation difference between the backshore/onshore boundary and the mean offshore (north of the backshore/offshore) elevation from the 02 July 2021 elevation profiles, which we used as a proxy for local sea level (illustrated in Fig. 2.9). The backshore slope was estimated using a linear fit of all points between the backshore/onshore and backshore/beach boundaries, projected into the local cross-shore direction.

To estimate the uncertainty on our ICESat-2-derived boundaries, we use the geolocation uncertainties estimated by Luthcke et al. (2021), who co-registered ATL03 data with Arctic DEM and reported the distribution offsets between the original and shifted locations for each beam. We consider the total uncertainty, defined as the mean offset plus one standard deviation for each beam. This total uncertainty ranges from 2.8 m to 4.8 m for individual beams. We consider the 'worst case' scenario where this error is entirely in the cross-shore direction. The satellite performs a 'yaw flip' twice every 502 days where it is re-oriented by 180 degrees (Luthcke et al., 2021). This means that the specific beam sampling a given ground track, and therefore the associated geolocation uncertainty, alternates between repeats. We take the uncertainty in the shoreline change between two observation dates as the sum in quadrature of the uncertainties of the individual measurements, and find that they range from 4.0 m to 5.9 m.

2.3 Results

2.3.1 Environmental conditions

We observed the most extreme environmental conditions by all measured metrics in 2019 (Table 2.2). The 2019 erosion year had the longest open water season, with sea ice breaking up sooner (late June) and re-forming later (mid-November) than in the other 2 years. It also had the highest wave energy, the most storms, higher air temperatures, and over twice as many ocean thawing degree days. By contrast, the 2021 open water season was the shortest, with sea ice breakup occurring in late July (although ERA5 suggests a one-day ice breakup on 27 June) and freeze-up

Table 2.2: Summary of environmental variables from ERA-5 (Hersbach et al., 2020)

Year	2019	2020	2021
Open water duration	27 June – 13 November	10 July – 26 October	July – 20 October
Open water days	138	111	91
Cumulative wave energy (m^2-days)	113.9	74	58.9
Number of extreme wave events (hours)	263	180	122
Mean air temperature (June – October) (°C)	3.4	1.6	1.8
Mean ocean temperature (open water season) (°C)	3.1	1.8	2.3
ADDT air (°C-days)	583.8	359.1	404.9
ADDT ocean (°C-days)	434.1	210.6	214

occurring in late October 2021 saw slightly warmer ocean and air temperatures but lower wave activity (in terms of both wave energy and hours of high waves) compared to 2020.

2.3.2 Imagery-derived shoreline position and retreat rates

The spatially averaged shoreline change rate in our study area was by -16.5 m a^{-1} (corresponding to retreat) between 2019 and 2021, with notable year-to-year and local variability (Table 2.3, Fig. 2.3). 2019 had the most shoreline loss, with a mean shoreline change of -23.7 m and single-segment (i.e. 10 m scale) shoreline change values as extreme as -66.7 m. 2020 experienced more moderate shoreline change, with a mean shoreline change of -15.4 m (ranging from -41.0 m to +6.0 m). 2021 experienced similar but slightly lower rates, with a mean shoreline change of -10.5 m (-30.9 m to +5.6 m).

Based on the uncertainty estimation described in Section 2.3, we estimated the precision of our shoreline positions estimates to be 2.2 m. Assuming that the error in each shoreline is independent of the others, this corresponds to a position change uncertainty of 3.1 m. We define substantial shoreline change as any value that exceeds this threshold.

Our shoreline change estimates for each region (Table 2.3, Fig. 2.3 b.) indicate that there was spatial variability between regions. Region 1 showed high retreat, with a mean change rate of -12.9 m a^{-1} over 3 years and single-segment year-to-year shoreline change estimates ranging from -29.4 m to +1.6 m. Shoreline change consisted almost exclusively of retreat, with the maximum observed

advancement (+1.6 m) falling below our estimated uncertainty threshold (3.1 m). We observed the greatest spatially averaged retreat in 2019 (-18.5 m), and the lowest in 2021 (-7.1 m). While every shoreline segment in region 1 underwent retreat in 2019 and 2020, 16% of valid shoreline segments (all in the western half of Region 1) did not exhibit substantial (¿ 3.1 m) shoreline change in 2021.

Region 2 exhibited the largest overall retreat, with a 3-year spatially averaged mean change rate of -24.3 m a^{-1} and year-to-year single-segment change estimates ranging from -58.2 m to -3.0 m. As with Region 1, we observed the largest amount of shoreline change in 2019 (-38.4 m), with similar and smaller change in 2020 (-16.8 m) and in 2021 (-17.7 m).

Region 3 exhibited the smallest amount of shoreline change, with a 3-year spatially averaged rate of -6.0 m a^{-1}. Region 3 was the only region in our study area where substantial shoreline advance (up to +18.6 m locally in 2019) occurred. Although 2019 was not the year with the highest spatially averaged shoreline change (-0.6 m) in Region 3, it was the most dynamic year, with both the maximum observed local retreat (-66.7 m of shoreline change) and advance (+18.6 m of shoreline change). We found that 24% of valid shoreline segments, concentrated almost exclusively in the easternmost third of the region, underwent significant retreat, whereas the central 62% of shoreline segments experienced substantial advance. The remaining 14% did not exhibit substantial retreat or advancement. In 2020, the mean shoreline change across the region was higher (-13.5 m), but the change at individual segments was lower in magnitude (with a local maximum of -41.0 m) and spread over a larger area (the eastern 66% of the basin). Only 3% of shoreline segments showed substantial advancement, whereas the remaining 31% experienced no significant change. Relative to 2020, retreat in 2021 was lower in magnitude (with a maximum shoreline change of -20.7 m) and present across less of the region (40%) , resulting in a lower spatially averaged shoreline change (-3.9 m). 19% of segments showed significant advancement (with a maximum of +5.6 m), whereas the remaining 41% experienced no significant change.

Table 2.3: Estimated shoreline change between each successive image observation date in each of the three regions identified in Figure 3, as well as across the whole study area. The mean and range are listed.

Year	Region 1	Region 2	Region 3	Total
2019	-18.5 m (-29.4m – -7.0 m)	-38.4 m (-58.2 m – -15.7 m)	-0.6 m (-66.7 m – +18.6 m)	-23.7 m (-66.7 m – +18.6 m)
2020	-13.0 m (-21.6 m – -3.4 m)	-16.8 m (-27.6 m – -3.0 m)	-13.5 m (-41.0 m – +6.0 m)	-15.4 m (-41.0 m – + 6.0 m)
2021	-7.1 m (-14.2 m – +1.6 m)	-17.7 m (-30.9 m – -5.6 m)	-3.9 m (-20.7 m – +5.6 m)	-17.7 m (-30.9 m – +5.6 m)
2019-2021	-12.9 m (-29.4 m – +1.6 m)	-24.3 m (-58.2 m – -3.0 m)	-6.0 m (-66.7 m – +18.6 m)	-16.5 m (-66.7 m – +18.6 m)

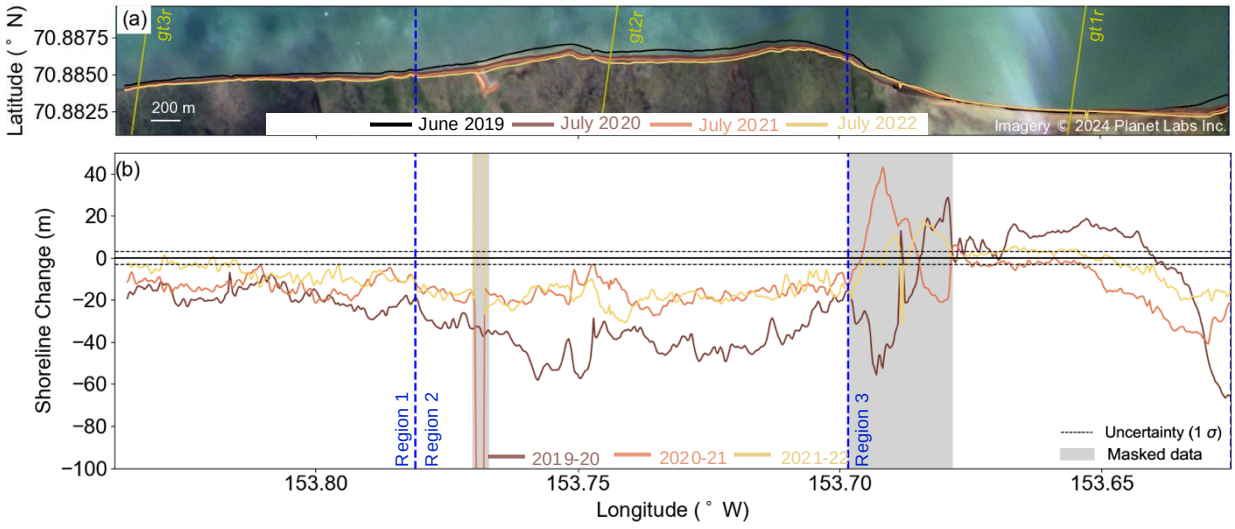


Figure 2.3: (a) Shorelines derived from Planet images, overlain on imagery from 07/25/2020 (©2024 Planet Labs Inc). The locations of the three ICESat-2 ground track are also shown. (b) Cross-shore shoreline change calculated between successive years. Areas where there was an ambiguous land/water boundary are masked out (shaded areas) and excluded from analysis. The boundaries of the three regions shown in Fig. 2.1 are shown as dashed lines.

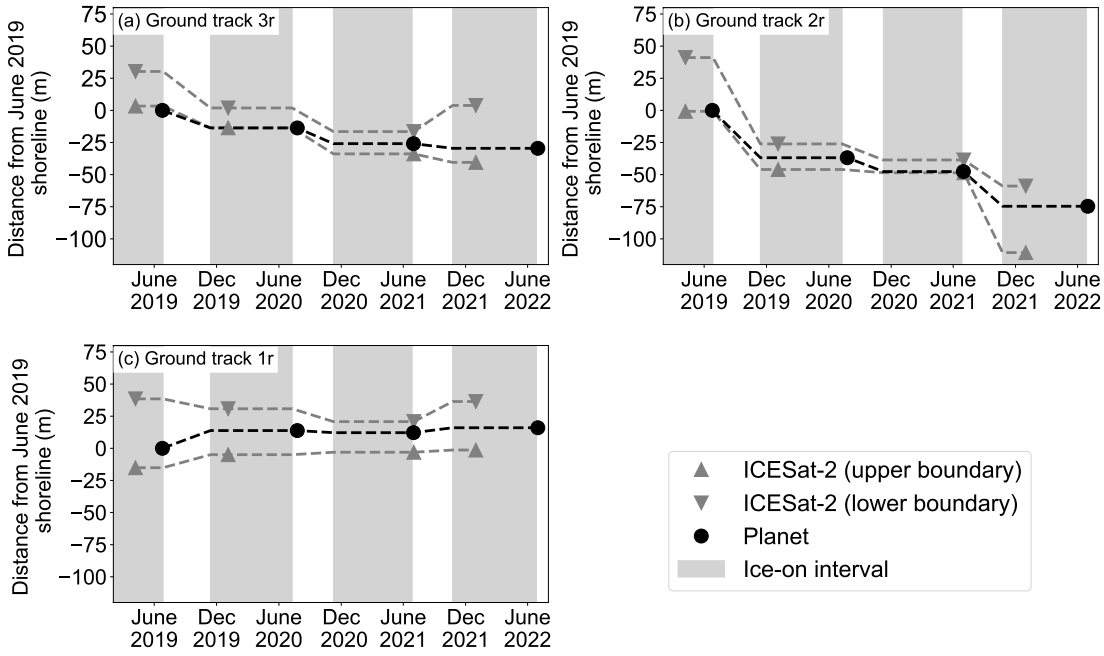


Figure 2.4: Time series of the position of upper and lower boundaries and coastal boundaries from ICESat-2 and the land-water boundary derived from Planet. Positions are given as the cross-shore distance from the Planet-derived shoreline from 25 June 2019. Ice-on intervals are shaded. Dashed lines indicate the trajectory of the shoreline based on a linear rate of change during the open water season and no change during ice-on periods.

2.3.3 Cross-validation of ICESat-2 altimetry and Planet imagery-derived shoreline positions

Altimetry from ICESat-2 provides an independent estimate of shoreline change at multiple positions along the shoreline profile, which can be compared to Planet-derived shoreline positions for validation. We find that overall shoreline positions estimated from both datasets are consistent. We would expect the land-water boundary from Planet to be located seaward (north) of the lower backshore boundaries identified by ICESat-2. However, we found that the Planet-derived land-water boundary consistently falls landwards (south) of the ICESat-2-derived lower boundary (by 8.6 $\pm$ 4.2 m to 41.1 $\pm$ 4.5 m) and either seawards (by up to 36.0 m $\pm$ 4.5 m) or slightly landward of the ICESat-2-derived upper boundary (by up to 3.3 $\pm$ 4.0 m) (Fig. 2.4), such that it is located on the backshore or onshore section of the elevation profiles. Given the published geolocation errors from ICESat-2 (up to 4.8 m, Luthcke et al. (2021)) and Planet ($<$ 10 m, Planet Team (2023)), the difference between ICESat-2 and Planet derived shorelines is not thought to be due to a consistent

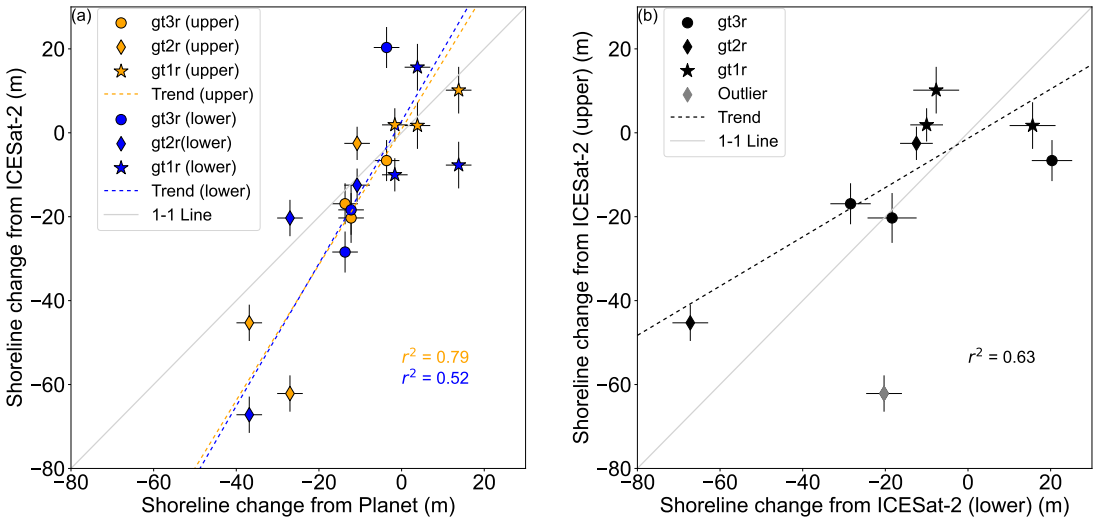


Figure 2.5: a) Comparison between shoreline change estimates from Planet and shoreline change estimates from the upper (orange) and lower (blue) boundaries derived from ICESat-2. b) Comparison between the measured change between each open water season across the upper and lower boundaries derived from ICESat-2. The coefficient of determination excluding the outlier drained lake measurement (grey) is reported. Linear fits were estimated using orthogonal distance regression. A 1-1 line is shown for reference.

geolocation offset between the two satellite estimates. The difference could be explained by a consistent landward bias in our NDWI thresholding technique (Section 2.3) or differences introduced by snow cover and variations in the local water level. Although observations from ICESat-2 and Planet span different time intervals (Table 2.1, Fig. 2.4), the number of open water days spanned by both are similar, allowing for a direct comparison between our imagery and altimetry-defined shoreline change estimates. We perform an orthogonal distance linear regression and find a high correlation between the Planet-derived change estimates and changes in the ICESat-2-derived upper boundary (r^2 = 0.79, p = .0008) and moderate correlation with the ICESat-2-derived lower boundary (r^2 = 0.52, p = .007) (Fig 2.5 a.).

2.3.4 Topographic change from satellite altimetry

Our SlideRule-derived elevation profiles (Fig. 2.6 b., Fig. 2.6 d. and Fig. 2.6 f.) fit the ATL03 photon data well, with RMS errors ranging from 0.04 m to 1.3 m and a mean RMS error

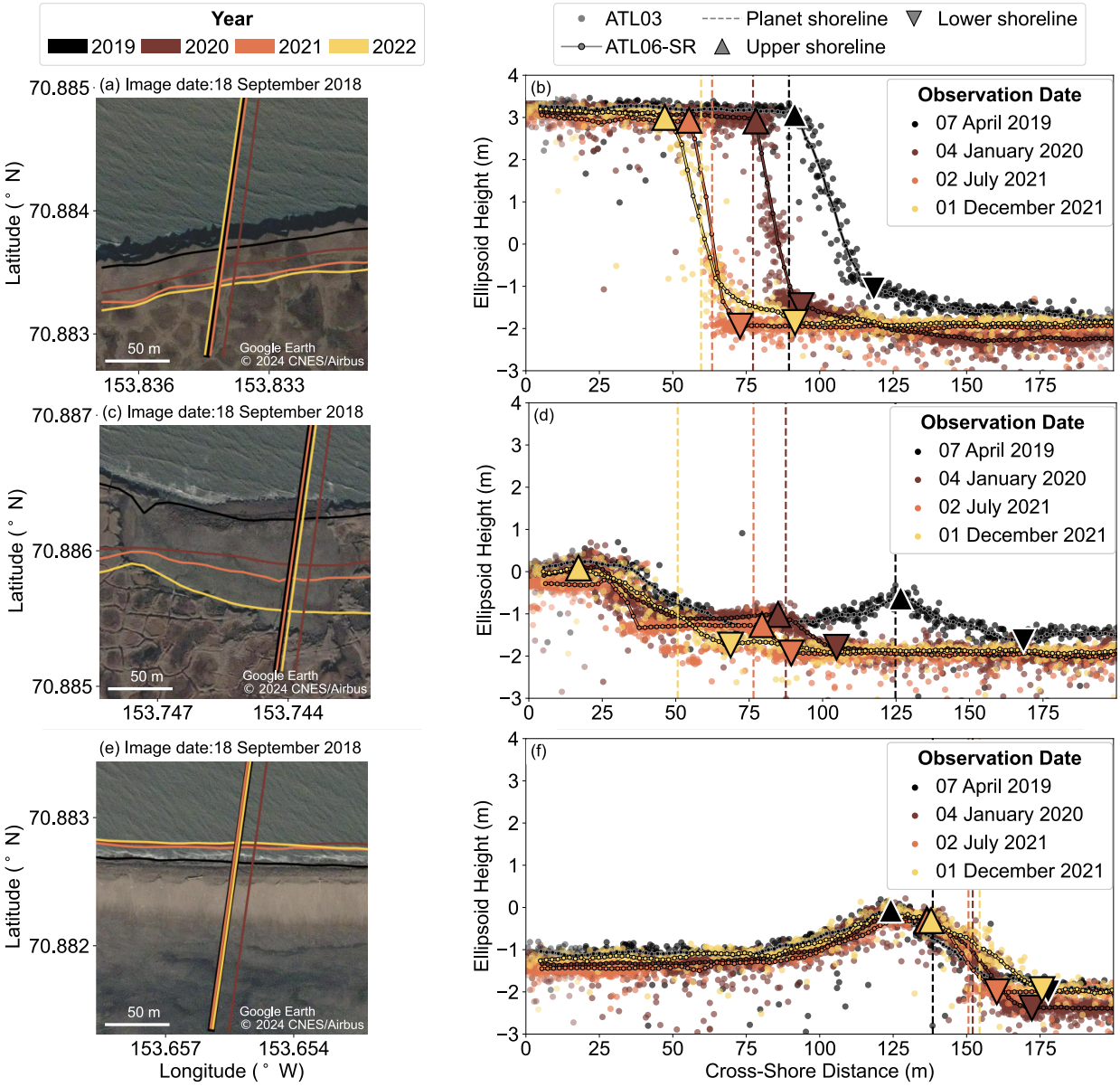


Figure 2.6: (a), (c), (e):Detailed view of the ICESat-2 sampling location from 2018 satellite imagery (©2024 Google Earth CNES/Airbus) for (a) ground track 3r; (c) ground track 2r and (e) ground track 1r . The location of the Planet shoreline and corresponding ICESat-2 pass for each year is shown. (b), (d), (f): ATL03 photon clouds from each ICESat-2 pass, with the SlideRule-derived (ATL06-SR) elevation profile overlaid on the photon clouds for (b) ground track 3r; (d) ground track 2r; and (f) ground track 1r. The estimated location of the upper and lower shoreline boundary for each date is marked, along with the cross-shore locations of the Planet-derived shorelines. The colors follow the same legend as (a), (c), and (e).

Table 2.4: Onshore heights and slopes derived from the identified upper and lower boundaries for each ICESat-2 observation.

Track	Date	Backshore elevation (m)	Backshore slope (%)
Ground Track 3r (Region 1)	07 April 2019	5.02	15
	04 January 2020	4.87	28
	02 July 2021	4.89	28
	31 December 2021	4.96	11
Ground Track 2r (Region 2)	07 April 2019	1.33	2.4
	04 January 2020	0.93	3.9
	02 July 2021	0.70	6.7
	31 December 2021	2.04	3.5
Ground Track 1r (Region 3)	07 April 2019	1.89	3.6
	04 January 2020	1.67	5.9
	02 July 2021	1.64	7.0
	31 December 2021	1.64	4.3

of 0.15 m (Fig. 2.10, Fig. 2.11, Fig. 2.12). The propagated vertical uncertainty ranges from 0.0024 to 0.27 m, with a mean uncertainty of 0.029 m. We now discuss the time evolution of the shoreline horizontal position (Table 2.4), backshore elevation, and backshore slope (Table 2.4) at each ICESat-2 ground track.

Ground track 3r in Region 1 (Fig. 2.6 a., Fig. 2.6 b., Fig. 2.4a.) shows a coastal bluff (such as the one shown in Fig. 2.13a.) that undergoes retreat with little change in morphology. The upper and lower shoreline boundaries show consistent retreat in 2019 and 2020, with north-south change at each boundary ranging from -16.9 m to -28.4 m. During these 2 years, we observed a steepening of the backshore slope from 15% in 2019 to 28% in 2020 and 2021. In July 2021, we note a cluster of photons that is $\sim$1 m high and $\sim$5 m across at the base of the bluff (Fig. 2.7a.) that may correspond to toppled bluff material. Between 2021 and 2022, we observed slight retreat of the upper boundary (-6.6 m of shoreline change) and advancement of the lower boundary (+20.3 m), resulting in a reduction in the backshore slope to 11%. In December 2021, we again note a $\sim$1 m high cluster of photons at the base of the bluff, that gently slopes down towards the mean offshore height over $\sim$20 m (Fig. 2.7a.). The backshore elevation remains stable, ranging from 4.89 m to 5.02 m over the 3 year study period.

Ground track 2r (Fig. 2.6 c., Fig. 2.6 d. Fig. 2.4b.) in Region 2 passes over the remnant

basin of a ∼150 m diameter lake that was breached and drained as a result of shoreline retreat prior to our study. This profile undergoes large changes in both the shoreline position and morphology. Aerial imagery from ShoreZone (Fig. 2.13b.) showed the lake pre-drainage, and the lake basin was clearly visible in Airbus imagery from Google Earth (Fig. 2.6c.) and in our 2019 ICESat-2 profile (Fig. 2.6d.). Between 2019 and 2020, -45.3 m of upper-shoreline change and -67.2 m of lower shoreline change occurred, corresponding to the loss of about half of the basin. This resulted in a 0.40 m drop in the backshore height from 1.33 m to 0.93 m and an increase in the backshore slope from 2.4% to 3.9%. By contrast, between early 2020 and early 2021 there was almost no change in the upper shoreline position (-2.5 m) and only moderate change in the lower shoreline position (-12.5 m), resulting in a further increase in the backshore slope to 6.7%. We also observe a slight lowering of 0.23 m of the backshore height. The photon distribution over the lake basin in July 2021 is concentrated in a narrow height band, with a secondary reflection below the surface (Fig. 2.7b.). This feature is indicative of an afterpulse due to surface ponding (Lu et al., 2021), suggesting the presence of shallow water. The rest of the lake basin was eroded between July and December 2021, resulting in -62.1 m of change of the upper shoreline and -20.3 m of change of the lower shoreline. This necessitated the definition of a new, substantially higher (2.04 m) backshore boundary and resulted in a shallowing of the backshore slope from 6.7% to 3.5%.

Ground track 1r (Fig. 2.6 e., 2.6 f., Fig. 2.4c.) in Region 3 passes over a 1.71 m high dune in front of a $\sim$ 2.6 km-wide breached thermokarst lake (shown in more detail in Fig. 2.13c.) that shows little shoreline change relative to other regions. We observed between +1.7 m and +10.2 m of advance in the upper boundary each year, while the lower boundary retreated in 2019 (-7.7 m) and 2020 (-10.0 m) and then advanced in 2021 (+15.6 m). We note a 0.22 m drop in the backshore elevation (from 1.89 m to 1.67 m) between 2019 and 2020, after which the elevation remains stable from 2020 to late 2021 (1.64 m to 1.67 m). The backshore slope steepens between 2019 and 2021 from 3.6% to 7.0 %, and then relaxes to 4.3% in late 2021.

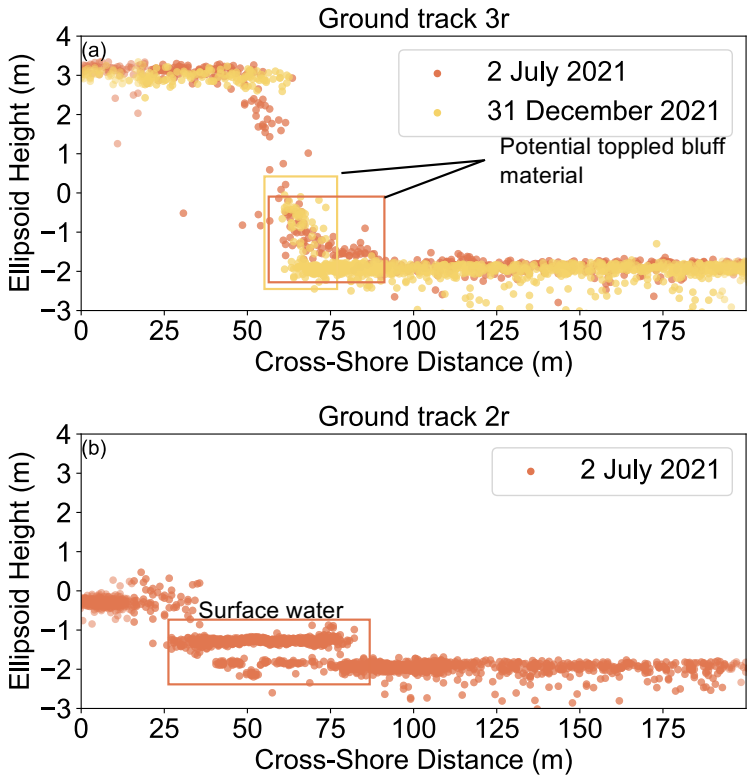


Figure 2.7: ICESat-2 ATL03 photon data show small-scale features, including (a) returns over what may be a toppled block material at the base of the bluff at ground track 3r and (b) Surface ponding in the drained lake basin at ground track 2r.

2.4 Discussion

2.4.1 Spatiotemporal variability in shoreline change in the context of previous observations

Our estimates of spatially averaged (regional) mean annual shoreline change (-10.5 m a^{-1} to -23.7 m a^{-1}) across our study region are higher than long-term historical estimates and similar to recent observations (Fig. 2.14). Gibbs and Richmond (2015) estimated a regional mean of -6.3 m a^{-1} and a local maximum of -18.6 m a^{-1} between Drew Point and Cape Halket between 1947 and 2002. Jones et al. (2009) estimated shoreline change across this region over multiple time intervals and found -6.8 m a^{-1} of change between 1955 and 1979, -8.7 m a^{-1} between 1979 and 2002, and -13.6 m a^{-1} between 2002 and 2007. A follow-up study by Jones et al. (2018) estimating shoreline change over a 9 km region covering our study area found a 10-year mean shoreline change rate of -17.2 m a^{-1} between 2007 and 2016. In addition to estimating a 10-year mean, Jones et al. (2018) reported regional year-to-year rates, which ranged from -6.7 m a^{-1} to -22.6 m a^{-1}. Our mean retreat rates in 2020 and 2021 fall within the range of year-to-year rates observed by Jones et al. (2018) whereas our mean retreat in 2019 (-23.7 m) slightly exceeds that range. Our 3-year mean of observed retreat rates (-16.5 m) is similar to the decadal-scale estimate from Jones et al. (2018), and consistent with an increase in local shoreline change rates compared to 2002-2007 (Jones et al., 2009). Our retreat estimates and the post-2002 estimates of Jones et al. (2009) and Jones et al. (2018) are all higher than the pre-2002 decadal-scale estimates of Gibbs and Richmond (2015) and Jones et al. (2009). This increase could be reflective of a long-term increase in retreat rates, although it may also be due to differences in time scales between studies, as short-term estimates of shoreline change tend to be higher in magnitude than long-term estimates (Sadler and Jerolmack, 2015).

Previous observations suggest that the spatial distribution of change rates across our study area has been variable over time. Gibbs and Richmond (2015) found the highest rates of shoreline change in Region 3 (-10 m a^{-1} to -18 m a^{-1}), intermediate rates in Region 2 (-8 m a^{-1} to -12 m a^{-1}), and slightly lower rates in Region 1 (-6 m a^{-1} to -12 m a^{-1}) between 1947 and 2002. Jones et al. (2009) found a similar pattern between 1955 and 1979, with the shoreline change in Region 3

occurring at rates in excess of -10 m a^{-1} and shoreline change in most of Regions 1 and 2 occurring at rates between -5 m a^{-1} and -10 m a^{-1}. However, they found that shoreline change rates in Region 2 increased to be in excess of -10 m a^{-1} between 1979 and 2002, and change rates in Region 1 followed suit between 2002 and 2007, such that change rates across the region were relatively uniform (averaging -18 m a^{-1}) between 2002 and 2007.

In contrast, our observed shoreline change rates between the three regions between 2019 and 2021 are not uniform. Although the relatively high rates of retreat we observed in Region 2 compared to Region 1 is consistent with Gibbs et al. (2019) and Jones et al. (2009), the stability of the central portion of Region 3 that we observed with both ICESat-2 altimetry and Planet imagery appears to be a recent development. Wang et al. (2022) sampled a transect across the central portion of Region 3 from satellite imagery-derived shorelines from 1974, 1985, 1992, 2001, 2009, and 2017 and estimated a mean shoreline change rate over the full study period of -55.9 m a^{-1}. When considering the rates between successive shorelines, Wang et al. (2022) found that 2009–2017 was the only time interval during which there was no observed shoreline change, suggesting that stabilization occurred in this time frame after over 4 decades of retreat.

2.4.2 Drivers of spatiotemporal variability in imagery-derived shoreline change

Jones et al. (2018) found that the environmental drivers of year-to-year variability on the Beaufort Sea Coast are not well-defined, but they did observe high retreat in years with extreme weather, which is consistent with our findings of both high retreat and extreme environmental conditions in 2019. Compared to 2020 and 2021, 2019 had a long open water season and elevated air and ocean temperatures (Table 2.2), all of which likely contributed to the elevated spatially averaged retreat across the study region.

Although there is correspondence between mean year-to-year shoreline change and year-to-year variations in wave and temperature conditions, the response of the shoreline to these time-varying conditions is not spatially uniform (Fig. 2.3 b.). In 2019, Region 1 and Region 2 both experienced high retreat, while Region 3 underwent high retreat across parts of the shorelines and

moderate advancement across others. Whereas we do not expect air and ocean temperatures to vary greatly spatially over the study region, local variations in wave energy due to shoreline orientation, position, and morphology may contribute to the observed spatial variability. For indented shorelines such as our study area, wave energy is expected to be concentrated towards the headlands due to wave refraction, such that shorelines with uniform composition will straighten over time (Van Rijn, 2011). This provides a potential explanation for increased retreat in Region 2, particularly in 2019 when wave action was high. 2021 saw the lowest amount of wave energy and fewest storms (Table 2), and the concentration of wave energy in the headlands of Region 2 would result in particularly low wave energy in the hinterlands of Region 1 and Region 3. We note that while Region 1 and Region 2 both consist primarily of ice-rich coastal bluffs, the shoreline in Region 3 is characterized by ShoreZone primarily as low-lying peat (Fig. 2.1 b.) that is expected to be subject to low incident wave energy (Harper and Morris, 2014). The eastern edge of Region 3 is characterized as inundated tundra, which refers to areas where thaw subsidence and surface ponding are present (Harper and Morris, 2014). Based on these characterizations and our observed patterns shoreline change, we posit that shoreline change in Region 1 and Region 2 is sensitive to year-to-year variations in wave energy and ocean and air temperatures, while the western and central portion of Region 3 are not. The eastern portion of Region 3 (inundated tundra) is likely subject to ground thaw, high wave energy and flooding, resulting in high retreat in response to high wave activity and high temperatures. The advancement observed in Region 3 may be driven by along-shore transport of material lost from the surrounding regions.

2.4.3 Drivers of morphologic change observed from ICESat-2 altimetry

The elevation profiles from ICESat-2 data provide additional information on topographic and morphological change at specific ground tracks (Table 2.4), which can provide insight on specific erosion and accretion processes that drive local shoreline change. Specifically, we consider changes in backshore elevation, backshore slope, and relative change between the upper and lower shoreline boundaries.

Based on previous studies in the Beaufort Sea Coast area (e.g., Barnhart et al., 2014; Overeem et al., 2011), we infer that the coastal bluff shown in ground track 3r in Region 1 (Fig. 2.6 b.) likely retreats primarily through the formation of thermal erosional niches, followed by bluff collapse. As the shoreline retreats, we observed no major morphological change; the backshore slope remained 10% with a stable (4.87 m to 5.02 m) backshore elevation. However, there were year-to-year fluctuations in the backshore slope due to differences in change rates at the upper and lower boundaries of the backshore. In particular, the relatively low slope (11%) in December 2021 is driven by a retreat of the upper boundary (-6.6 m of shoreline change) coupled with advance of the lower boundary (+20.3 m of shoreline change) (Table 2.4). Based on the ICESat-2 ATL03 photon data from July and December 2021 (Fig. 2.7a.), we hypothesize that this reduction in slope is due to the accumulation of collapsed bluff material at the base of the cliff that is not removed by the end of the 2021 open water season. The low retreat derived from altimetry in 2021 is consistent with the low retreat estimated from Planet imagery in the broader Region 1 (which has a spatially averaged mean shoreline change of -7.1 m) and is possibly due to relatively low wave energy and fewer storms in the 2021 open water season (Table 2.2). It may be that multiple locations along the shoreline in Region 1 observed in imagery were sheltered by uneroded toppled bluff material similar to what we observe at ground track 3r.

The drained lake basin captured by ground track 2r in Region 2 (Fig. 2.6 d.) is an example of a more complex feature, which displays variable retreat as the shoreline migrates from the lake basin boundary to the bluff on the southern edge. The transition in shoreline morphology is reflected in an increase in backshore elevation from 0.70 m to 2.04 m and moderate fluctuations in the backshore slope (2.4 % to 6.7 % ; Table 2.4). The changes in slope between 2019 and 2020 and between early and late 2021 were driven by high and variable change (-20.3 m to - 67.2 m) in both the upper and lower boundaries, while the steepening of the slope between 2020 and 2021 was driven by retreat of the lower shoreline (-12.5 m of shoreline change) and little change in the upper shoreline (-2.5 m).

In order to assess whether the presence of this lake basin impacts local retreat rates, we compared the mean Planet-derived shoreline change across the drained lake basin (which spans

15 segments over 150 m) to the distribution of Planet-derived shoreline change across the entirety of Region 2. In 2019, the mean shoreline change across the lake basin (-35.3 m) is similar to retreat in the Region 2 overall, as it falls in the 63rd percentile of observed change. However, in 2020 shoreline change across the basin (-10.5 m) fell into the 8th percentile of observed headlands change, and in 2021 it was in the upper 90th percentile (-23.1 m). This suggests that the presence of the drained lake basin may have contributed to differential erosion during 2020 and 2021 relative to Region 2 overall. Differential erosion rates in drained lake basins have been observed before, with Jones et al. (2009) observing generally higher retreat rates of recently drained lake basins in this region between 1955 and 2002 relative to other land types (although this trend did not hold between 2002 and 2007). They suggested that the low elevation and presence of thawed sediments likely makes drained lake basins more susceptible to erosion than coastal bluffs. Our observation of surface water in July 2021 (Fig. 2.7 b.) is consistent with this interpretation, as it would help keep the underlying sediments in this basin thawed.

Based on our observations and the theory presented in Jones (2009), we can infer the processes driving the 3-year evolution of the drained lake basin. In 2019, wave-driven erosion of the seaward side of the drained lake basin exposed low-lying thawed sediments. In 2020, debris from this large erosion event may have sheltered the remainder of this basin, as evidenced by the retreat at the lower boundary and stability of the upper boundary. Once this debris was removed by waves, the low backshore elevation (0.70 m) would have left the basin susceptible to overtopping by high waves, and the thawed sediments would have low mechanical strength, making the basin susceptible to rapid erosion as observed between early and late 2021. The steeper backshore slope in 2019 compared to 2021 may have also contributed to increased wave run-up (Earlie et al., 2018) and therefore increased mechanical erosion.

Both the upper and lower shoreline positions at ground track 1r in Region 3 (Fig. 2.6 f., Fig. 2.4 c.) are relatively stable, whereas the other ground tracks exhibit high retreat. We see moderate advance (+10.2 m of shoreline change) and a drop in elevation (-0.22 m) of the backshore boundary in 2019, but very little change in either the position (+1.7 m to +1.9 m, which falls within our

estimated uncertainty) or elevation (which ranges from 1.64 m to 1.67 m) of the backshore over the next 2 years. Fluctuations in the slope between observation dates are driven primarily by changes in the lower boundary (which undergoes between -10.0 and +15.6 m of shoreline change per year), which is consistent with sediment deposition and removal at the beach in front of the lagoon or changes in snow cover.

In order to understand the relative rates of retreat at the upper and lower boundaries of the shoreline, we perform an orthogonal distance regression between the annual change at both boundaries (Fig. 2.5b.). We exclude change for the drained lake basin between July and October 2021, where the collapse of the remaining lake basin necessitated the definition of new upper shoreline boundary. We find a moderate correlation between upper and lower shoreline boundary change (r^2 = 0.63, p = .009) and a slope of 0.59 in the linear fit. Thus, both boundaries exhibit comparable amounts of change, but the lower shoreline (the interface between the backshore, beach, and ocean) is more dynamic.

2.4.4 Potential and challenges using ICESat-2 for shoreline characterization

Analyses of both the geolocated photon data and derived elevation profiles from ICESat-2 provide valuable insight on shoreline change. ICESat-2's geolocated photon product resolves coastal topography with a high level of detail, capturing abrupt elevation changes over horizontal distances of 5 m or less (e.g. Fig. 2.6 b.). We observe process-scale features such as toppled blocks and surface ponds in snow-free ICESat-2 profiles (Fig 2.7). We find that the simplified elevation profiles derived via SlideRule can adequately capture the shoreline for assessing shoreline evolution, although small-scale features such as the toppled block on ground track 3r (Fig. 2.7 a.) and surface ponding on ground track 2r (Fig. 2.7 b.) are lost. ICESat-2 profiles allow for the identification of multiple shoreline boundaries, which can be compared against imagery-derived shoreline positions (Fig. 2.4, Fig. 2.5 a.). Furthermore, analysis of morphologic parameters such as backshore height and backshore slope can provide insight on specific erosional and accretional processes, such as the collapse of the small drained lake and the presence of toppled blocks at steep coastal bluffs.

The highest RMS misfit between the SlideRule-derived elevation profiles and underlying photons occur in areas with steep slopes and abrupt elevation changes (Fig. 2.10, Fig. 2.11, Fig. 2.12). This is particularly apparent for ground track 3r (Fig. 2.10), where the upper shoreline boundary inferred from SlideRule often appears 2 m to 5 m southward of the boundary that would be visually inferred from ATL03. The 10 m section length we used in SlideRule is likely too coarse to adequately capture abrupt elevation changes, but a shorter segment length would have relied on fewer photons per segment and therefore be more sensitive to variations in along-track photon density. An adaptive approach based on local topography and photon density may be able to capture steep and complex features more accurately.

Given the seasonal revisit time of ICESat-2 over our study region, the high frequency of cloud cover in the summer and fall, and the low reflectivity of the snow-free tundra, the majority of usable ICESat-2 data occurs in winter and spring, when snow and sea ice are present. Snow cover will impact ICESat-2-based shoreline position estimates, particularly the location of the lower shoreline boundary, which will in turn impact our slope estimates. Although we expect the magnitude of snowcover-induced changes to be small relative to the large erosion events observed at the ground track 3r (the coastal bluff) and the ground track 2r (the small drained lake), it may be the dominant source of change in areas with lower rates of change, such as the ground track 1r (the large breached lake). Future work comparing snow-on ICESat-2 tracks to snow-off ICESat-2 tracks and snow-off digital elevation models could help quantify snow distribution at the shoreline and its impact on shoreline position estimates. There is also up to 15 m of horizontal offset between repeat ICESat-2 profiles (Fig. 2.6a., Fig. 2.6c., Fig. 2.6e.), meaning that differences in shoreline position may in part be due to different sampling locations.

2.5 Conclusions

We used multispectral imagery from Planet and altimetry data from ICESat-2 to highlight spatiotemporal variability in changes in the position and topography of the shoreline along a dynamic section of the Beaufort Sea Coast near Drew Point, Alaska, USA. We found km-scale variability

in annual shoreline change that reflects the response of distinct geomorphic units to time-varying wave and temperature conditions and small-scale variability ($\sim$10s of m) that may be influenced by local shoreline morphology. We used elevation profiles from ICESat-2 altimetry to track changes in the position, elevation, and cross-shore slope of the shoreline at three ground tracks. We found that each ground track samples a distinct shoreline type that is subject to different mechanisms of change. At ground track 3r (Region 1) and ground track 1r (Region 3), we observed changes in shoreline position that are consistent with adjacent imagery-derived estimates, and analysis of changes in morphological parameters (namely elevation and slope) helped to illustrate specific processes (such as rapid bluff retreat, sheltering of bluffs by collapse bluff material, and sediment accumulation/deposition) that drive the observed shoreline change. Ground track 2r in Region 2 illustrates how a small-scale feature (in this case a drained lake basin) can be subject to different processes than the surrounding area, leading to locally variable retreat.

Overall, we found that annual retreat rates from both datasets are consistent with recent estimates of shoreline change over the last decade and that current spatial patterns of retreat differ from long-term trends, particularly in Region 3. Planet imagery and ICESat-2 altimetry provided complementary shoreline measurements, with the two datasets producing similar estimates of shoreline position change. Multispectral imagery can provide regular scene-wide estimates of shoreline change that can contextualize ICESat-2 topographic transects with the surrounding shoreline. Altimetry data from ICESat-2 provides cross-shore estimates of topographic change that allow us simultaneously track changes in shoreline position and morphology; this vertical dimension critically provides additional insight into the geomorphic processes driving shoreline change. Small features that are visible in the ATL03 photon data can also aid in the interpretation of short-term processes. By integrating satellite altimetry and multispectral imagery, we can study mechanisms of coastal change that have previously been challenging to identify with satellite remote sensing. Additional datasets such as aerial photography and shoreline classifications from databases such as ShoreZone can also aid in the interpretation of both satellite altimetry and satellite imagery. Retreat rates derived from altimetry and satellite imagery can also be used for cross-validation, and the

ability to estimate both the upper and lower shoreline boundary from altimetry allows us to better interpret our shoreline estimates derived from multispectral imagery.

The regular revisits and dense track sampling of ICESat-2 provides estimates of retreat rates and geometric properties such as elevation and slope over large areas and multiple years. However, bulk analysis of these changes requires a method for systematic processing of ATL03 data to generate simplified elevation profiles and extract relevant parameters. The processing workflow presented here generates elevation profiles that show good agreement with ATL03, but could be improved upon to better capture abrupt elevation changes and small-scale features. Future work should also develop techniques to estimate contributions from snow and topographic offset.

2.6 Code and Data Availability

The ICESat-2 ATL03 geolocated photon product is available at the National Snow and Ice Data Center (NSIDC): https://doi.org/10.5067/ATLAS/ATL03.006. ERA-5 data are available at the Copernicus Data Store: https://doi.org/10.24381/cds.adbb2d47. Aerial photography and shoreline classifications are available at the NOAA Fisheries Alaska ShoreZone Website: https://alaskafisheries.noaa.gov/mapping/sz. Multispectral imagery was provided by Planet Labs under the NASA Commercial Smallsat Data Acquisition Program (CSDA). Derived datasets including shoreline positions and elevation profiles are available at:
https://doi.org/10.5281/zenodo.11095271. The scripts used to generate all results and figures are available at: https://doi.org/10.5281/zenodo.14777816

2.7 Author contributions

MBB was responsible for the design, data analysis, visualization, and preparation of the manuscript. AAB worked with the lead author to conceptualize the research that went into the manuscript, discussed all aspects of the investigation and analysis with the lead author throughout the project, and contributed to review and editing of all drafts of the manuscript. All other authors

were involved in the conceptualization of the project and reviewed and edited all drafts of the manuscript.

2.8 Competing interests

The authors declare that there are no competing interests.

2.9 Acknowledgements

This work was supported by NASA grant no. 80NSSC24K0019 (MB), 80NSSC22K1105 (RJM), and 80NSSC21K0912 (MRS). We thank César Deschamps-Berger and the anonymous referees whose feedback helped refine our manuscript. We also thank the Scripps glaciology group for advice on analyzing and visualizing ICESat-2 data. The Scientific colour map lajolla (Crameri, 2023) is used in this study to prevent visual distortion of the data and exclusion of readers with colour-vision deficiencies (Crameri et al., 2020).

This chapter has been published in full as: Bryant, M. B., Borsa, A. A., Anderson, E. J., Masteller, C. C., Michaelides, R. J., Siegfried, M. R., and Young, A. P. (2025). Multiple modes of shoreline change along the Alaskan Beaufort Sea observed using ICESat-2 altimetry and satellite imagery. The Cryosphere, 19:1825–1847. The dissertation author was the primary researcher and author on this paper. The paper is licensed under a Creative Commons Attribution 4.0 License, which allows for adaptation and re-use with proper attribution.

2.10 Supplementary material

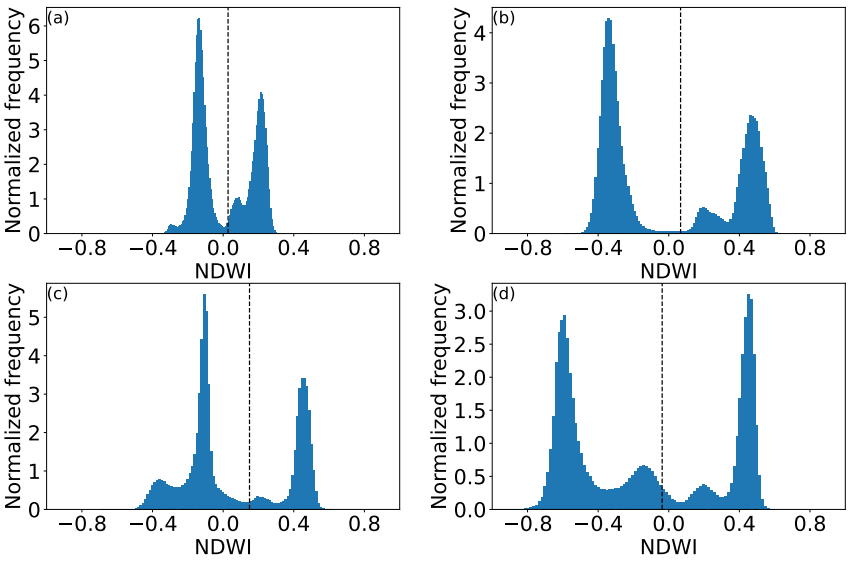


Figure 2.8: Normalized distribution of scene-wide NDWI values for Planet images collected on (a) 25 June 2019, (b) 25 July 2020, (c) 02 July 2021, and (d) 01 July 2022. The threshold used for identifying the land-water boundary, estimated using Otsu's method, is shown as a dashed vertical line.

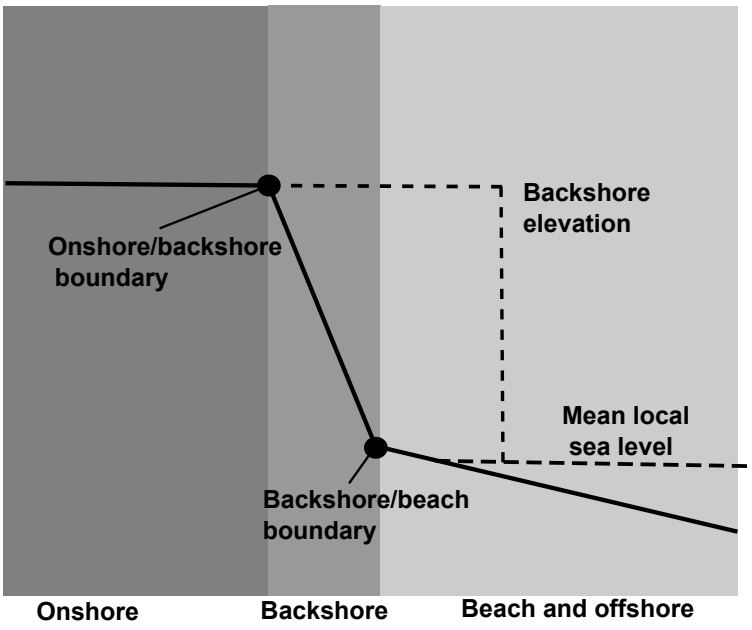


Figure 2.9: Illustration of the boundaries and elevation estimates described in Section 2.4

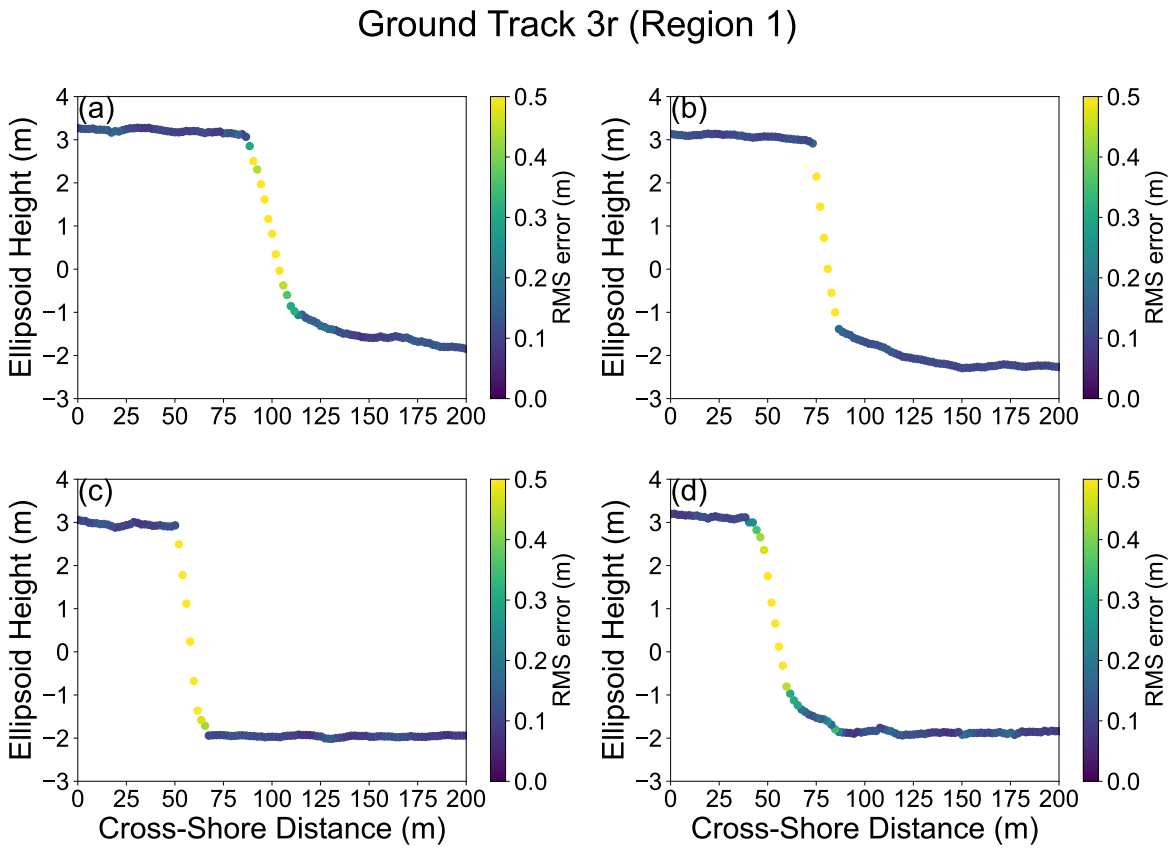


Figure 2.10: RMS error between our SlideRule-derived elevations and the source ATL03 photon information for ground track 3r for (a) 7 April 2019; (b) 4 January 2020; (c) 2 July 2021; (d) 31 December 2021

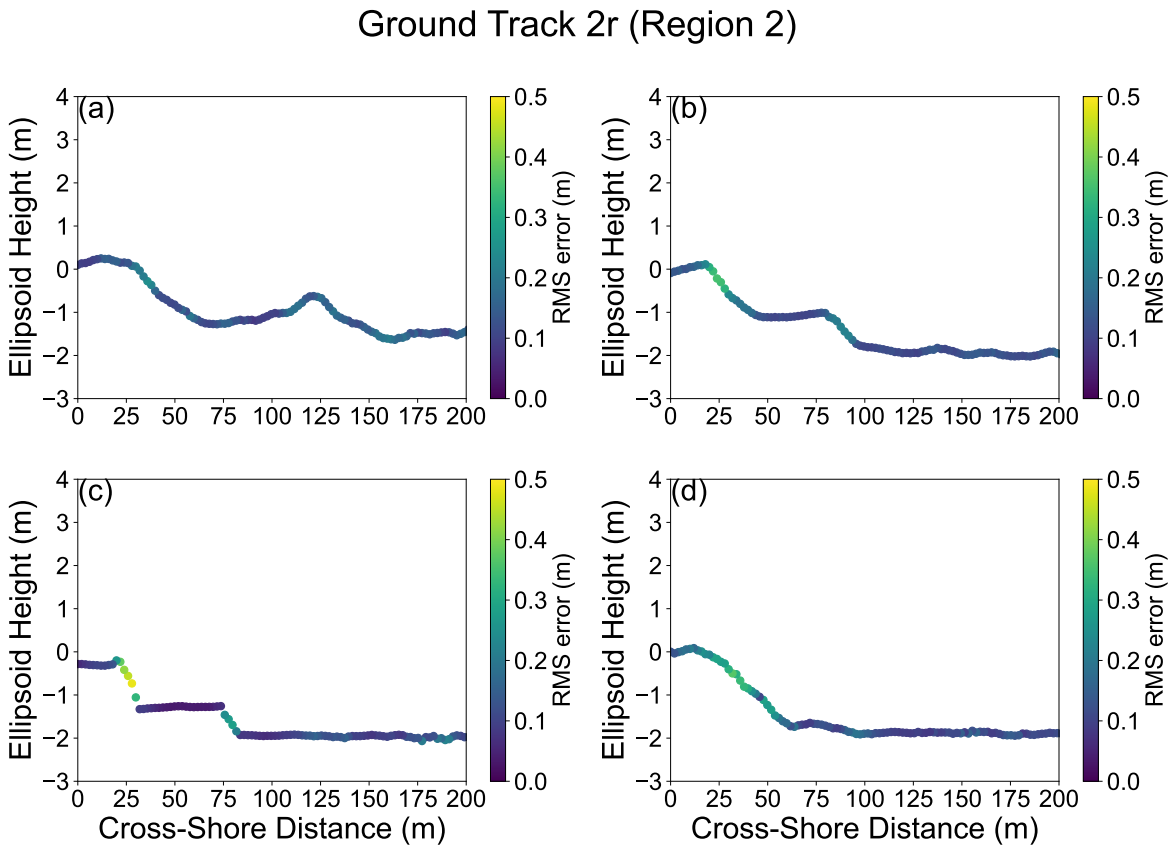


Figure 2.11: RMS error between our SlideRule-derived elevations and the source ATL03 photon information for ground track 2r for (a) 7 April 2019; (b) 4 January 2020; (c) 2 July 2021; (d) 31 December 2021

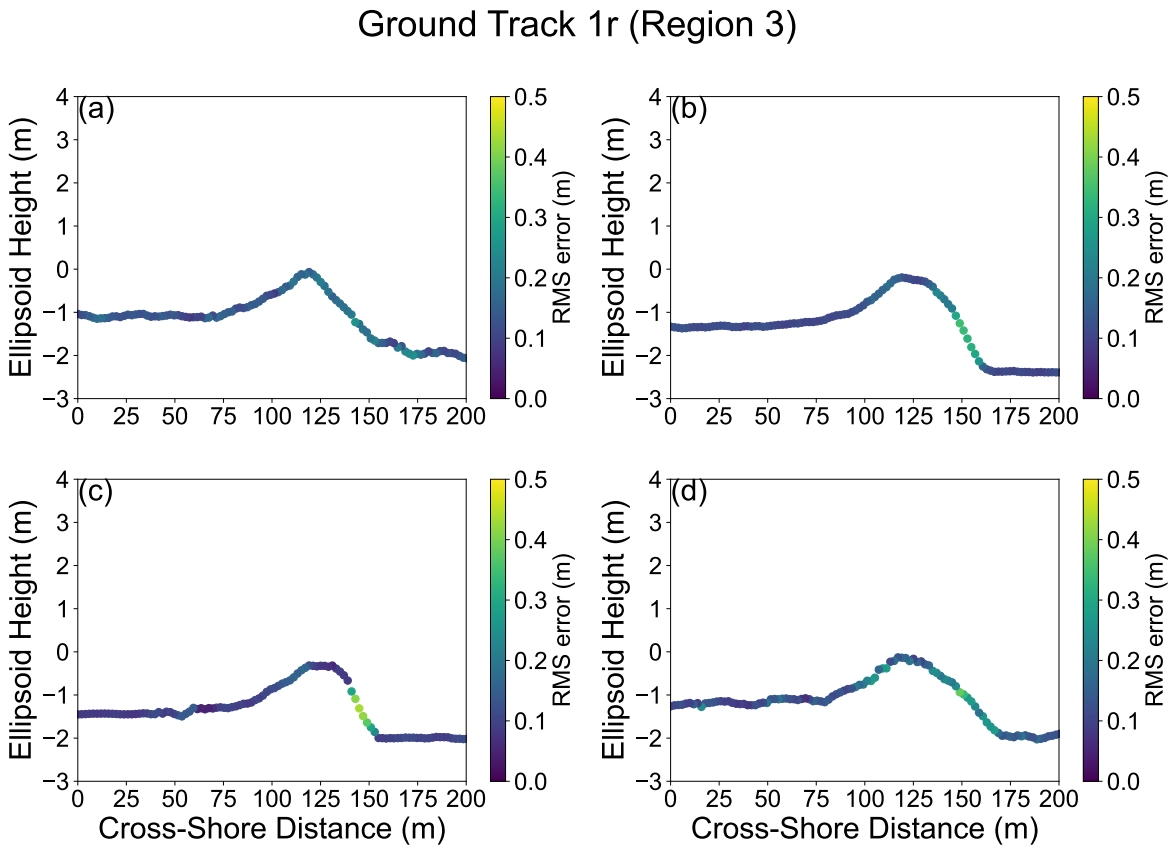


Figure 2.12: RMS error between our SlideRule-derived elevations and the source ATL03 photon information for ground track 1r for (a) 7 April 2019; (b) 4 January 2020; (c) 2 July 2021; (d) 31 December 2021

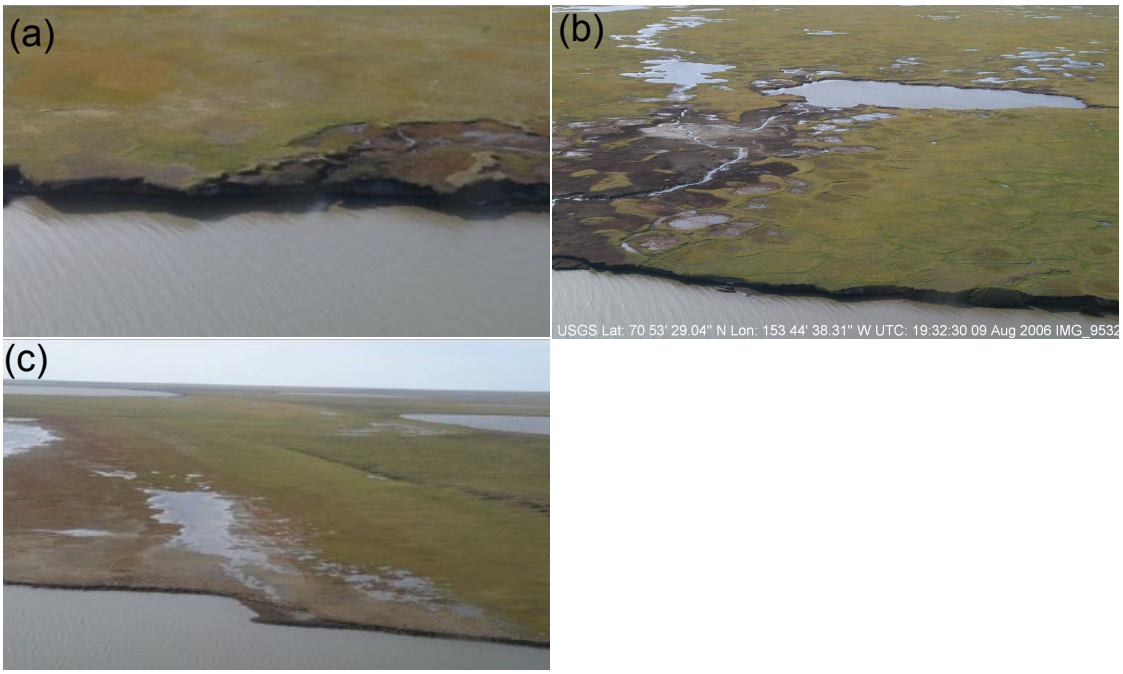


Figure 2.13: 2007 aerial photography from NOAA ShoreZone (Harper and Morris, 2014) captured near the sites our ICESat-2 ground tracks. a) A coastal bluff near the sampling site of ground track 3r in Region 1. b) The small lake sampled by ground track 2r in Region 2 before it drained. c) The western edge of the large breached thermokarst lake in Region 3 that is crossed by ground track 1r.

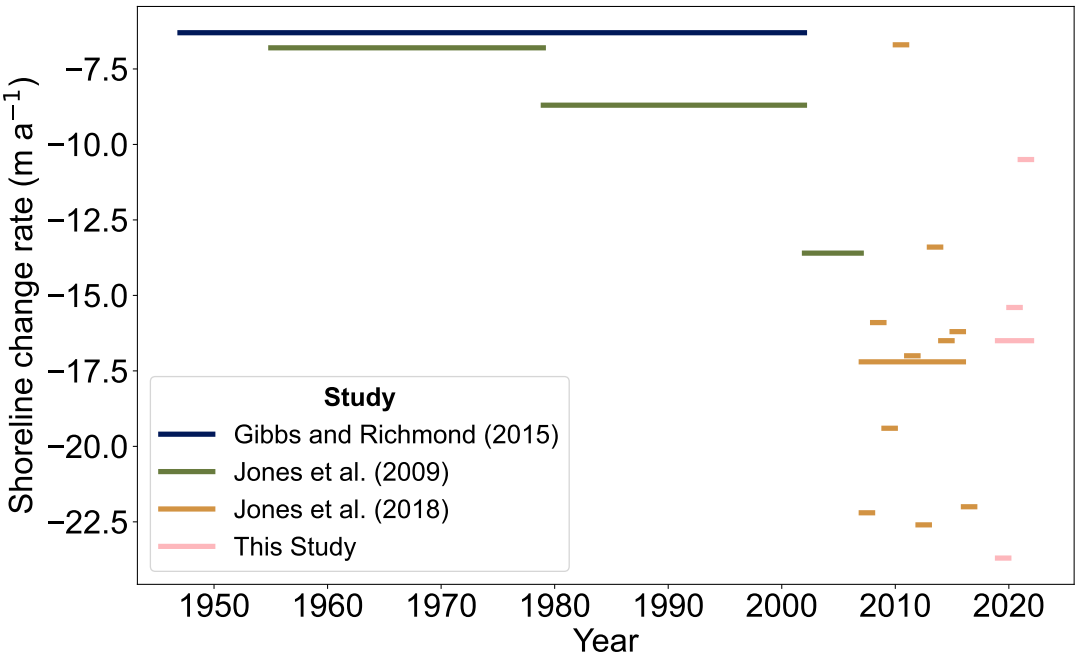


Figure 2.14: Long and short-term regional shoreline change rates along the Alaskan Beaufort Sea Coast near Drew point from previous work, along with the 3-year and year-to-year regional rates derived in this work

Table 2.5: The dates of all images used for the cluster uncertainty analysis described in Section 2.2, along with the standard deviation of the residuals derived from each cluster. The total number of images from each date is listed in parenthesis

Cluster	Dates	Standard deviation of residuals (m)
1	26 June 2020 (1), 27 June 2020 (1), 29 June 2020 (2)	1.8
2	04 July 2020 (1), 07 July 2020 (4), 07 10 2020 (1)	2.3
3	25 July 2020 (3)	2.8
4	16 June 2021 (2), 19 June 2021 (1)	1.9
5	02 July 2021 (1), 04 July 2021 (2),	2.4
6	13 July 2021 (1), 14 July 2021 (3)	1.9

Table 2.6: North-South change in the upper and lower boundaries estimated from ICESat-2 and the land-water boundaries estimated from Planet at each sampled ICESat-2 location

Track	Boundary	2019	2020	2021
Ground Track 3r (Region 1)	upper boundary	16.9 m (± 4.9 m)	-20.3m (± 5.9 m)	-6.6 m (± 4.9 m)
	lower boundary	28.4 m (± 4.9 m)	-18.4 m (± 5.9 m)	20.3 m (± 4.9 m)
	land-water boundary (Planet)	-13.7 m (± 3.1 m)	-12.2 m (± 3.1 m)	-3.6 m (± 3.1 m)
Ground Track 2r (Region 2)	upper boundary	-45.3 m (± 4.3 m)	-2.5 m (± 4.0 m)	-62.1 m (± 4.3 m)
	lower boundary	-67.2 m (± 4.3 m)	-12.5 m (± 4.0)	-20.3 (± 4.3 m)
	land-water boundary (Planet)	-36.9 m (± 3.1 m)	-10.8 m (± 3.1 m)	-27.0 m (± 3.1 m)
Ground Track 2r	upper boundary	10.2 m (± 5.6 m)	1.9 m (± 4.0 m)	1.7 m (± 5.6 m)
	lower boundary	-7.7 m (± 5.6 m)	-10.0 m (± 4.0 m)	15.6 m (± 5.6 m)
	land-water boundary (Planet)	13.8 m (± 3.1 m)	-1.6 m (± 3.1 m)	3.8 m (± 3.1 m)

References

Arndt, P. and Fricker, H. A. (2024). A framework for automated supraglacial lake detection and depth retrieval in icesat-2 photon data across the greenland and antarctic ice sheets [preprint]. *EGUsphere*, 2024:1–41.

Aré, F. E. (1988). Thermal abrasion of sea coasts (part I). *Polar Geography and Geology*, 12(1):1–1.

Baranskaya, A., Novikova, A., Shabanova, N., Belova, N., Maznev, S., Ogorodov, S., and Jones, B. M. (2021). The role of thermal denudation in erosion of ice-rich permafrost coasts in an enclosed bay (gulf of kruzenstern, western yamal, russia). *Frontiers in Earth Science*, 8.

Barnhart, K. R., Anderson, R. S., Overeem, I., Wobus, C., Clow, G. D., and Urban, F. E. (2014). Modeling erosion of ice-rich permafrost bluffs along the Alaskan Beaufort Sea coast. *Journal of Geophysical Research: Earth Surface*, 119(5):1155–1179.

Brunt, K. M., Smith, B. E., Sutterley, T. C., Kurtz, N. T., and Neumann, T. A. (2021). Comparisons of satellite and airborne altimetry with ground-based data from the interior of the Antarctic Ice Sheet. *Geophysical Research Letters*, 48(2).

Crameri, F. (2023). Scientific colour maps. Version 8.0.1. Zenodo, https://doi.org/10.5281/zenodo.8409685.

Crameri, F., Shephard, G. E., and Heron, P. J. (2020). The misuse of colour in science communication. *Nature Communications*, 11(1):5444.

Earlie, C., Masselink, G., and Russell, P. (2018). The role of beach morphology on coastal cliff erosion under extreme waves. *Earth Surface Processes and Landforms*, 43(6):1213–1228.

Farquharson, L., Mann, D., Swanson, D., Jones, B., Buzard, R., and Jordan, J. (2018). Temporal and spatial variability in coastline response to declining sea-ice in northwest Alaska. *Marine Geology*, 404:71–83.

Gibbs, A. and Richmond, B. (2015). National assessment of shoreline change—historical shoreline change along the north coast of alaska, u.s.–canadian border to icy cape. Open-File Report, U.S. Geological Survey.

Gibbs, A. E., Nolan, M., Richmond, B. M., Snyder, A. G., and Erikson, L. H. (2019). Assessing patterns of annual change to permafrost bluffs along the North Slope coast of Alaska using high-resolution imagery and elevation models. *Geomorphology*, 336:152–164.

Günther, F., Overduin, P. P., Yakshina, I. A., Opel, T., Baranskaya, A. V., and Grigoriev, M. N. (2015). Observing Muostakh disappear: permafrost thaw subsidence and erosion of a ground-ice-rich island in response to arctic summer warming and sea ice reduction. *The Cryosphere*,

9(1):151–178.

Harper, J. and Morris, M. (2014). Alaska ShoreZone coastal habitat mapping protocol. Technical report, Nuka Research and Planning Group, LLC.

Hersbach, H., Bell, B., Berrisford, P., Hirahara, S., Horányi, A., Muñoz-Sabater, J., Nicolas, J., Peubey, C., Radu, R., Schepers, D., Simmons, A., Soci, C., Abdalla, S., Abellan, X., Balsamo, G., Bechtold, P., Biavati, G., Bidlot, J., Bonavita, M., De Chiara, G., Dahlgren, P., Dee, D., Diamantakis, M., Dragani, R., Flemming, J., Forbes, R., Fuentes, M., Geer, A., Haimberger, L., Healy, S., Hogan, R. J., Hólm, E., Janisková, M., Keeley, S., Laloyaux, P., Lopez, P., Lupu, C., Radnoti, G., De Rosnay, P., Rozum, I., Vamborg, F., Villaume, S., and Thépaut, J. (2020). The ERA5 global reanalysis. *Quarterly Journal of the Royal Meteorological Society*, 146(730):1999–2049.

Himmelstoss, E., Henderson, R., Kratzmann, M., and Farris, A. (2021). Digital shoreline analysis system (DSAS) version 5.1 user guide: U.s. geological survey. Open-File Report, U.S. Geological Survey.

Hunter, J. D. (2007). Matplotlib: A 2D graphics environment. *Computing in Science & Engineering*, 9(3):90–95.

Irrgang, A. M., Lantuit, H., Manson, G. K., Günther, F., Grosse, G., and Overduin, P. P. (2018). Variability in rates of coastal change along the yukon coast, 1951 to 2015. *Journal of Geophysical Research: Earth Surface*, 123(4):779–800.

Jasinski, M. F., Stoll, J. D., Hancock, D., Robbins, J., Nattala, J., Pavelsky, T. M., Morison, J., Jones, B. M., Ondrusek, M. E., Parrish, C., Carabajal, C., and the ICESat-2 Science Team. (2023). Atlas/icesat-2 l3A along track inland surface water data, version 6.

Jones, B. M., Arp, C. D., Jorgenson, M. T., Hinkel, K. M., Schmutz, J. A., and Flint, P. L. (2009). Increase in the rate and uniformity of coastline erosion in Arctic Alaska. *Geophysical Research Letters*, 36(3):2008GL036205.

Jones, B. M., Farquharson, L. M., Baughman, C. A., Buzard, R. M., Arp, C. D., Grosse, G., Bull, D. L., Günther, F., Nitze, I., Urban, F., Kasper, J. L., Frederick, J. M., Thomas, M., Jones, C., Mota, A., Dallimore, S., Tweedie, C., Maio, C., Mann, D. H., Richmond, B., Gibbs, A., Xiao, M., Sachs, T., Iwahana, G., Kanevskiy, M., and Romanovsky, V. E. (2018). A decade of remotely sensed observations highlight complex processes linked to coastal permafrost bluff erosion in the Arctic. *Environmental Research Letters*, 13(11):115001.

Jorgenson, M. T., Kanevskiy, M., Shur, Y., Grunblatt, J., Ping, C.-L., and Michaelson, G. (2014). Permafrost database development, characterization, and mapping for northern alaska. Technical report, U.S. Fish and Wildlife Service.

Lantuit, H., Overduin, P. P., Couture, N., Wetterich, S., Aré, F., Atkinson, D., Brown, J., Cherkashov,

G., Drozdov, D., Forbes, D. L., Graves-Gaylord, A., Grigoriev, M., Hubberten, H.-W., Jordan, J., Jorgenson, T., Ødegård, R. S., Ogorodov, S., Pollard, W. H., Rachold, V., Sedenko, S., Solomon, S., Steenhuisen, F., Streletskaya, I., and Vasiliev, A. (2012). The Arctic Coastal Dynamics Database: A new classification scheme and statistics on arctic permafrost coastlines. *Estuaries and Coasts*, 35(2):383–400.

Liu, C., Li, J., Tang, Q., Qi, J., and Zhou, X. (2022). Classifying the Nunivak Island Coastline Using the Random Forest Integration of the Sentinel-2 and ICESat-2 Data. *Land*, 11(2):240.

Lu, X., Hu, Y., Yang, Y., Vaughan, M., Palm, S., Trepte, C., Omar, A., Lucker, P., and Baize, R. (2021). Enabling value added scientific applications of ICESat-2 data with effective removal of afterpulses. *Earth and Space Science*, 8(6).

Luthcke, S. B., Thomas, T. C., Pennington, T. A., Rebold, T. W., Nicholas, J. B., Rowlands, D. D., Gardner, A. S., and Bae, S. (2021). ICESat-2 pointing calibration and geolocation performance. *Earth and Space Science*, 8(3):e2020EA001494.

Magruder, L., Brunt, K., Neumann, T., Klotz, B., and Alonzo, M. (2021). Passive ground-based optical techniques for monitoring the on-orbit ICESat-2 altimeter geolocation and footprint diameter. *Earth and Space Science*, 8(10).

Markus, T., Neumann, T., Martino, A., Abdalati, W., Brunt, K., Csatho, B., Farrell, S., Fricker, H., Gardner, A., Harding, D., Jasinski, M., Kwok, R., Magruder, L., Lubin, D., Luthcke, S., Morison, J., Nelson, R., Neuenschwander, A., Palm, S., Popescu, S., Shum, C., Schutz, B. E., Smith, B., Yang, Y., and Zwally, J. (2017). The Ice, Cloud, and land Elevation Satellite-2 (ICESat-2): Science requirements, concept, and implementation. *Remote Sensing of Environment*, 190:260–273.

Michaelides, R. J., Bryant, M. B., Siegfried, M. R., and Borsa, A. A. (2021). Quantifying surface-height change over a periglacial environment with ICESat-2 laser altimetry. *Earth and Space Science*, 8(8).

Neuenschwander, A. L., Pitts, K. L., Jelley, B. P., Robbins, J., Markel, J., Popescu, S. C., Nelson, R. F., Harding, D., Pederson, D., Klotz, B., and Sheridan., R. (2023). Atlas/icesat-2 l3a land and vegetation height, version 6.

Neumann, T. A., Brenner, A., Hancock, D., Robbins, J., Gibbons, A., Lee, J., Harbeck, K. and. Saba, J., Luthcke, S. B., and Rebold, T. (2023). Atlas/icesat-2 l2a global geolocated photon data, version 6.

Neumann, T. A., Martino, A. J., Markus, T., Bae, S., Bock, M. R., Brenner, A. C., Brunt, K. M., Cavanaugh, J., Fernandes, S. T., Hancock, D. W., Harbeck, K., Lee, J., Kurtz, N. T., Luers, P. J., Luthcke, S. B., Magruder, L., Pennington, T. A., Ramos-Izquierdo, L., Rebold, T., Skoog, J., and Thomas, T. C. (2019). The Ice, Cloud, and Land Elevation Satellite – 2 mission: A global geolocated photon product derived from the Advanced Topographic Laser Altimeter System.

Remote Sensing of Environment, 233.

Otsu, N. (1979). A threshold selection method from gray-level histograms. *IEEE Transactions on Systems, Man, and Cybernetics*, 9(1):62–66.

Overeem, I., Anderson, R. S., Wobus, C. W., Clow, G. D., Urban, F. E., and Matell, N. (2011). Sea ice loss enhances wave action at the Arctic coast: Sea ice loss enhances erosion. *Geophysical Research Letters*, 38(17):n/a–n/a.

Planet Team (2023). Planet application program interface: In space for life on earth. https://api.planet.com.

Sadler, P. M. and Jerolmack, D. J. (2015). Scaling laws for aggradation, denudation and progradation rates: the case for time-scale invariance at sediment sources and sinks. *Geological Society, London, Special Publications*, 404(1):69–88.

Shean, D., Swinski, J. P., Smith, B., Sutterley, T., Henderson, S., Ugarte, C., Lidwa, E., and Neumann, T. (2023). SlideRule: Enabling rapid, scalable, open science for the NASA ICESat-2 mission and beyond. *Journal of Open Source Software*, 8(81):4982.

Smith, B., Adusumilli, S., Csathó, B. M., Felikson, D., Fricker, H. A., Gardner, A., Holschuh, N., Lee, J., Nilsson, J., Paolo, F. S., Siegfried, M. R., Sutterley, T., and the ICESat-2 Science Team. (2023). Atlas/icesat-2 l3a land ice height, version 6. https://nsidc.org/data/ATL06/versions/6.

Smith, B., Fricker, H. A., Holschuh, N., Gardner, A. S., Adusumilli, S., Brunt, K. M., Csatho, B., Harbeck, K., Huth, A., Neumann, T., Nilsson, J., and Siegfried, M. R. (2019). Land ice height-retrieval algorithm for NASA's ICESat-2 photon-counting laser altimeter. *Remote Sensing of Environment*, 233:111352.

Van Rijn, L. (2011). Coastal erosion and control. *Ocean & Coastal Management*, 54(12):867–887.

Vos, K. (2024). Sds_transects.py. https://github.com/kvos/CoastSat/blob/master/coastsat/SDS_transects.py.

Vos, K., Splinter, K. D., Harley, M. D., Simmons, J. A., and Turner, I. L. (2019). CoastSat: A Google Earth Engine-enabled Python toolkit to extract shorelines from publicly available satellite imagery. *Environmental Modelling & Software*, 122:104528.

Wang, J., Li, D., Cao, W., Lou, X., Shi, A., and Zhang, H. (2022). Remote sensing analysis of erosion in Arctic coastal areas of Alaska and eastern Siberia. *Remote Sensing*, 14(3):589.

Wobus, C., Anderson, R., Overeem, I., Matell, N., Clow, G., and Urban, F. (2011). Thermal erosion of a permafrost coastline: Improving process-based models using time-lapse photography. *Arctic, Antarctic, and Alpine Research*, 43(3):474–484.

Xie, H., Sun, Y., Liu, X., Xu, Q., Guo, Y., Liu, S., Xu, X., Liu, S., and Tong, X. (2021). Shore zone classification from ICESat-2 data over Saint Lawrence Island. *Marine Geodesy*, 44(5):454–466.

Chapter 3

Unsupervised classification of topographic shores type from airborne lidar in the East Chukchi Sea

Abstract

Understanding the importance of morphology on shoreline change rates in the Arctic requires high-resolution, up-to-date information on shoreline morphology. Existing large-scale databases are time-invariant and would be difficult to reproduce, while site-specific classification efforts are primarily qualitative and not always generalizable. Here, we propose an unsupervised clustering approach to provide a reproducible, quantitative classification scheme based on cross-shore profiles from airborne lidar. Our approach represents profiles as normalized forms that are scaled by their total width and height. We perform k-means clustering in two steps:

1. We cluster the normalized forms using elastic functional k-means to create form clusters.
2. We then subdivide these form clusters into parameter clusters by performing k-means clustering on their respective widths and heights.

We test this approach on a 72-km stretch of the East Chukchi Sea coast between Utqiagvik and Peard Bay. We divide our profiles into two form clusters: cliff-like profiles and profiles that slope downwards behind the backshore due to hydrologic features. Our parameter clustering subdivides the cliff-like profiles into low-intermediate cliffs, wide cliffs, and tall cliffs, and the

downwards-sloping profiles into river mouths, drainage channel mouths, low-intermediate cliffs with drainage channels, and tall cliffs with drainage channels. We find that cliff clusters make up larger along-shore units than downwards-sloping clusters, and that parameter clusters are unevenly distributed along the shoreline, with wide clusters occurring primarily in the north and tall clusters occurring primarily in the south. This classification scheme captures the primary landforms present in the region, but does not account for less common features such as slumped tundra and man-made features. We note that clustering parameters and the final number of clusters are subjective and should be chosen based on comparison against available imagery and specific research needs. We conclude that k-means clustering can produce groupings that are physically meaningful, and provide a basic framework that can be adapted for different research purposes.

3.1 Introduction

To generalize our findings of shore-type dependent retreat from Chapter 2, we need continuous alongshore high-resolution classifications of shore morphology. However, these are not currently available on a large scale. Previous work considering the link between morphology and retreat rates use shoreline morphology classifications from a variety of sources. The Arctic Coastal Dynamics Database (Lantuit et al., 2012) provides a low-resolution (10s of km), circum-Arctic database of shore forms, composition and retreat rates based on a compilation of field data and expert analysis, and has been used to assess large-scale drivers of retreat (Irrgang et al., 2022; Lantuit et al., 2012; Nielsen et al., 2022). The ShoreZone database (Harper and Morris, 2014) provides coastal classifications at higher resolutions (10s of meters to 100s of meters) in Alaska and British Columbia based on expert analysis of aerial photography, and has been used to examine local variability in retreat rates on the Chukchi Sea Coast (Farquharson et al., 2018) and Alaskan Beaufort Sea Coast (Bryant et al., 2025). Regional studies of shoreline change have relied on locally available datasets including general tundra landform classifications (Joregenson et al., 2015; Lara et al., 2018; Piliouras et al., 2023) and interpretation of satellite and aerial imagery (Irrgang et al., 2018) to derive their own site-specific classifications.

The existing Arctic coastal classification schemes have some fundamental limitations on available Arctic coastal classifications. Given high retreat rates in the Arctic (0.5 m/yr on average (Lantuit et al., 2012),with up to 22 m/y locally in Northern Alaska (Jones et al., 2018)) and observations of rapid change in local shoreline morphology (Bryant et al., 2025; Jones et al., 2013; Lim et al., 2020), these snapshot databases may not be an adequate reference for studies that require up-to-date local shoreline conditions. Studies focused on the drivers of local shoreline rates may also benefit from classifications at higher resolutions than what is currently available. Furthermore, existing classifications have data gaps. ShoreZone only covers Alaska and British Columbia, while the Arctic Coastal Dynamics database excludes much of the Canadian Archipelago, Greenland, and the Bering Sea. The reliance of these databases on expert analysis of field data make them difficult to reproduce. While individual studies have performed their own site-specific classifications, their methods and classes may not be generalizable to other areas.

A quantitative classification scheme based on remotely sensed datasets could provide a reproducible way to generate custom classes over specific areas and time intervals of interest. Recent work has explored classifying the shoreline using airborne and spaceborne elevation datasets. Airborne elevation surveys provide high-resolution along- and across-shore measurements of the shore zone over large areas. Nijland et al. (2017) trained a random forest model to predict ShoreZone coastal types from airborne lidar. Xie et al. (2021) applied a similar method to space-borne datasets by training a similar classification model on elevation data from ICESat-2, and Liu et al. (2022) expanded on this work by combining metrics from ICESat-2 elevation data and Sentinel-2 elevation data. While these methods show the potential to identify shore types using elevation data, supervised classification methods rely on having an existing classification dataset to train on, and are limited by the resolution of the training dataset. Unsupervised classification removes the need for pre-existing datasets, providing more flexibility in where they can be applied.

Here, we present a reproducible, quantitative framework for classifying shorelines based on unsupervised clustering of cross-shore elevation profiles and demonstrate its utility along the Eastern Chukchi Sea Coast. The classification is broken into two parts: identifying underlying

functional forms that describe the general shape of the profiles, and then subdividing these forms into sub-clusters based on their overall widths and heights. We utilize aerial photographs and satellite imagery to inform an appropriate number of clusters and provide physical interpretations of our clusters. We discuss the successes and limitations of our classification method, and how it could be adapted to different use cases.

3.2 Data and Methods

3.2.1 Study area

This study is focused on a 72 km length of coastline along the Eastern Chukchi Sea, starting at the southern edge of Utqiagvik and ending west of Peard Bay (Figure 3.1). This exposed stretch of coastline is broadly characterized as consisting of coastal bluffs with narrow (40 m or less) sand and gravel beaches. These bluff are punctuated by small creeks, bays, and drainage outlets, which often are fronted by wide (up to 150 m) sandy beaches or spits (Gibbs and Richmond, 2015). The average shoreline change rate across this region between 1947 and 2010 is -0.3 m/yr, with local change rates ranging from -1.2 m/yr to 0.7 m/yr (Gibbs et al., 2024). Based on these rates, we assume that shoreline morphology is stable on annual to decadal timescales.

3.2.2 Elevation transect generation and processing

Elevation transects for our classification scheme were derived from a 2010 airborne lidar survey from USGS (OCM Partners, 2026). The point cloud has a nominal point spacing of 1.5 m (corresponding to a point density of .67 point/m^2), and vertical accuracy better than 30 cm. A digital elevation model (DEM) was generated from the point cloud data by estimating the average elevation across 2m grid cells using the NOAA Digital Coast Data Access Viewer (NOAA, 2025), which provides on-demand processing of lidar data.

To generate cross-shore transects, we first generated a shore-parallel reference shoreline at the seaward-most 0-m contour of the DEM using the Contour tool in QGIS. To reduce small-scale undulations and ensure similar spacing between transects, we smoothed the shoreline with

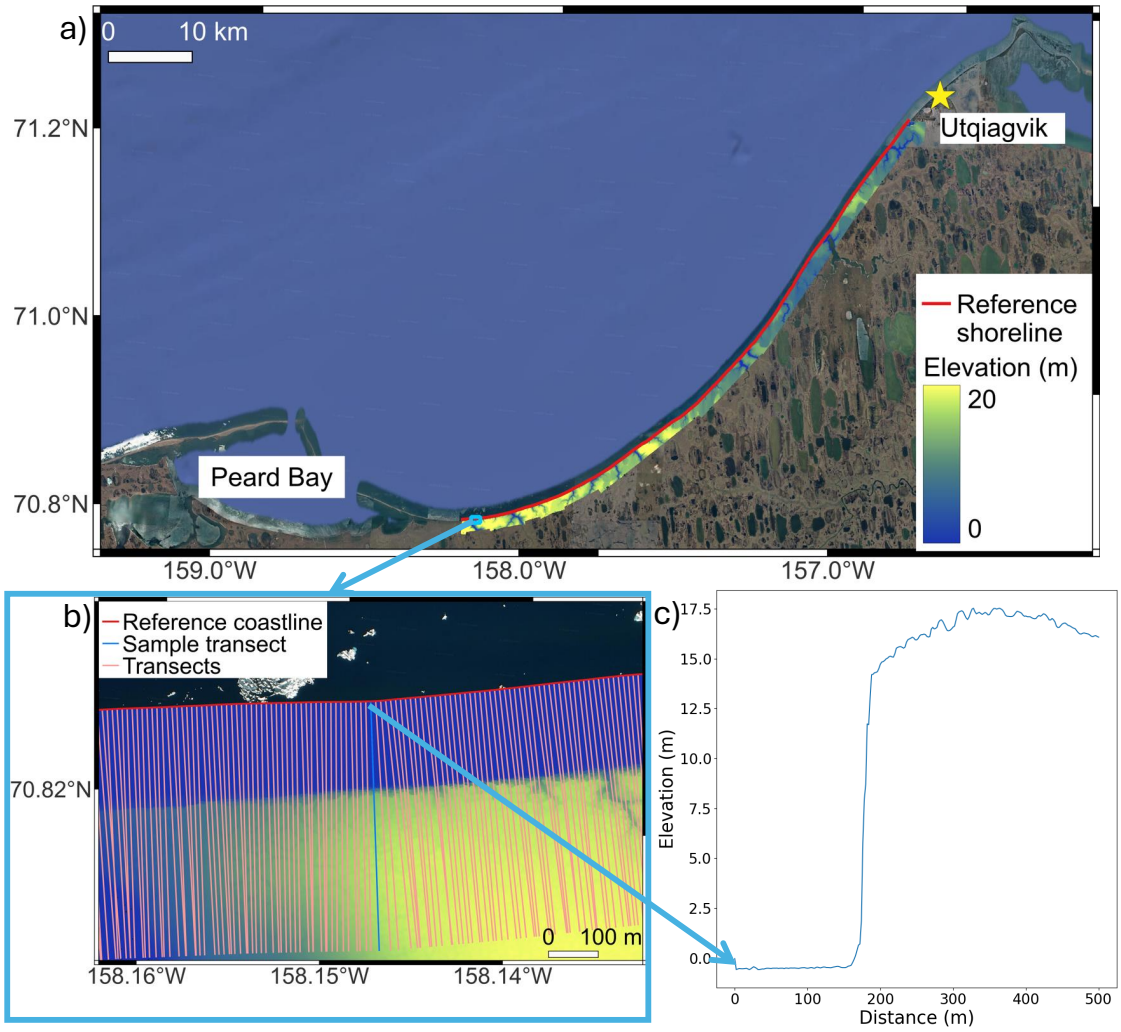


Figure 3.1: a) An overview of the study area and elevation data on the northwestern coast of Alaska. An offshore reference coastline derived from the DEM is shown. b) 500m shore-perpendicular transects are cast from the reference shoreline and ending inland. c) The resulting elevation profile from sampling the DEM along the transect labeled in b)

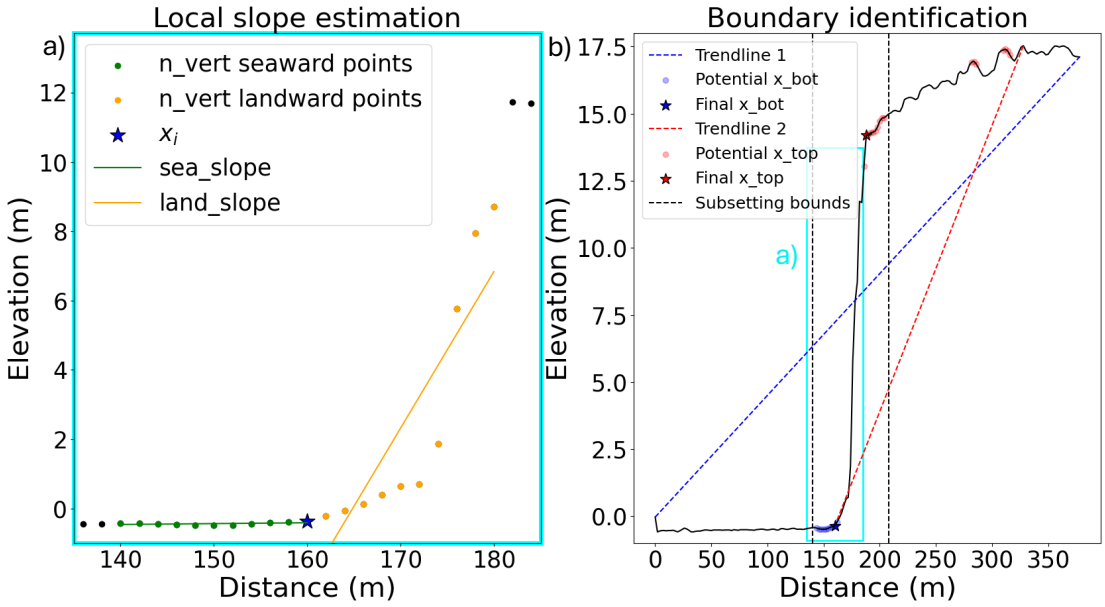


Figure 3.2: a) An example of how the local *sea_slope* and *land_slope* variables are calculated for a given point x_i of the profile in panel b), using the final *x_bot* as an example. *Sea_slope* is estimated through a linear interpolation of *n_vert* points seawards of x_i , while *land_slope* is estimated through a linear interpolation of *n_vert* points landwards of x_i: . b)The selection of *x_bot*, *x_top*, and the subsetting bounds using CliffDelineaTool. Potential *x_bot* and *x_top* tops points are identified based on their local *land_slope* and *sea_slope*. The final *x_bot* is selected as the potential *x_bot* that is farthest from Trendline 1, and the final *x_top* is selected as the potential *x_top* that is farthest from Trendline 2. The subsetting bounds are defined as 20 meters seaward of *x_bot* and 20m landward of *x_top*.

a 50-m running mean. We then used the SDS-transect module from CoastSat (Vos et al., 2019) to create shore-perpendicular transects every 10m along-shore starting at this reference coastline and extending 500 m landwards. The DEM was sampled every 2m along each transect to create cross-shore elevation profiles. This resulted in 7411 elevation profiles.

We next delineated the shore zone in each transect. While the shore zone is often delineated using tidal data or visual indicators such as vegetation (Nijland et al., 2017), here we use a topography-based definition that relies only on elevation data. Let x refer to the horizontal position along the profile and $h(x)$ refer to the elevation. For each profile, we identified the apparent instantaneous water line (x_{bot}) and the backshore-onshore boundary (x_{top}, illustrated in Figure 3.2) using a modified version of CliffDelineaTool (Swirad, 2021; Swirad and Young, 2022), a Python tool designed to automatically identify the bottoms and tops of cliffs from elevation profiles using a distance-to-trendline approach, which we describe below and illustrate in Figure 3.2. All user-specified parameters are given in italics and defined in Table 3.1.

The original profiles are truncated $land_lim$ points from the absolute elevation maximum, if there is one before the end of the profile. For every point x_i along the truncated profile, CliffDelineaTool calculates local seaward and landwards slopes (sea_slope and $land_slope$ respectively) from the neighboring points that are n_vert points seawards and n_vert points landwards of x_i respectively, as shown in figure 3.2 a). While the original algorithm calculates sea_slope and $land_slope$ by calculating the pairwise slopes between each adjacent point and then taking the average, we instead calculated the slope using a linear interpolation of all the points within n_vert of x_i in order to increase computational efficiency. We added an additional step, to flag areas where the elevation drops inland of the backshore due to inland water or cross-cutting drainage channels. If the local $land_slope$ exceeds the user-specified neg_slope parameter, the profile is truncated $land_lim$ points inland of the first point where neg_slope occurs. A trendline (Trendline 1 in figure 3.2 b) is drawn from the first to the last point on the profile. Potential base points are defined as points that fall below Trendline 1, have a sea_slope value below a specified threshold $baseSea$, have a $land_slope$ value above a threshold $baseLand$, and have an elevation below $MaxBaseElev$. The potential base

point that has the highest vertical distance from the trend line is selected as the final base x_{bot}. While CliffDelineaTool was designed to identify the cliff-beach junction, by starting the transects seawards of the beach we instead capture the apparent instantaneous waterline.

Once the base has been identified, a second trendline (Trendline 2) is drawn from *x_bot* to the end of the profile. Potential tops are defined as points that fall above Trendline 2, have a *sea_slope* greater than $topSea$, and have a *land_slope* lower than $topLand$. Due to the large size of our study area (72 km), it was challenging to find a single combination of $topSea$ and $topLand$ that was suitable for all profiles. In some cases, the transition from the backshore to onshore is abrupt and *sea_slope* is steep while *land_slope* is shallow. In other cases, the transition is more gradual, such that *sea_slope* is low and *land_slope* is steep relative to the abrupt transition case. To address this, we added an additional constraint: potential tops must satisfy the condition that $\frac{sea_slope}{land_slope} > \alpha$. This makes it easier to identify tops with a shallow *sea_slope* or steep *land_slope* while ensuring relative slope shallowing around the top. The potential top that has the highest vertical distance from Trendline 2 is selected as the final backshore-onshore boundary x_{top}. A full list of the parameters used is provided in table 3.1. While CliffDelineaTool includes a third step to search for an alternative top landwards of x_top, we do not implement this step. We also do not implement the smoothing and outlier detection step at this stage.

Out of our 7411 total transects, 15 transects were dropped because the algorithm failed to find a top or a base. Each profile was then trimmed to start 20 m seawards of x_{bot} and end 20 m inland of x_{top} (see figure 3.2 b for an example of the resulting subsetting bounds). Including these seaward and landward buffers in the subsetting bounds helps to ensure that all relevant nearshore data is included, including the immediate onshore region.

We derived two along-shore statistics from our profiles: the width (W) and the height (H). The width is defined here as the horizontal distance between x_{bot} and x_{top}:

$$W = x_{top} - x_{bot} \tag{3.1}$$

Table 3.1: Parameters used for our modified CliffDelineaTool algorithm

Parameter	Explanation	Value
nVert	The number of adjacent points used to calculate local slopes	10
land_lim	The number of points inland of the local maximum or negative slope threshold to use	25
baseMaxElev	The maximum allowed base elevation (m)	.5
baseSea	The maximum seaward slope (sea_slope) allowed for potential bases (degrees)	.5
baseLand	The minimum landward slope (land_slope) allowed for potential bases (degrees)	.5
topSea	The minimum seaward slope allowed for potential tops (degrees)	2
topLand	The maximum landward slope allowed for potential tops (degrees)	5
α	The minimum ratio of sea_slope to land_slope allowed for potential bases	3
neg_slope	The threshold for truncating a transect that slopes downwards (degrees)	-1

The total height H is defined as the vertical distance between the elevation of the highest point and the elevation at the lowest point on the profile:

$$H = max(h) - min(h) \tag{3.2}$$

Along-shore outliers may be present from misidentifications of x_{top} or x_{bot} due to blunders in CliffDelineaTool or small-scale features such as river channels that are not well-captured in our sampling. We identified outliers in W and H by creating smoothed versions of each parameter, $\bar{W}$ and $\bar{H}$ using a 50 m (5 transect) along-shore running mean (figure 3.3). We then calculated standardized residuals between the original and smoothed datasets:

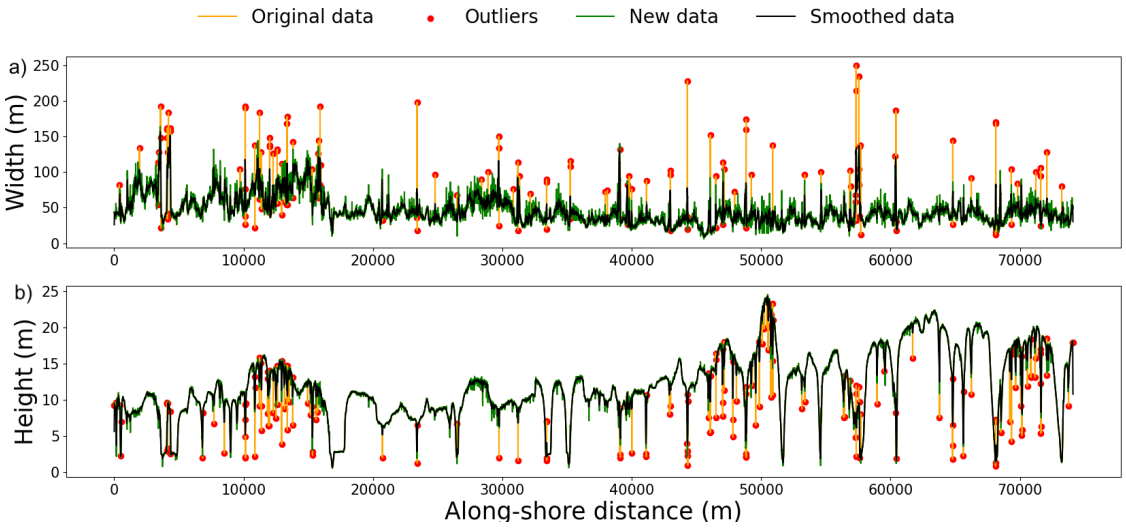


Figure 3.3: Our estimated W (a)) and H (b) parameters were smoothed alongshore, and outliers were removed.

$$r_W = W - \bar{W} \tag{3.3}$$

$$\hat{r}_W = \frac{r_W}{\sigma_{r_W}} \tag{3.4}$$

$$r_H = H - \bar{H} \tag{3.5}$$

$$\hat{r}_H = \frac{r_H}{\sigma_{r_H}} \tag{3.6}$$

Where σ_r is the standard deviation of the residual. Any transect where $\hat{r_W}$ or $\hat{r_H}$ was greater than 3 was flagged as an outlier (figure 3.3) and excluded. After outlier removal, we were left with 7150 transects.

3.2.3 Clustering

Our clustering workflow separates the profiles into two components (figure 3.4): normalized functions $\hat{h}(\hat{x})$ which describe the general shape of the profiles, and scaling parameters (W,H) that describe their dimensions. We first clustered profiles based on their normalized functions to create *form clusters*, then subdivided each from cluster into more detailed *parameter clusters* based on the associated scaling parameters.

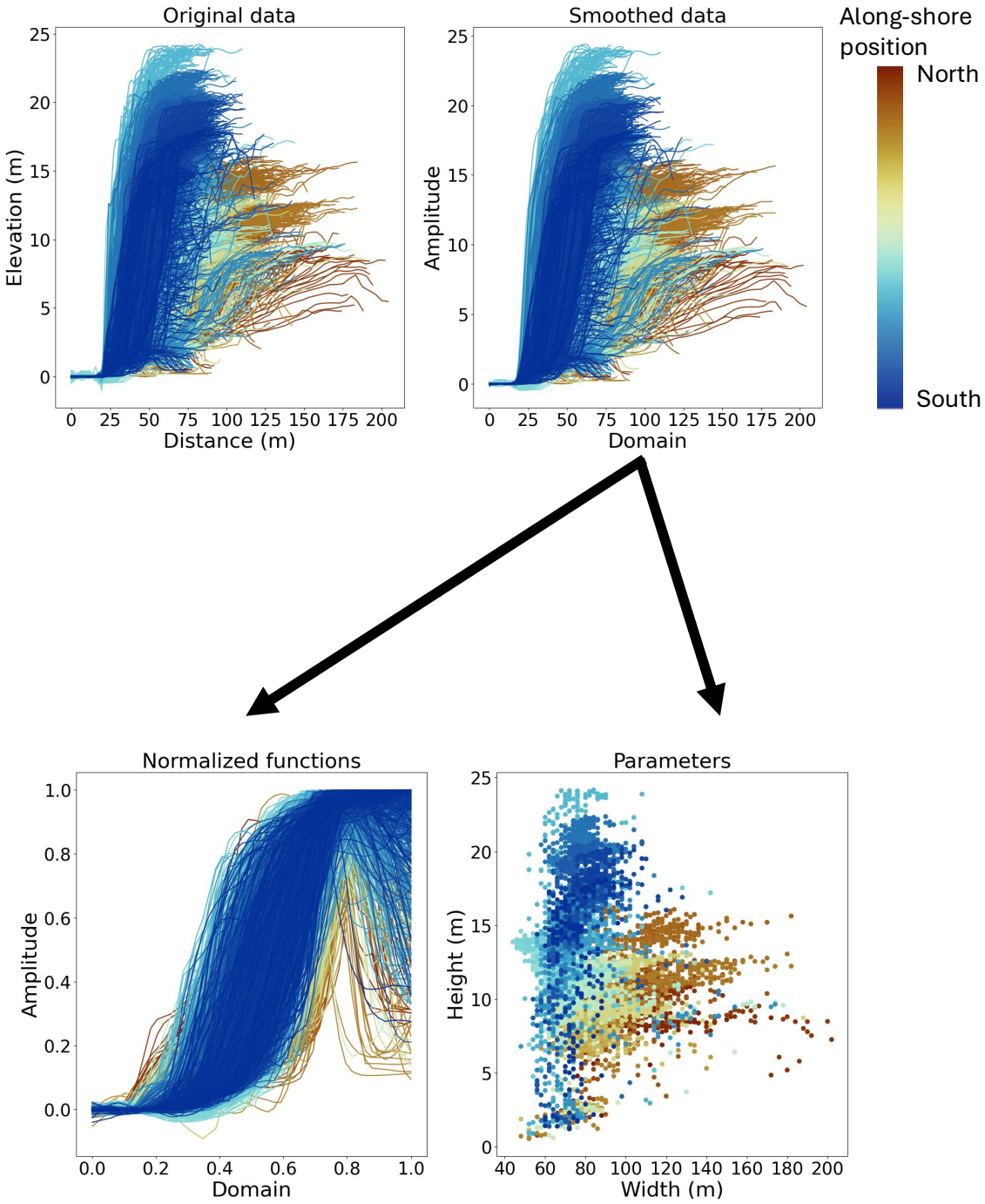


Figure 3.4: Profiles were smoothed and then decomposed into two components: normalized functions and scaling parameters

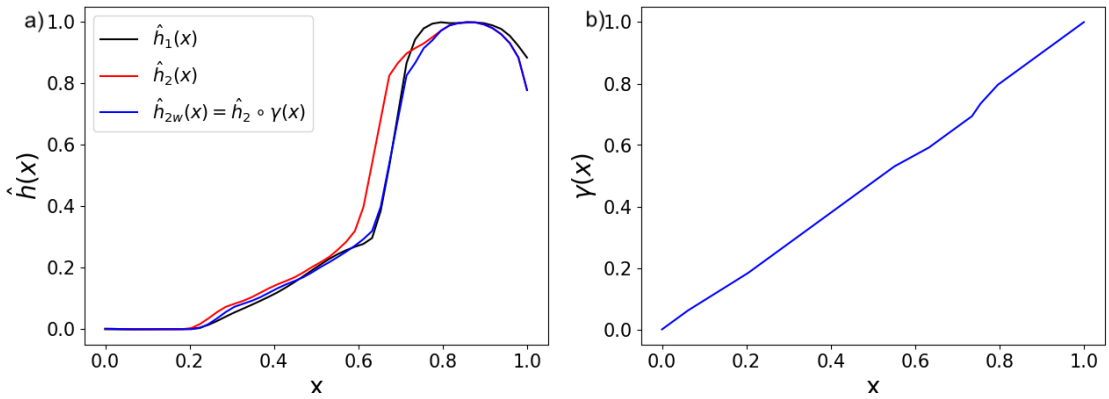


Figure 3.5: An example of functional alignment. a: $\hat{h}_2$ is aligned to $\hat{h}_1$ by warping its domain using the warping function $\gamma(x)$ (b)

To create the normalized functions, each profile was normalized by its total height and total width, and the elevation was referenced to its apparent local sea level:

$$\hat{x} = \frac{x}{W + x_{sea} + x_{land}} \tag{3.7}$$

$$\hat{h}(\hat{x}) = \frac{h(x) - \bar{h_w}}{H} \tag{3.8}$$

Where $x_{sea} = x_{land} = 20$m refers to the distance before x_{bot} and after x_{top} after subsetting, and $\bar{h_w}$ refers to the median value of h between 0 and x_{sea}. To ensure that every $\hat{h}(x)$ has the same domain, each normalized transect was resampled to 50 points evenly spaced horizontally (every .02 units across the domain) using a piecewise linear interpolation.

Functional clustering

The first step of our clustering is functional clustering, where we identify groups of normalized profiles that share a similar shape. We clustered the profiles using elastic functional k-means alignment, implemented using the FDASRSF python package (Tucker, 2024; Tucker et al., 2013; Zang et al., 2020). Functional alignment aims to reduce the difference between two functions that have a similar shape, but have horizontal offsets due to a shift or distortion between their domains (see figure 3.5 for an example). Given two profiles, $\hat{h}_1$ and $\hat{h}_2$, we seek to find the optimal domain

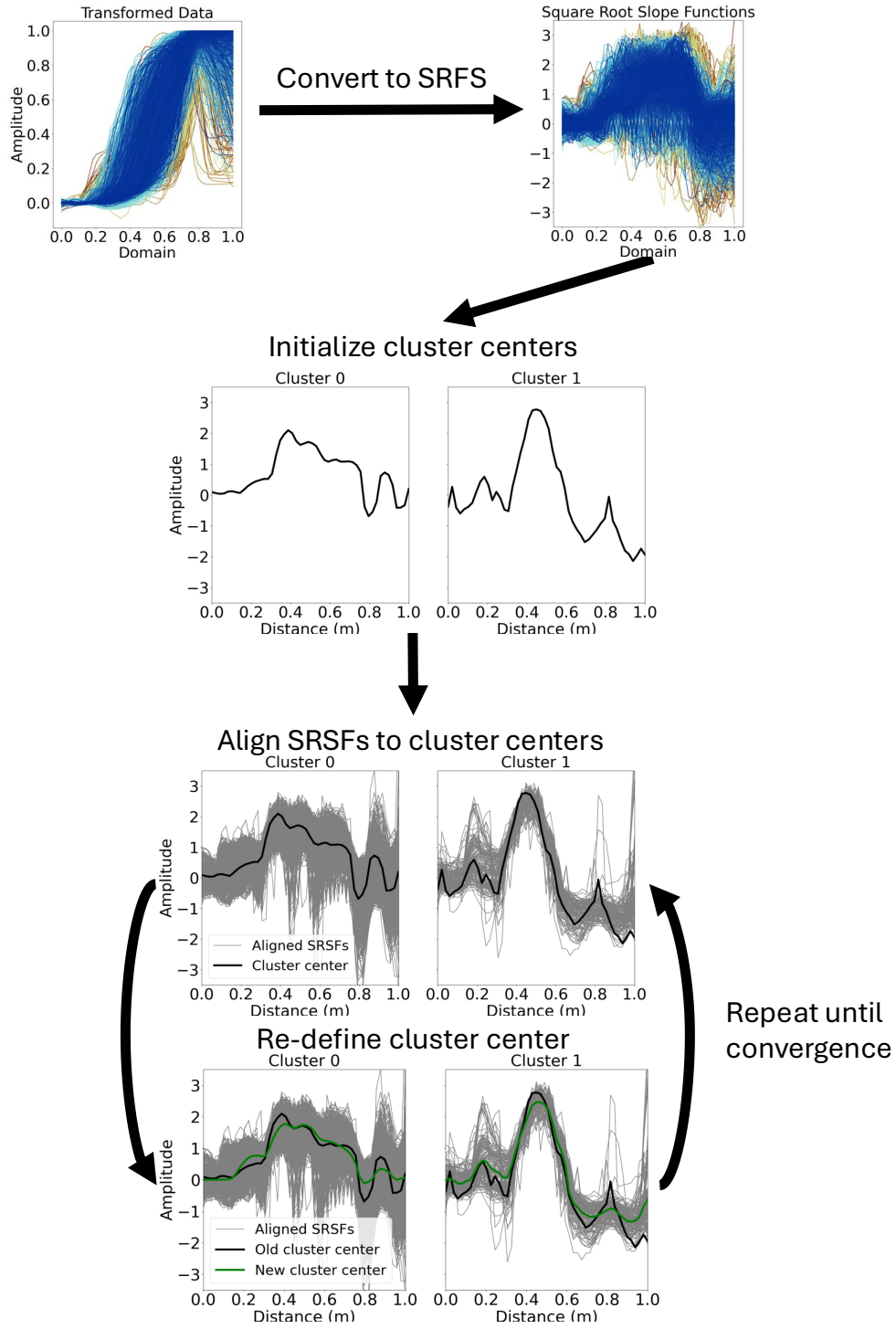


Figure 3.6: The FDASRSF workflow.

warping function γ such that the difference between $\hat{h}_1(x)$ and $\hat{h}_{2w} = \hat{h}_2 \circ \gamma(x)$:

$$d_{1,2} = \sqrt{\int_0^1 |\hat{h}_2 \circ (\gamma(x)) - \hat{h}_1(x)|^2 dx + \lambda |1 - \gamma'(x)|^2} \tag{3.9}$$

is minimized. λ is a penalty constant that constrains the degree to which a function can be warped - as lambda increases, the difference between x and $\gamma(x)$ decreases (Wu and Srivastava, 2011).

The distance equation 3.9 is not symmetric, meaning that the optimal γ and resulting value of d will vary depending on whether $\hat{h}_1$ is aligned to $\hat{h}_2$ or $\hat{h}_2$ is aligned to $\hat{h}_1$. To address this asymmetry, Tucker et al. (2013) and Zang et al. (2020) instead consider the square root slope function (SRSF or q) of each profile:

$$q(x) = \frac{\hat{h}'(x)}{\sqrt{|\hat{h}'(x)|}} \tag{3.10}$$

It can be shown that if a function $\hat{h}$ is warped into $\hat{h}_w$, the SRSF of the warped function q_w is:

$$q_w = q \circ \gamma(x) \sqrt{\gamma'} \tag{3.11}$$

And the distance between aligned SRSFs:

$$\sqrt{\int_0^1 |q_2 \circ (\gamma(x)) \sqrt{\gamma'} - q_1(x)|^2 dx + \lambda |1 - \gamma'(x)|^2} \tag{3.12}$$

is symmetric. Therefore, aligning the functions in SRSF space and then transforming the aligned SRSF back into function space provides a symmetric warping operation.

Once the optimal γ has been found, the final difference between two profiles $\hat{h}_1$ and $\hat{h_2}$ after alignment is defined as follows based on their SRSFs:

$$d_{1,2} = \sqrt{\int_0^1 |q_2 \circ \gamma(x) - q_1(x)|^2 dx} \tag{3.13}$$

Prior to alignment, all of the normalized profiles are smoothed using a 3-point running mean. This reduces small-scale variations that could cause local extremes in the derivative while maintaining the large-scale shape of the profile. The k-means algorithm (illustrated in figure 3.6) is then run as follows:

1. k cluster centers h_k are initialized from the normalized profiles.
2. All profiles $\hat{h}_i$, including the cluster centers, are converted to SRSFs q_i
3. Each SRSF q_i is aligned to each cluster center q_k to create warped functions q_{iw}
4. Each q_i is assigned to a cluster based on the closest center as defined by equation 3.13
5. For each cluster, a new center is defined as the mean of the aligned SRSFs.
6. The difference between the previous $(n-1)$ and new (n) iteration for each cluster center q_k is computed:

$$D_{k,n} = \frac{||q_{k,n-1} - q_{k,n}||}{||q_{k,n-1}||} \tag{3.14}$$

7. If the mean $\overline{D_{kn}}$ across all clusters is lower than the user-specified convergence threshold or has reached the maximum number of iterations, then the clustering stops and the current cluster centers are finalized. Otherwise, steps 2-6 are repeated in a new iteration.

We note that the results of k-means clustering are dependent on the initial centers chosen, and that the algorithm may converge on a local minimum rather than the absolute minimum. The k-means++ algorithm (Arthur and Vassilvitskii, 2007) is a commonly used method that aims to improve the selection of initial cluster centers by selecting the first cluster center at random, and

then selecting subsequent clusters centers from a probability distribution that is weighted according to the distance $d(q_i)$ of each datum q_i to the closest cluster center:

$$P(q_{ki} = q_i) = \frac{d(q_i)^2}{\sum_{q_j} d(q_j)^2} \tag{3.15}$$

Given that this region is dominated by cliffs (Gibbs and Richmond, 2015), the distribution of different shapes is uneven, with cliff-like profiles dominating other shore types by a large margin. As a result, randomly selecting profiles based on equation 3.15 may result in multiple similar cliff-like cluster centers and under-represent the full diversity of profile types. Instead of sampling our cluster centers from a probability distribution, we selected the first center from a uniform distribution and each subsequent center based on the q_i that minimizes equation 3.15. We used this method to generate 10 sets of 9 initial cluster centers (or seeds).

We ran this elastic functional k means algorithm for cluster numbers k ranging from 2 to 10 using the 10 aforementioned seeds sets, with a convergence threshold of .05 and a maximum of 10 iterations. We used a penalty value of $\lambda = .05$, which we found prevented concave profiles from becoming convex after being warped. In order to determine the best starting seed and optimal number of clusters k, we relied on both quantitative metrics and a qualitative assessment. For each model run, we calculated the silhouette score S (Rousseeuw, 1987) which can be computed uses pairwise distances between profiles as defined by equation 3.13: If a profile $\hat{h}_i$ belongs to cluster A, and cluster B is the next closest cluster the silhouette score $S(i)$ is:

$$S(i) = \frac{b(i) - a(i)}{max(a(i), b(i))} \tag{3.16}$$

where $a(i)$ is the mean distance between $\hat{h}_i$ and every other profile in cluster A, and $b(i)$ is the mean distance between $\hat{h}_i$ and every other profile in cluster B. A $S(i)$ value close to 1 suggests the profile is much closer to profiles in its cluster than to profiles in other clusters. A score of -1 suggests the profile is closer on average to profiles in a different cluster. For each k value, we selected the starting seeds set that resulted in the highest median $S(i)$ (see Supplementary Figure

3.18) as our final classification. We then inspected the median and distribution of $S(i)$, as well as the values of $S_c(i)$, the median score for each individual cluster. We identified candidate clusters that have a high $S_c(i)$ values, a high overall median, and a distribution skewed towards higher values of $S(i)$. Candidate clusters were evaluated based on qualitative assessments of the visual grouping of the original (unscaled) profiles into classes. The classified transects were also overlain on satellite imagery from Google Earth and compared to aerial photography from the ShoreZone database to evaluate the correspondence between different classes and visual shore types. In order to assess the along-shore cohesion of our classification and the relative spatial size of different clusters, we define along-shore *units* as continuous along-shore groups of transects that share the same class. For each cluster, we estimated the length of each unit and report the median and maximum.

Parameter clustering

We next subdivided the profiles in each form cluster based on the parameters W and H. Each profile is represented by a 2-dimensional vector $\overrightarrow{p} = (\hat{W}, \hat{H})$, where

$$\hat{W} = \frac{W - min(W)}{max(W) - min(W)} \tag{3.17}$$

$$\hat{H} = \frac{H - min(H)}{max(H) - min(W)} \tag{3.18}$$

We then clustered the parameterized profiles using the Kmeans package from scikit-learn(Pedregosa et al., 2011). Cluster centers

$$C = \begin{bmatrix} \hat{W_{c1}} & \hat{H_{c1}} \\ \hat{W_{c2}} & \hat{H_{c2}} \\ \dots & \dots \\ \hat{W_{ck}} & \hat{H_{ck}} \end{bmatrix}$$

are initialized randomly. Each data point $\overrightarrow{p_i}$ is assigned to the closest center based on Euclidean distance. After all data points have been assigned, the centers are redefined based on the

mean of all points in each cluster. The total inertia I of each iteration is calculated as the sum of the squares between each point and its cluster center:

$$I = \sum_{i}^{k} \sum_{x \in C_i} ||\overrightarrow{p} - \overrightarrow{\mu_i}||^2 \tag{3.19}$$

And the difference between the previous iteration cluster centers and the current iteration n is calculated as

$$D = ||C_n - C_{n-1}||_F \tag{3.20}$$

This is iterated until D falls below a user-specified threshold, which we defined as 0.0001. For each cluster number k, we ran 20 instances of k-means and selected the model with the lowest final inertia. Since the distribution of parameters is more even than for the functional forms, we utilize the standard k-means++ algorithm to initialize our clusters. This procedure was done separately for each functional cluster. We evaluated these candidate k values using the silhouette score and the same qualitative criteria used for form clustering.

3.3 Results

3.3.1 Functional clustering

We found the best distribution of silhouette scores (Figure 3.7) for k=2, with a median of 0.41 and range of -0.24 to 0.56. This means that while some profiles may be improperly classified, the majority of profiles are closer to profiles in their own cluster than in the other cluster. The silhouette scores drop as k is increased to 3 and 4, and then remain constant for larger k values. Based on these observations, we select k=2 as the best number of clusters. Our final form clusters (Figure 3.8) group the profiles into two physical types. Form cluster 0, which encompasses the majority (87.5 %) of the profiles, consists of cliff-like profiles with elevations that increase monotonically from the ocean inland and then flatten out onshore. Alongshore units in this class (Figure 3.10) have a large size variance, with lengths ranging from 10 to 2100 m and a median length of 140 m. Cluster 0 is

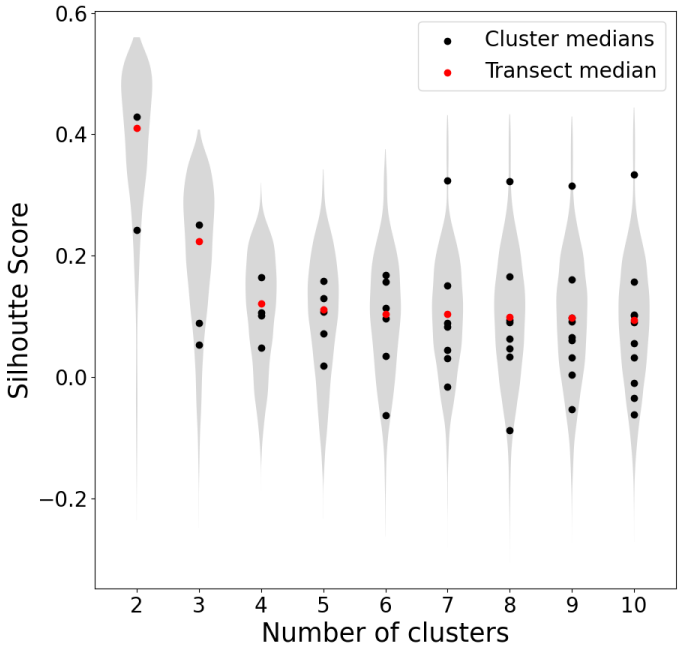


Figure 3.7: Distribution of silhouette scores for different cluster numbers for the form clustering. The median of each cluster and the overall median of the dataset is shown.

relatively well-partitioned, with a median silhouette score of 0.43. The remaining 12.5 % of the profiles are classified as Form Cluster 1, which is characterized by profiles that slope downwards onshore. Inspection of aerial photography and satellite imagery shows that this downwards slope can occur on multiple shore types, including beach-fronted lagoons, river and drainage channels (see Figure 3.15). The along-shore units classified as Form Cluster 1 are much smaller than Cluster 0, with a range of 10 m to 830 m and median of 20 m. The silhouette scores for profiles in Form Cluster 1 tend to be lower than in Form Cluster 0, with a median of 0.24. Both form clusters are present across the full range of the study area (Figure 3.9 a)), although the larger Form Cluster 1 units are located primarily in the northeast.

3.3.2 Parameter Clusters

We next subdivided Form Cluster 0 into parameter clusters. Based on the silhouette score distributions (figure 3.11 a)), we selected k=3 as the best fit, which results in a median silhouette

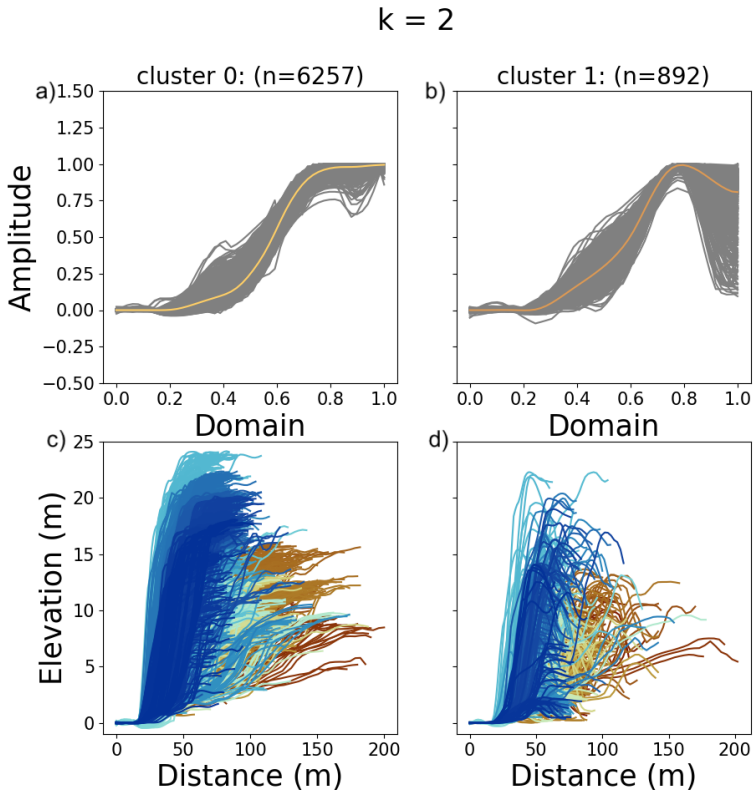


Figure 3.8: The final form clusters. Top: The center of each cluster and aligned normalized profiles. Bottom: The original profiles corresponding to each cluster

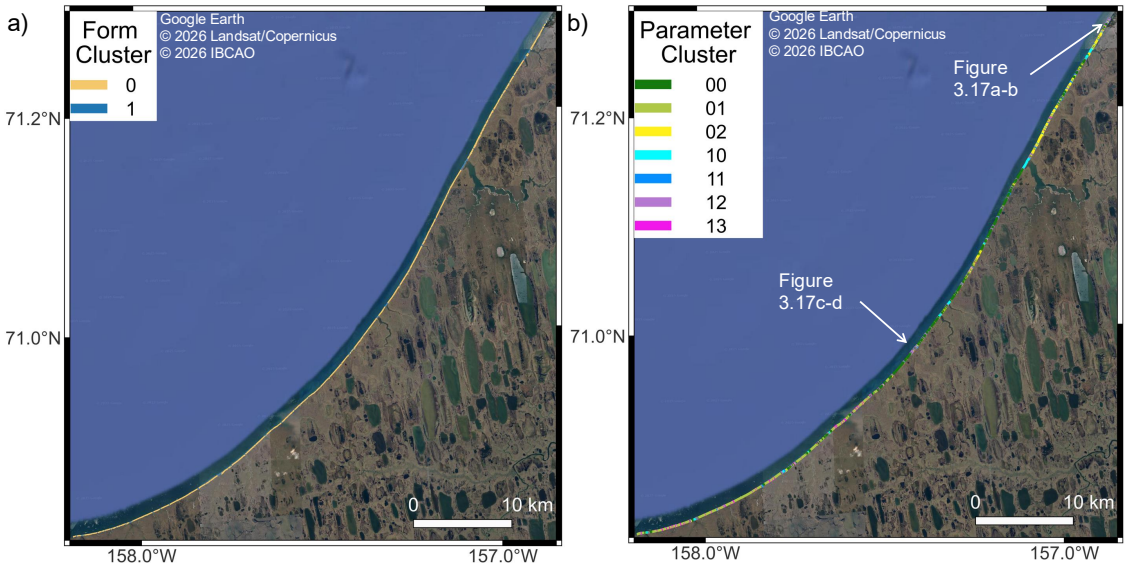


Figure 3.9: Map of the final transects labeled according to their a) form class and b) parameter class. The locations of the features shown in Figure 3.17 are indicated

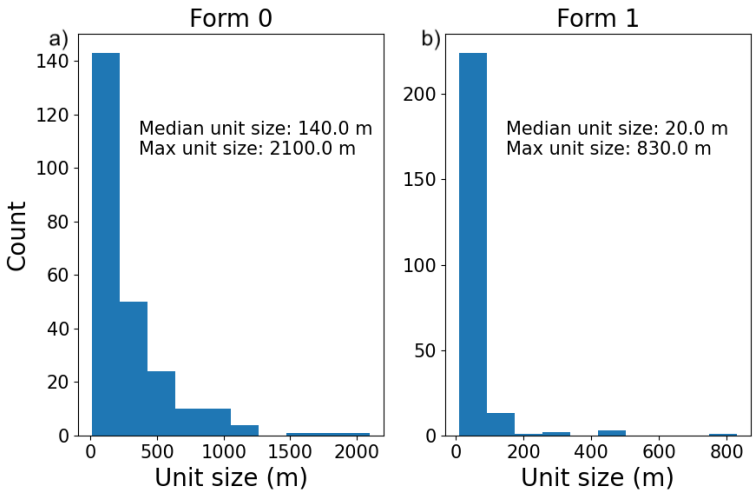


Figure 3.10: Size distribution of along-shore units corresponding to each form cluster

score of 0.51, range of -0.03 to 0.68, and median cluster scores ranging from 0.41 to 0.59 . When k is increased to 4 and 5, the median score decreases and the distribution of scores broadens to include more lower silhouette scores. The overall distributions for k values between 6 and 10 are similar to each other. Visual inspection of the classified transects overlain onto Google Earth imagery confirms that increasing k further leads to more frequent along-shore changes in class that do not appear to correspond to actual physical transitions. The 3 parameter clusters (Figure 3.12 a) and Figure 3.13) can be described as cliffs with different widths and heights: Cluster 00 (Figure 3.13 a), d)) consists of cliffs with low to intermediate heights ($<$ 14 m) and widths less than 70 m. Cluster 01 (Figure 3.13 b), e)) consists of tall ($\geq$ 14 m), cliffs with widths $<$ 90 m. Cluster 02 (Figure 3.13 c), f)) corresponds to wide (over 90 m) cliff-like features, with variable heights (3-17 m). Aerial photography (Figure 3.13 f)) shows that these high overall widths tend to be in part due to the presence of wide beaches. Cluster 01 has the largest continuous along-shore units, with a maximum size of 2100 m and median size of 135 m. While Cluster 00 and Cluster 02 have occasional large units (up to 1740 m and 1040 respectively), they both have a median size of 20 m, meaning that most of the along-shore units are small. These clusters are not evenly distributed across the study area (Figure 3.9 b)) - Cluster 02 is most prevalent in the northeast, Cluster 01 is most prevalent in the southwest, and Cluster 00 is most prevalent in intermediate latitudes.

For Form Cluster 1, we found that the highest maximum silhouette score (0.81) occurs at k=3,

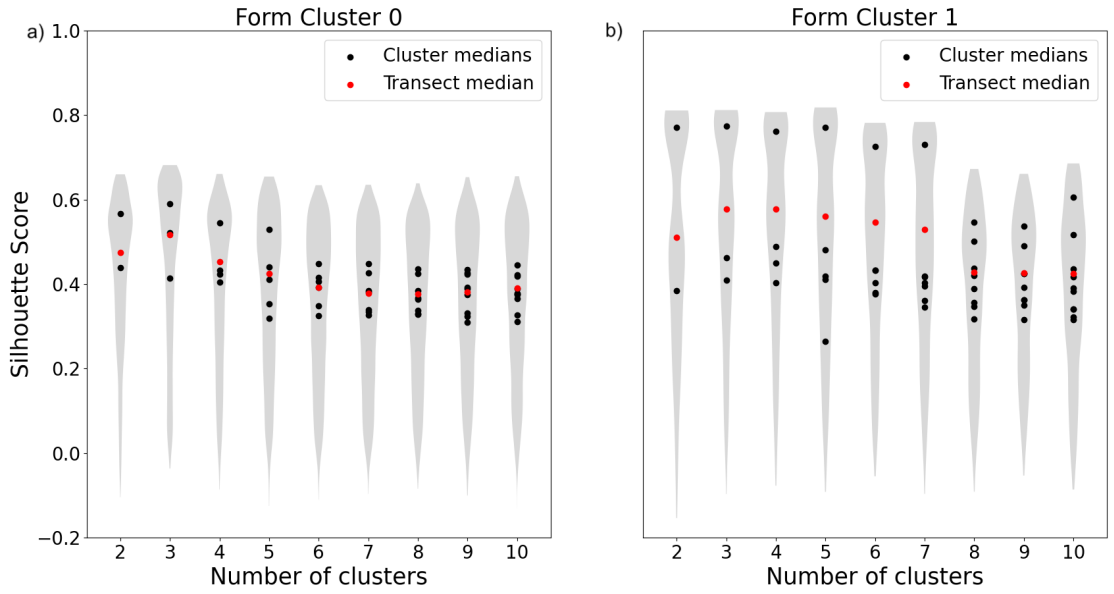


Figure 3.11: The distribution of silhouette scores for increasing k values for the parameter clustering step for each form cluster. The median of each cluster and the overall median of the dataset is shown

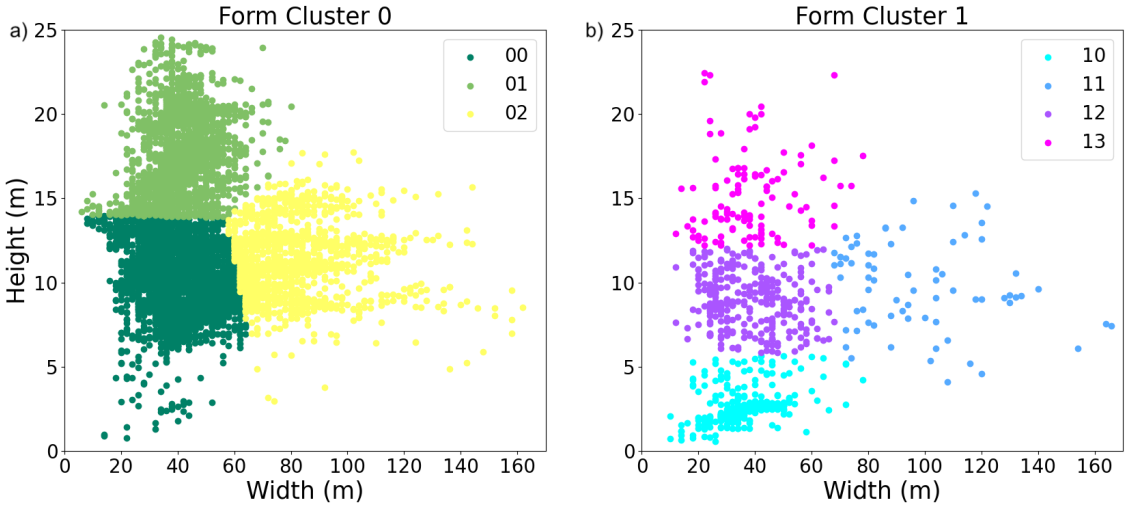


Figure 3.12: The distribution of parameters and their corresponding parameter cluster label for each form cluster.

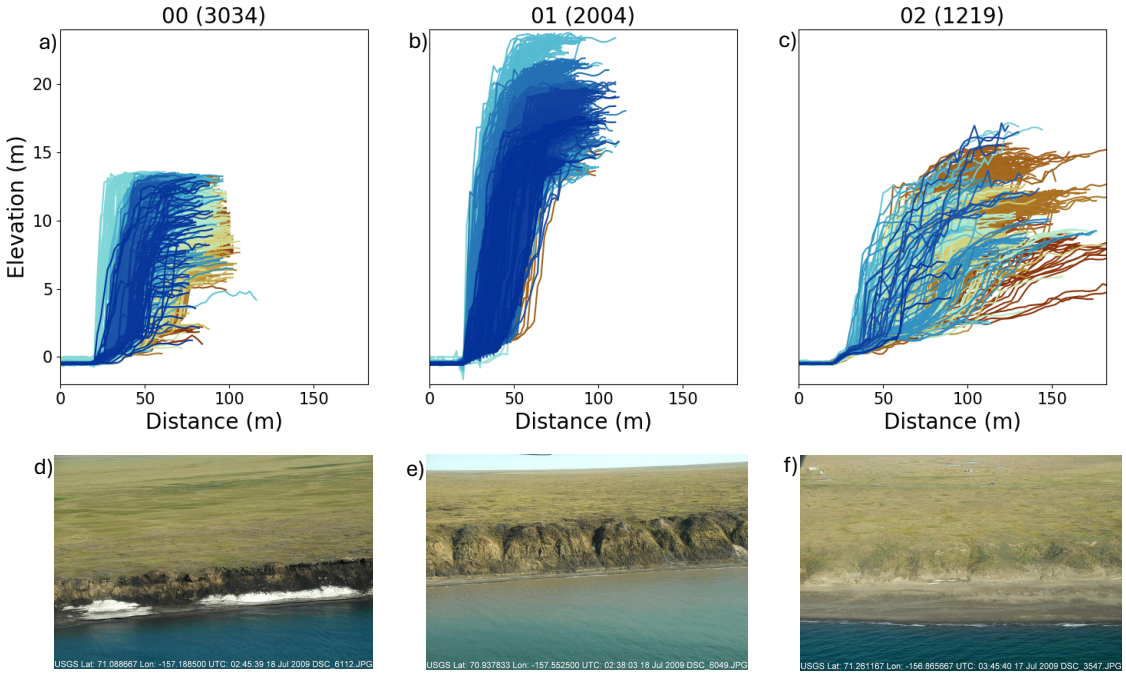


Figure 3.13: a-c: The transects corresponding to the parameter clusters for Form cluster 0. The number of transects in each cluster is provided in parenthesis. d-f: Aerial photographs from ShoreZone (Harper and Morris, 2014) showing examples of landforms characteristic of each cluster.

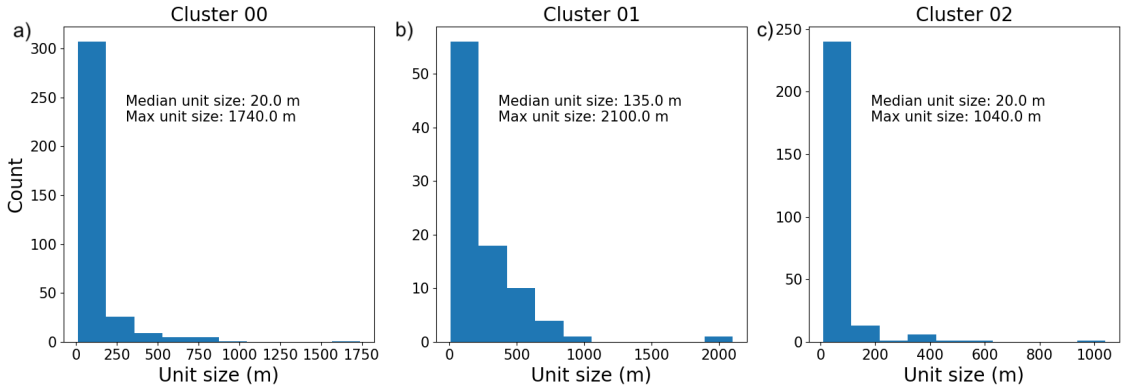


Figure 3.14: Along-shore unit size distribution for the parameter clusters in Form Cluster 0

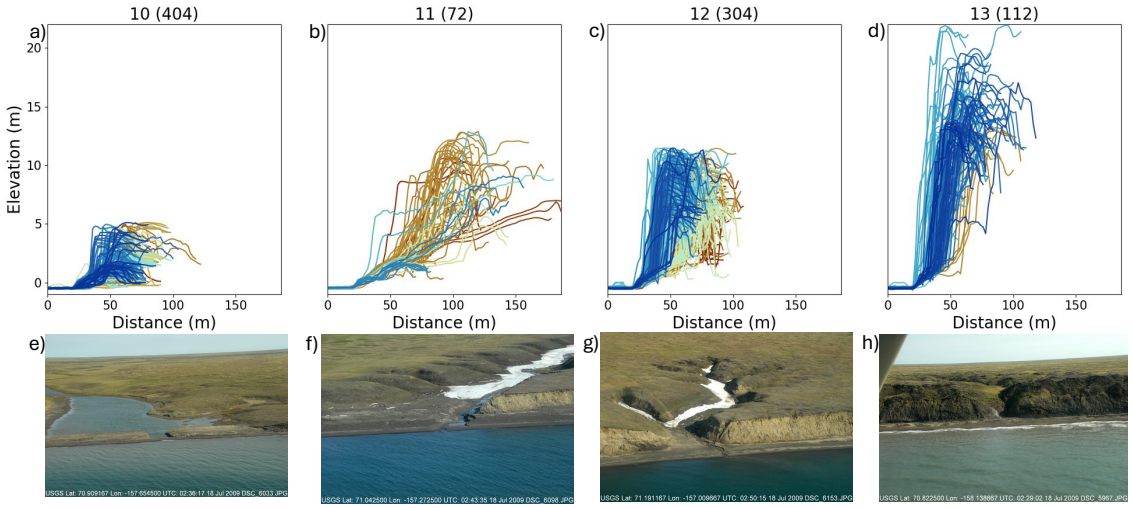


Figure 3.15: a-d: The transects corresponding to the parameter clusters for Form Cluster 1. The number of transects in each cluster is provided in parenthesis. e-h: Aerial photographs from ShoreZone (Harper and Morris, 2014) showing examples of landforms characteristic of each cluster.

while the highest overall median score (0.58) occurs at k=4. The overall distribution of silhouette scores remains similar for k=2 through k = 7, after which both the medians and the maximum drop substantially. The subdivision of Form Cluster 1 into 3 parameter clusters (Supplemental Figure 3.19) separates our downward-sloping profiles into different source features: beach-fronted lagoons (Figure 3.15 e)), wide features that are most commonly associated with dry river channel mouths (Figure 3.15 f)), and cliffs with small drainage channels (Figure 3.15 g) and h)). Separating Form cluster 1 into 4 clusters results in two clusters corresponding to small drainage channels: one for intermediate and low cliffs (6-12 m, Cluster 12 in Figure 3.15 c), g)), and one for higher cliffs ($>$ 12 m, Cluster 13 in Figure 3.15 d), h)). In order to be consistent with the height-dependent clusters in Form Cluster 0 (clusters 00 and 01), we propose using k = 4 as the final cluster number. The beach-fronted lagoons and wide features belong to Clusters 10 (Figure 3.15 a), e)) and 11 (Figure 3.15 b), f)) respectively. Cluster 10 is the largest of the Form 1 parameter clusters, with a maximum along-shore unit size of 830 m and a median of 40 m (figure ()). The other 3 form clusters are much smaller, with maximum unit sizes ranging from 60 m (Cluster 13) to 140 m (Cluster 12), and medians between 10-20m. Clusters 10 and 12 are fairly evenly distributed along the shoreline, while Cluster 11 is most prevalent in the North and Cluster 13 is most prevalent in the south.

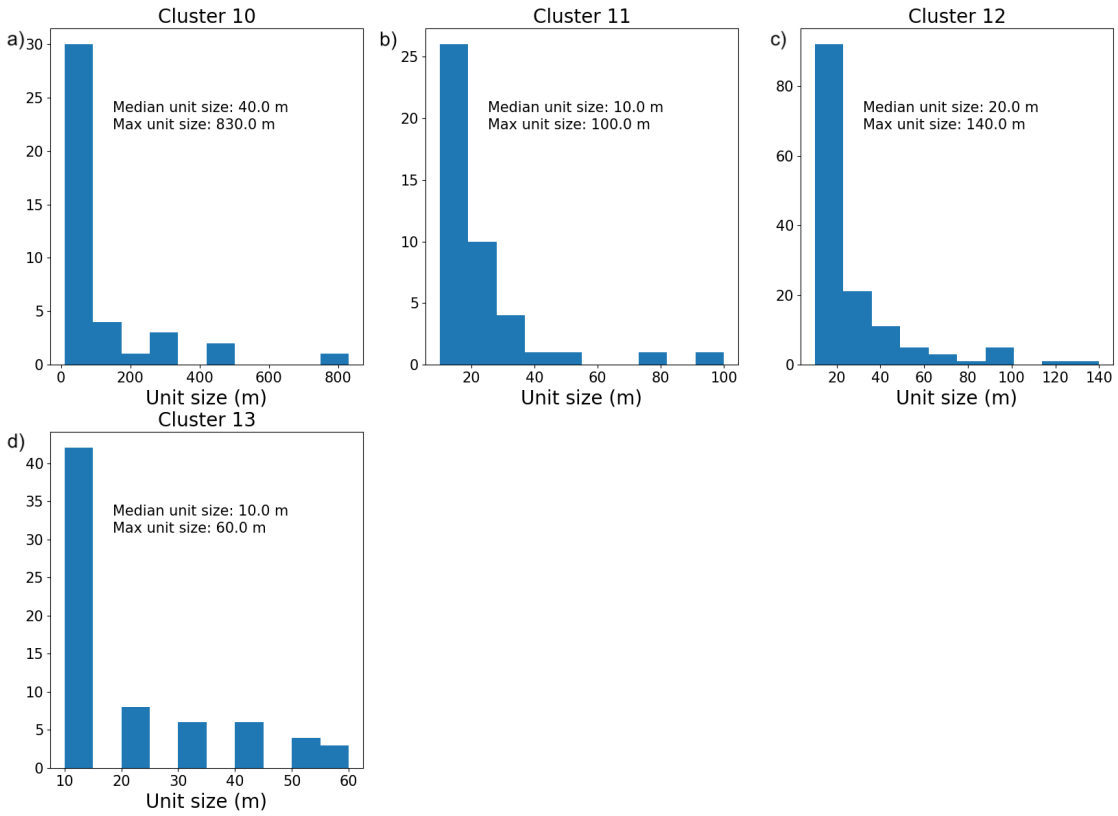


Figure 3.16: Along-shore unit size distribution for the parameter clusters in Form Cluster 1

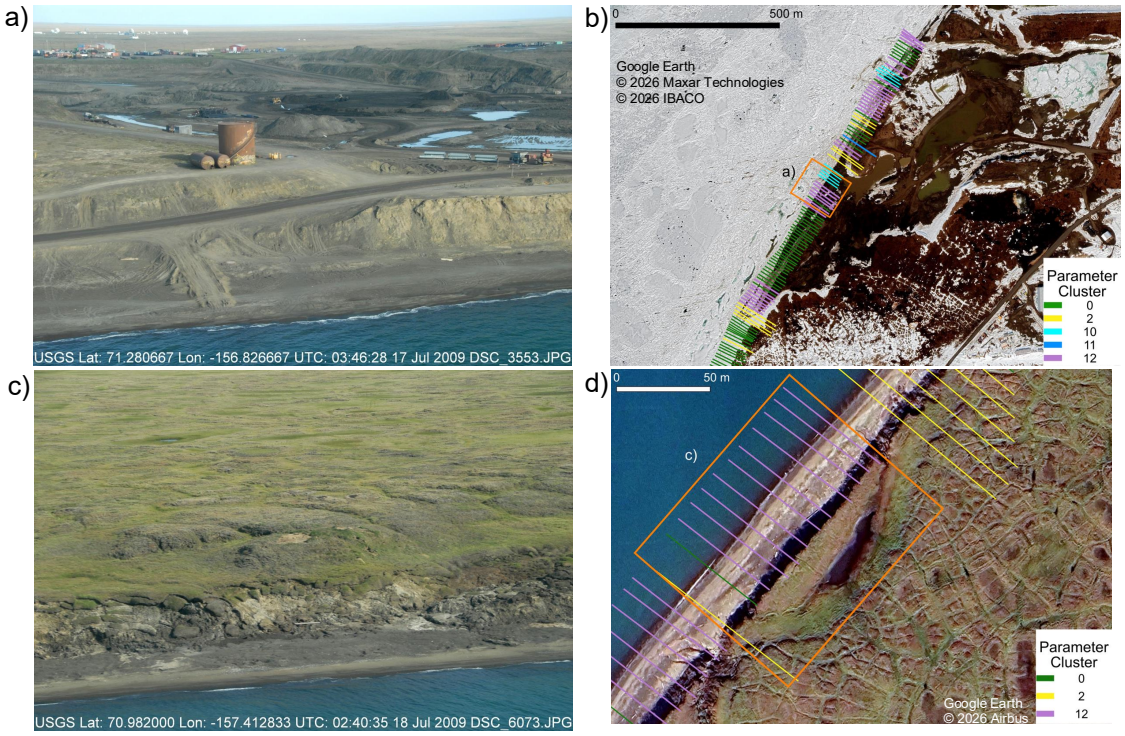


Figure 3.17: Notable features not represented in our classification: a): A developed site on the edge of Utqiagvik. b) The full stretch of developed shoreline is split between multiple classes. c) A section of slumped tundra, which gets assigned primarily to parameter cluster 12 (d). Aerial photographs are from ShoreZone. (Harper and Morris, 2014)

3.3.3 Unrepresented Features

While most of the shoreline can be described by the categories mentioned above, inspection of aerial photography and satellite imagery reveals some features that are not represented by their own class. Examples of these features are shown in Figure 3.17. Near Utqiagvik, there are man-made features due to construction (Figure 3.17 a), b)). From the photograph (Figure 3.17 a)), we can see that the shore form is variable. As a result, transects crossing over this region are classified as a combination of clusters 00, 02, 10, 11, and 12. We also identified a section of tundra that is slumped (Figure 3.17 a)) due to permafrost degradation, possibly from flooding. This section is primarily classified as cluster 12 (low-intermediate river channels)(Figure 3.17).

3.4 Discussion

3.4.1 Physical interpretation of clusters

Our clustering method divides profiles into groups that are physically distinct. The division of profiles into long segments of cliff-like features and shorter downwards-sloping hydrological features is consistent with Gibbs and Richmond (2015)'s description of the region as predominantly bluffs that are intersected with rivers and drainage channels. Our parameter clusters allow us to further segregate these categories into different height and width groups, as well as distinguish between different physical features such as active rivers and small drainage channels. Given that bluff height and beach width have been used as inputs for Arctic erosion modeling (Rolph et al., 2022), segregating groups by their overall height and width may be valuable for shoreline change assessments.

We do note that these classes do not capture the full diversity of shore types in our study area - isolated features such as the slumped tundra and construction site are not well-represented. While the profiles from these features may resemble other profiles in their clusters, they are clearly different physical landscapes and may evolve differently than the average shore type in their respective clusters. It may be that there are too few profiles from these features to define their own cluster, or that the parameters used for clustering are not sufficient to distinguish them from our other shore types. A different clustering technique, different parameterization, or the incorporation of additional datasets such as surface reflectance may improve our ability to identify these more unique features.

3.4.2 Spatial distribution of clusters

The large-scale spatial patterns observed in our clusters is consistent with what we would expect. The concentration for wide clusters (clusters 02, 11, see Figure 3.9) in the northeast and the concentration of tall clusters (clusters 01, 13) in the southwest is consistent with the overall trends in along-shore width and height (Figure 3.3). The difference in unit sizes is also physically interpretable. Form Cluster 0 having larger unit widths than Form Cluster 1 (Figure 3.10) is

reasonable, as we would expect hydrologic features to be localized, and cliff sections to be long. It is also expected that river mouths (Cluster 10) would be larger on average than drainage channels (Clusters 12 and 13, Figure 3.16).

While we do find some large continuous along-shore units (Figures 3.9, 3.10, 3.14, 3.16), the overall along-shore variability is high, with 10-30 m units being prevalent among every cluster. Small units are expected for small features such as drainage channels that are not well-sampled at the 10-m scale. If there are large along-shore jumps in width and height, some of the transects sampling these small-scale features may have been removed by the filtering and outlier procedure in section 3.2.2 (figure 3.3), further reducing their along-shore sampling rate. Small units can also occur due to misclassifications or a poor similarity of a given profile to any of the cluster centers. We note that our parameter clusters (Figure 3.12) are not well-separated, resulting in some overlap of the widths and heights of different clusters. This can lead to frequent along-shore switching between neighboring clusters, such as cliffs and drainage channels of different widths/heights. Along-shore smoothing paired with the detection of within-cluster outliers or defining strict height/width boundaries between clusters post-clustering may help provide more consistent along-shore clustering and identify transects that do not fit well in any cluster.

3.4.3 Subjective choices in the classification method and opportunities for improvement

We note that there are multiple subjective choices made in our clustering workflow and multiple opportunities for further testing and refinement. Our choice of a low warping constraint γ in equation 3.12 means that our clusters are based primarily on monotonicity and are insensitive to the backshore slopes of the original profiles. Increasing γ would allow for less warping between profiles and cluster centers and could be used to create more form clusters with differing slopes. In addition, our parameterization of profiles is simple, and may not be sufficient to fully characterize elevation profiles. For example, separating our width and height parameters into beach width, beach height, backshore width, and backshore heights may allow for a more detailed separation of shore types. Integration of additional parameters from other data sources, such as multispectral imagery

(as is done in Xie et al. (2021)) or geologic and permafrost databases (as is done in Piliouras et al. (2023)) may also help develop more detailed clusters. Integrating multispectral imagery could also improve the detection of the shore zone in the transect processing phases, as shore zone delineations based solely on topographic boundaries tend to be less accurate than those estimated from visual indicators (Nijland et al., 2017).

The choice of the final cluster numbers k is also subjective. While we referenced silhouette scores as a quantitative metric for determining an appropriate k-value, the k-value with the highest cluster score is not guaranteed to provide the 'best' model fit, and different values of k can have comparable silhouette score distributions, as is seen in the parameter clustering step (Figure 3.11). Bringing in additional data such as satellite and aerial imagery is helpful for informing appropriate k values for both form and parameter clustering. The best k value may also be informed by the specific scientific needs of a study. For example, while we prioritized maximizing the silhouette score and along-shore cohesion, choosing a higher value of k could be used to divide the clusters into more, narrower width and height groups at the cost of smaller along-shore units due to frequent switching between classes. Different clustering methods, including density-based clustering algorithms, may perform better for specific datasets, especially when parameters are poorly separated.

Finally, we note that k-means clustering is inherently a relative classification method, where the resulting classes depend on the specific subset of data used. If we were to re-run our workflow on a subset of our study area or a different region, we would most likely get different classes with different forms and parameter bounds. Thus, this method is not meant to provide a large-scale, comprehensive classification like ShoreZone or the Arctic Coastal Dynamics Database, but instead help interpret the shoreline variability within a specific region. Future work should explore the sensitivity of this workflow to different study area sizes.

3.5 Conclusions

We have developed a framework for classifying shore types based on k-means clustering of elevation profiles. This workflow performs the clustering in two steps: first by clustering the profiles'

normalized forms, and then subdividing these form clusters into parameter clusters based on their overall heights and widths. By running our workflow over a $\sim$ 72 km long lidar DEM over the Chukchi Sea coast, we categorize the shoreline into two basic forms: cliffs and downward-sloping features that correspond to permanent or transient water pathways. Our parameter clusters separate our cliff-like class into cliffs of different widths and heights and our downward-sloping class into river mouths, drainage channel mouths, and high and low cliffs intersected by drainage channels. This representation captures the most commonly occurring landforms in our study area, but does not account for less common features such as man-made features and slumped tundra. The large-scale spatial distribution of clusters and the size distribution of their units are physically reasonable, but there is small-scale along-shore variability driven by misclassifications and poor cluster separation. We note that the parameterization used here is fairly simple, and the final choice of the number of clusters is subjective. The goal of this work is not to provide the 'best' possible classification scheme, but to demonstrate the potential for unsupervised classification to capture physically meaningful differences in cross-shore profiles, and to provide a quantitative classification framework that can be improved upon and modified to fit specific research needs.

3.6 Acknowledgments

This work was supported by NASA grant no. 80NSSC24K0019.

This work is based on unpublished research done in collaboration with A. Borsa and A.Young. The dissertation author was the primary researcher on this project.

3.7 Supplementary Figures

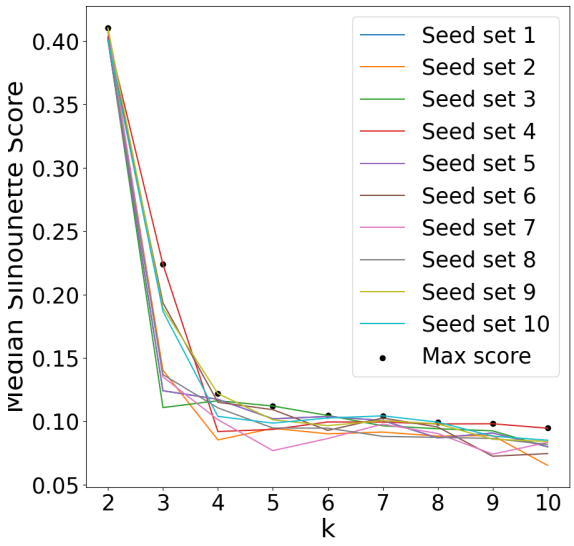


Figure 3.18: The median silhouette score as a function of k for the 10 sets of seeds tested. The seed set with the maximum score for each k was used for the final evaluation in Figure 3.7

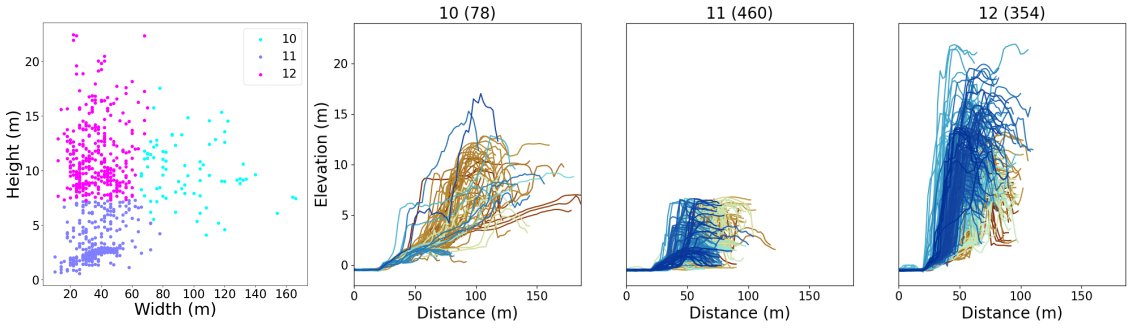


Figure 3.19: The distribution of parameters for Form Cluster 1 when split into 3 parameter clusters.

References

Arthur, D. and Vassilvitskii, S. (2007). k-means++: The Advantages of Careful Seeding. In *Proceedings of the eighteenth annual ACM-SIAM symposium on Discrete algorithms*, SODA '07, pages 1027–1035, New Orleans, Louisiana. Society for Industrial and Applied Mathematics.

Bryant, M. B., Borsa, A. A., Masteller, C. C., Michaelides, R. J., Siegfried, M. R., Young, A. P., and Anderson, E. J. (2025). Multiple modes of shoreline change along the Alaskan Beaufort Sea observed using ICESat-2 altimetry and satellite imagery. *The Cryosphere*, 19.

Farquharson, L., Mann, D., Swanson, D., Jones, B., Buzard, R., and Jordan, J. (2018). Temporal and spatial variability in coastline response to declining sea-ice in northwest Alaska. *Marine Geology*, 404:71–83.

Gibbs, A. E., Ohman, K. A., Coppersmith, R., and Richmond, B. M. (2024). National Assessment of Shoreline Change: A GIS compilation of updated vector shorelines and associated shoreline change data for the north coast of Alaska, U.S. Canadian border to Icy Cape.

Gibbs, A. E. and Richmond, B. M. (2015). National assessment of shoreline change—Historical shoreline change along the north coast of Alaska, U.S.–Canadian border to Icy Cape. Open-File Report, U.S. Geological Survey.

Harper, J. and Morris, M. C. (2014). Alaska ShoreZone Coastal Habitat Mapping Protocol. Technical Report, Nuka Research and Planning Group, LL.

Irrgang, A. M., Bendixen, M., Farquharson, L. M., Baranskaya, A. V., Erikson, L. H., Gibbs, A. E., Ogorodov, S. A., Overduin, P. P., Lantuit, H., Grigoriev, M. N., and Jones, B. M. (2022). Drivers, dynamics and impacts of changing Arctic coasts. *Nature Reviews Earth & Environment*, 3(1):39–54.

Irrgang, A. M., Lantuit, H., Manson, G. K., Günther, F., Grosse, G., and Overduin, P. P. (2018). Variability in Rates of Coastal Change Along the Yukon Coast, 1951 to 2015. *Journal of Geophysical Research: Earth Surface*, 123(4):779–800.

Jones, B. M., Farquharson, L. M., Baughman, C. A., Buzard, R. M., Arp, C. D., Grosse, G., Bull, D. L., Günther, F., Nitze, I., Urban, F., Kasper, J. L., Frederick, J. M., Thomas, M., Jones, C., Mota, A., Dallimore, S., Tweedie, C., Maio, C., Mann, D. H., Richmond, B., Gibbs, A., Xiao, M., Sachs, T., Iwahana, G., Kanevskiy, M., and Romanovsky, V. E. (2018). A decade of remotely sensed observations highlight complex processes linked to coastal permafrost bluff erosion in the Arctic. *Environmental Research Letters*, 13(11):115001.

Jones, B. M., Stoker, J. M., Gibbs, A. E., Grosse, G., Romanovsky, V. E., Douglas, T. A., Kinsman, N. E. M., and Richmond, B. M. (2013). Quantifying landscape change in an arctic coastal lowland using repeat airborne LiDAR. *Environmental Research Letters*, 8(4):045025.

Joregenson, T. M., Kanevskiy, M., Shur, Y., Grunblatt, J., Ping, C.-L., and Michaelson, G. (2015). permafrost-characterization-and-mapping-for-northern-alaska-final-2015.pdf. Technical Report, U.S. Fish and Wildlife Service.

Lantuit, H., Overduin, P. P., Couture, N., Wetterich, S., Aré, F., Atkinson, D., Brown, J., Cherkashov, G., Drozdov, D., Forbes, D. L., Graves-Gaylord, A., Grigoriev, M., Hubberten, H.-W., Jordan, J., Jorgenson, T., Ødegård, R. S., Ogorodov, S., Pollard, W. H., Rachold, V., Sedenko, S., Solomon, S., Steenhuisen, F., Streletskaya, I., and Vasiliev, A. (2012). The Arctic Coastal Dynamics Database: A New Classification Scheme and Statistics on Arctic Permafrost Coastlines. *Estuaries and Coasts*, 35(2):383–400.

Lara, M. J., Nitze, I., Grosse, G., and McGuire, A. D. (2018). Tundra landform and vegetation productivity trend maps for the Arctic Coastal Plain of northern Alaska. *Scientific Data*, 5(1):180058.

Lim, M., Whalen, D., Martin, J., Mann, P. J., Hayes, S., Fraser, P., Berry, H. B., and Ouellette, D. (2020). Massive Ice Control on Permafrost Coast Erosion and Sensitivity. *Geophysical Research Letters*, 47(17).

Liu, C., Li, J., Tang, Q., Qi, J., and Zhou, X. (2022). Classifying the Nunivak Island Coastline Using the Random Forest Integration of the Sentinel-2 and ICESat-2 Data. *Land*, 11(2):240.

Nielsen, D. M., Pieper, P., Barkhordarian, A., Overduin, P., Ilyina, T., Brovkin, V., Baehr, J., and Dobrynin, M. (2022). Increase in Arctic coastal erosion and its sensitivity to warming in the twenty-first century. *Nature Climate Change*, 12(3):263–270.

Nijland, W., Reshitnyk, L. Y., Starzomski, B. M., Reynolds, J. D., Darimont, C. T., and Nelson, T. A. (2017). Deriving Rich Coastal Morphology and Shore Zone Classification from LIDAR Terrain Models. *Journal of Coastal Research*, 33(4):949–958.

NOAA (2025). Custom processing of "2010 USGS Lidar: North Slope, Alaska". Dataset, NOAA Office for Coastal Management, Charleston, SC. https://coast.noaa.gov/dataviewer.

OCM Partners (2026). 2010 USGS Lidar: North Slope, Alaska from 2010-06-15 to 2010-08-15. https://www.fisheries.noaa.gov/inport/item/52766.

Pedregosa, F., Varoquaux, G., Org, N., Gramfort, A., Michel, V., Fr, L., Thirion, B., Grisel, O., Blondel, M., Prettenhofer, P., Weiss, R., Dubourg, V., Vanderplas, J., Passos, A., Tp, A., and Cournapeau, D. (2011). Scikit-learn: Machine Learning in Python. *Journal of Machine Learning Research*, 12:2825 – 2830.

Piliouras, A., Jones, B. M., Clevenger, T., Gibbs, A. E., and Rowland, J. C. (2023). Variability in terrestrial characteristics and erosion rates on the Alaskan Beaufort Sea coast. *Environmental Research Letters*, 18(11):114050.

Rolph, R., Overduin, P. P., Ravens, T., Lantuit, H., and Langer, M. (2022). ArcticBeach v1.0: A physics-based parameterization of pan-Arctic coastline erosion. *Frontiers in Earth Science*, 10.

Rousseeuw, P. J. (1987). Silhouettes: A graphical aid to the interpretation and validation of cluster analysis. *Journal of Computational and Applied Mathematics*, 20:53–65.

Swirad, Z. M. (2021). CliffDelineaTool. https://github.com/zswirad/CliffDelineaTool.

Swirad, Z. M. and Young, A. P. (2022). CliffDelineaTool v1.2.0: an algorithm for identifying coastal cliff base and top positions. *Geoscientific Model Development*, 15(4):1499–1512.

Tucker, D. J. (2024). FDASRSF. https://github.com/jdtuck/fdasrsf_python.

Tucker, J. D., Wu, W., and Srivastava, A. (2013). Generative models for functional data using phase and amplitude separation. *Computational Statistics & Data Analysis*, 61:50–66.

Vos, K., Splinter, K. D., Harley, M. D., Simmons, J. A., and Turner, I. L. (2019). CoastSat: A Google Earth Engine-enabled Python toolkit to extract shorelines from publicly available satellite imagery. *Environmental Modelling & Software*, 122.

Wu, W. and Srivastava, A. (2011). An information-geometric framework for statistical inferences in the neural spike train space. *Journal of Computational Neuroscience*, 31(3):725–748.

Xie, H., Sun, Y., Liu, X., Xu, Q., Guo, Y., Liu, S., Xu, X., Liu, S., and Tong, X. (2021). Shore Zone Classification from ICESat-2 Data over Saint Lawrence Island. *Marine Geodesy*, 44(5):454–466.

Zang, X., Kurtek, S., Chkrebtii, O., and Tucker, J. D. (2020). Elastic k-means clustering of functional data for posterior exploration, with an application to inference on acute respiratory infection dynamics. arXiv:2011.12397 [stat].

Chapter 4

Variations in shoreline change between shore types on the East Chukchi Sea

Abstract

In this chapter, we examine long-term shoreline change rates across a 72 km stretch of the Western Chukchi Sea and consider how these change rates may be related to spatial variations in meteorological forcings, sediment composition, and topographically defined shore classes. We used retreat rates from the USGS that span 1947-2010 and are available every 50m alongshore. We used a combination of CARRA2, modeled nearshore waves from USGS, and DAYMET to evaluate spatial patterns in long-term averages and extremes in open water days, sea surface temperature, wave power and direction, air temperature and precipitation. We also assessed variations in shoreline composition reported in the ShoreZone database. We then compare retreat rates between different shore types defined by an unsupervised classification of airborne lidar data. We find the least retreat and highest advancement in the northeast, and the highest retreat in the southwest. We hypothesize that the large-scale variations in shoreline change are driven by spatial differences in wave exposure, sediment supply, wave temperature, and atmospheric conditions. We also find differences in retreat rates between different shore types. Wide shore types are primarily in areas that have seen little retreat or some accumulation. River mouths have retreated more than cliff-like landforms, possibly due to the migration of sediment from these rivers to nearby beaches. We also find that high cliffs have retreated more than lower cliffs, although it is hard to determine whether this is due to physical differences between these two shore types or because they tend to be located

in different parts of the study area with different atmospheric and oceanic conditions and different sediment types. We do not find significant differences in shoreline change rates between cliffs with and without drainage channels, but note that the sample size of drainage channels is small. Overall, we conclude that the observed spatial variations in this region are likely due to a combination of spatially varying meteorological forcings, material composition and shore morphology, and that more in-depth analysis is needed to separate the effects of these different factors.

4.1 Introduction

Now that we have developed a large-scale coastal classification method, we can use these classes to examine the relationship between topographic shore types and patterns of shoreline change. Previous research has pointed to different shore types having different patterns of shoreline change. For example, Farquharson et al. (2018) found varying shoreline change patterns across different geomorphic units in the Chukchi Sea, with permafrost bluffs and barrier islands primarily retreating and beaches and gravel barriers showing a mixture of retreat and advance. Piliouras et al. (2023) found that shoreline change along the Alaskan Beaufort Sea coast varied according to elevation, lithology, and barrier island presence. And Irrgang et al. (2018) found high rates of retreat across beaches, spits, inundated tundra, and active tundra cliffs, lower rates of retreat across tundra slopes and tundra flats, and accretion across gravel features. All three of these studies demonstrate different shoreline evolution among different shore types, while also highlighting the role of time and space-varying meteorological conditions in driving along-shore variability. While our classes are defined based on the cross-shore shape of the shoreline, material composition is also important. In this chapter, we evaluate long-term shoreline change rates on the Chukchi sea coast in the context of long-term ocean and atmospheric forcings, shoreline composition, and morphologic variability based on the classes derived in Chapter 3.

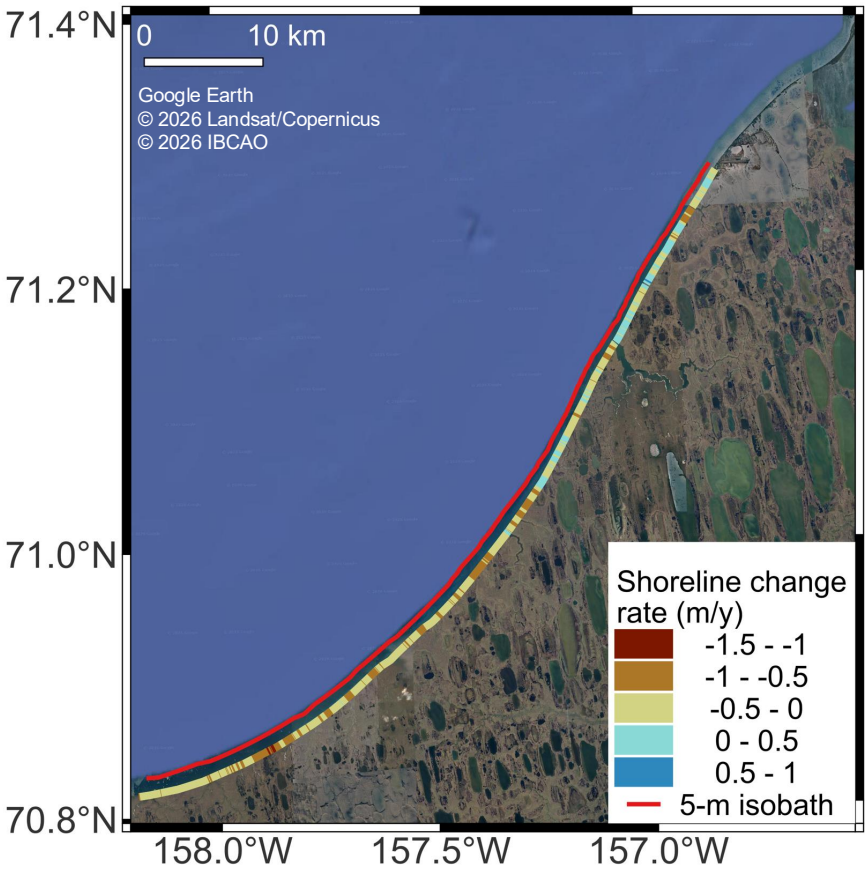


Figure 4.1: An overview of our study area with historical shoreline change rates from Gibbs et al. (2024). The location of the 5-m isobath where the wave model from Engelstad et al. (2024b) was generated is shown.

Table 4.1: Summary of meteorological datasets used and the derived quantities

Source	Resolution	Variables	Derived quantities
CARRA2	2.5 km x 2.5 km grid daily	sea ice concentration, SST	open water days, mean/max summer SST
DAYMET	1 km x 1 km grid daily	2m min air temperature, 2m max air temperature, precipitation	mean summer temperature, summer rainfall
USGS waves	400 m alongshore every 3 hours	significant wave height wave period wave direction	mean annual wave power, mean annual wave direction, mean annual incidence angle

4.2 Data and Methods

4.2.1 Historical shoreline change rates

We used long-term shoreline change rates published by the US Geologic Survey (Gibbs et al., 2024; Gibbs and Richmond, 2015), which are estimated using 5 shorelines digitized from topographic sheets, orthorectified photographs, and digital elevation models spanning 1947 to 2010 (Gibbs and Richmond, 2017). Retreat rates (Figure 4.1) are provided as 500-m long cross-shore transects spaced every 50m along-shore. For each transect, the retreat rate was estimated as the slope of a linear fit to the shoreline position along the transect. Errors on the slope are reported in the form of a 90% confidence interval (CI), which we convert to a standard deviation σ using the formula:

$$\sigma = \frac{CI}{3.29} \tag{4.1}$$

To get the along-shore position of these retreat rates on the 2010 shoreline where our shoreline classifications are defined, we used the approximate water line estimated in Section 3.2.2 as a reference shoreline. We smoothed this shoreline with a 50-m running mean to reduce small-scale alongshore undulations. We used the intersection point between the USGS transects and our reference shoreline as the along-shore coordinates of each retreat measurement.

4.2.2 Meteorological datasets

Large-scale variations in permafrost thaw and shoreline change are driven in part by meteorological forcings including air and ocean temperature, precipitation, and wave conditions (Aré, 1988; Baranskaya et al., 2021; Günther et al., 2013; Zwieback et al., 2018). Therefore, an evaluation of shoreline change across different shore types needs to also account for variations in along-shore meteorological forcings. We compiled sea ice concentration, wave statistics, ocean temperature, air temperature and precipitation from multiple data sources, listed in table 4.1 and summarized below. We compiled this data between 1980-2010, as this time range is covered by all three datasets.

Sea ice and ocean temperature from CARRA2

The majority of shoreline change on the Arctic coastline takes place during the open water season, when there is no landfast or nearshore ice to protect the shoreline from waves. During the open water season, the frozen coastline is subject to both thermal and mechanical erosion (Aré, 1988; Baranskaya et al., 2021; Günther et al., 2013; Overeem et al., 2011), and thus depends on the ocean temperature, wave action, and the length of the open water season. We obtained sea ice coverage and sea surface temperature (SST) from the Second-Generation Copernicus Arctic Regional Reanalysisis (CARRA2) dataset (Pelt et al., 2025), which provides daily sea ice and ocean conditions on a 2.5 km grid. We sampled sea ice concentration and sea surface temperature from the 31 grid cells that were nearest to the shore and had valid data. For each year, we estimated the number of open water days (owd) as the number of days for which the mean sea ice concentration was less than 15%, following Overeem et al. (2011). We then calculated the mean and maximum number of open water days per year between 1980-2010 for each location over our study area. The mean and maximum SST at each location was estimated by averaging daily SST values over each open water season.

Wave data from USGS

In order to examine spatial variations in wave activity, we used modeled nearshore wave data published by the USGS (Engelstad et al., 2024b). This dataset provides downscaled waves

statistics based on the CMIP 6 CMCC CMCC-CM2-VHR4 wind and wave model (Scoccimarro et al., 2017), and is generated using the Simulating WAves Nearshore (SWAN) numerical model (Booij et al., 1999) with Wave Watch III outputs as boundary conditions (Engelstad et al., 2024a) and bathymetry from the International Bathymetric Chart of the Arctic Ocean (IBCAO) (Jakobsson et al. (2024), show in Supplementary Figure 4.17). The CMIP 6 input wave conditions are sampled at the 20 m isobath (Supplementary Figure 4.17), and SWAN is used to propagate the sea states and estimate the significant wave heights (H_S), mean period (T), and wave direction (θ_w) are provided every 400-m along the 5-m isobath (which is plotted in Figure 4.1 and runs roughly parallel to the shore) at 3-hour time intervals.

In order to summarize the wave conditions over the full time series of the dataset, we estimate the omnidirectional wave power J, and the direction of maximum wave energy θ_{max}. Ahn et al. (2023) proposed a method for estimating summary statistics from a time series of wave data by approximating the wave spectra from reported peak and mean wave statistics. Because the downscaled wave database (DWDB) only contains mean wave statistics, we simplify this method. For each location, we divide the N observations in $n \times m$ bins, where n is number of unique frequencies and m is the number of unique directions in the time series. We then estimate the components of the wave spectra $\overline{S_{ij}}$ by averaging the wave energy in each frequency and direction bin:

$$\overline{S_{ij}} = C\Big(\sum_{f_p \in f_i, \theta_p \in \theta_j} \frac{H_{s_p}^2}{16 = \Delta f_i \Delta \theta_i}\Big)/N \tag{4.2}$$

$$C = \frac{\sum_n H_{s_n}^2/16N}{\sum_{i,j} \Delta f_i \Delta \theta_j} \tag{4.3}$$

$$\Delta f_i = \frac{f_{i+1} - f_{i-1}}{2} \tag{4.4}$$

$$\Delta \theta_j = \frac{\theta_{j+1} - \theta_{j-1}}{2} \tag{4.5}$$

where p is the number of individual observations in the ith and jth frequency and directional bins.

We then calculate J as:

$$J = \rho g \sum_{i,j} c_{g_i} S_{ij} \Delta f_i \Delta \theta_j \tag{4.6}$$

and θ_{max} as the angle that maximizes the directional energy $J(\theta)$:

$$J(\theta) = \rho g \sum_{i,j} c_{g_i} S_{ij} \Delta f_i \Delta \theta_j cos(\theta - \theta_j)\delta \tag{4.7}$$

$$\delta = \begin{cases} 1 & \text{if } \theta - \theta_j > 0 \\ 0 & \text{if } \theta - \theta_j \leq 0 \end{cases}$$

Where ρ is the density of seawater, g is the gravitational constant, and c_{g_i} is the group velocity of waves at a frequency f_i. We test Equation 4.7 for angles ranging from 0 to 360° in 1° intervals to identify θ_{max}. Since the waves are at a fixed depth (h) of 5 m, we can use the dispersion relationships (Dingemans, 1997) to calculate the wave number k and the group velocity c_{g_i}:

$$(\frac{2\pi f_i}{k})^2 = gktanh(kh) \tag{4.8}$$

$$c_{g_i} = \frac{\pi f_i}{k}(1 + \frac{2kh}{sinh(2kh)}) \tag{4.9}$$

This approach was also used to create representative wave vectors of the input CMIP-6 waves (Supplementary Figure 4.17). We also calculate $\overline{\theta_I}$, the incidence angle between θ_{max} and the local 5-m isobath.

Temperature and precipitation from DAYMET

In addition to thermomechanical forcing at the beach and cliff base, permafrost coasts can also experience top-down thawing and mass wasting from warm air temperatures (Baranskaya et al., 2021; Günther et al., 2013) and rainfall (Zwieback et al., 2018). We extracted daily observations of

the minimum and maximum 2m air temperature (T_{min} and T_{max} respectively), daily precipitation, and snow water equivalent (SWE) between June 1st and October 31st of each year along our reference shoreline from the DAYMET reanalysis dataset (Thornton et al., 2022) using the Python Single Pixel Extraction Tool (Thornton and Devarakonda, 2011), which provides atmospheric conditions on a daily basis on a 1 km grid. We calculated the mean temperature, $T_m = \frac{\overline{T_{max} - T_{min}}}{2}$ and the mean annual cumulative precipitation. Since we are specifically interested in rain conducting heat on a snow-free tundra, we only included precipitation from days where SWE is 0.

4.2.3 Shoreline composition from ShoreZone

In addition to meteorology and morphology, shoreline change rates are also dependent on the material or sediment type (Kriebel and Dean, 1985), i.e. geology and grain size. We used material types reported in the ShoreZone database (Harper and Morris, 2014), a comprehensive geomorphic database created based on expert analysis of airborne imagery. The shoreline is divided into alongshore units (which can range from 10s of meters to several kilometers in length) that share a common shore form. Each alongshore unit is broken into across-shore zones and components based on wave exposure and changes in form or material, as illustrated in Supplementary Figure 4.18. The primary zones are the supratidal zone, which lies above the maximum water line; the intertidal zone, which lies between the minimum and maximum tidal water lines; and the subtidal zone, which lies below the minimum water line. In our study region, only the supratidal and intertidal zones are defined. A single zone is often subdivided into across-shore components, according to transitions in the shore form or material. While these components can be further divided into primary, secondary, and tertiary materials, here we only consider the primary material of each component. The component materials are provided as letter codes. Upper case letters indicate the general class, which in this region can be 'Clastic' (C), 'Biogenic' (B), 'Anthropogenic' (A), or 'Bedrock' (R). The general class codes are accompanied by lower case letters indicating the more specific materials, which are listed in Table 4.2. Permafrost, by definition, is defined by temperature and not sediment type. As a result, there is a material code for permafrost present in both the

Table 4.2: Material class code compiled from ShoreZone. Note that the bedrock class (R) had no subcodes present in our study region

Primary Class	Code	Meaning
A: Anthropogenic	a	metal structure
	d	man-made debris
	f	fill
B: Biogenic	g	fine shell
	l	dead trees
	o	organic litter
	p	peat
	z	permafrost
C: Clastic	c	cobbles
	d	diamicton (poorly sorted mud)
	f	fines (silt/clay mud)
	p	pebbles
	s	sand
	z	permafrost
R: Bedrock	N/A	N/A

'Clastic' and 'Biogenic' classes.

In order to create a simplified code for each alongshore unit, the codes for each component within a zone were combined, and duplicate letter codes were removed. While the original database orders the lower case letters in each class according to their relative abundance within the component, we sorted them alphabetically in order to reduce the total number of classes and simplify the dataset to represent the material types present regardless of abundance. For both the supratidal and intertidal zones, we plotted the spatial distribution of the primary classes, detailed classes, and permafrost presence. We note that since ShoreZone classifications are based on interpretation of aerial imagery, a lack of permafrost in the material code means that there are no surface expressions of permafrost (i.e. ground ice or surface deformation) and does not rule out the presence of sub-surface permafrost.

4.2.4 Comparing rates between shore types

We next evaluated retreat rates across our different shore types derived in Chapter 3 (Figure 3.9). For each along-shore location where a retreat transect intersects our baseline, we assigned it the class of the closest baseline point. We then aggregated the shoreline change rates associated

with each class and report the median and number of sampled transects per class. To estimate the uncertainty on our per-class medians, we propagated the reported shoreline change uncertainties σ using Monte Carlo sampling. For every individual shoreline change observation with value s and uncertainty σ_s within a given class, we resampled it from a gaussian distribution with mean s and standard deviation σ. We then calculated the median from these resampled values. We repeated this process 5000 times to create a distribution of median values. We reported the mean and standard deviation of this distribution as the final median and error on the median.

To assess whether different form and parameter classes have significantly different patterns of shoreline change, we made two comparisons. First, we compared the medians and their 95% confidence intervals based on their propagated errors. We also performed a 2-sample Kolmogorov-Smirnov (KS) test, which tests the hypothesis that two groups of samples come from the same distribution. For the form classes, we considered the KS statistic significant if its p-value was less than .05. When comparing our 7 parameter classes, we performed 21 pairwise tests, which increases the chance of a false positive result. To account for this, we adjusted our significant p-value threshold using the Bonferroni correction, meaning we scaled our significant p-value threshold by the number of tests performed:

$$p_n = \frac{p}{21}$$

or, equivalently, $p = 21p_n$. The KS test is sensitive to differences in both the center and shape of each distribution, meaning that a significant p-value does not always mean the distributions have different medians. We therefore required two conditions to be met for the medians of two classes to be considered significantly different:

1. The 2-sample K-S statistic is significant
2. There is little to no overlap between their 95% confidence intervals

We then performed a second set of pairwise KS tests between classes after removing their medians. If the KS statistic was significant for these centered distributions, we inferred that the

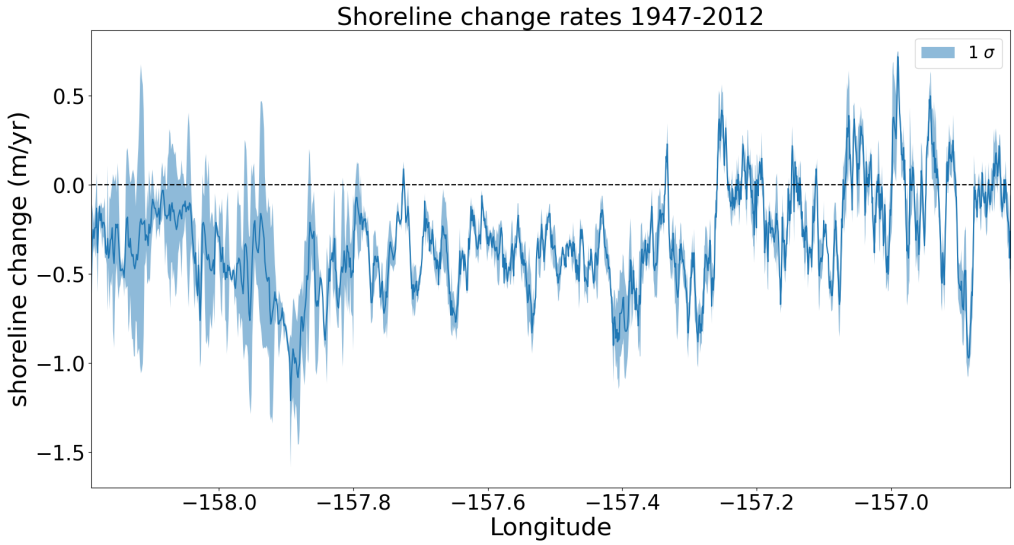


Figure 4.2: Historic retreat rates from USGS (Gibbs et al., 2024) and their measurement errors

shapes of the distributions are different.

4.3 Results

4.3.1 Overview of shoreline change rates

Shoreline change across our study area (Figure 4.2) is predominantly negative, with a mean of -0.3 m/yr, and range of -1.2 m/yr to 0.7 m/yr. The majority of shoreline advancement has occurred in the Northeast, while the highest retreat has occurred in the southwest. We also observed the highest errors in the southwest.

4.3.2 Historic meteorological conditions

The 30-year mean of CARRA2-derived open water days and sea surface temperature (Figure 4.3) show minor variations across the study area, with up to 98 open water days in the southwest and as low as 89 open water days in the northeast. The 30-year maximum open water season ranges by 39 days across the study area, with up to 171 open water days in a single year in the southwest and as low as 132 open water days in the northeast. We also observe minor variations in the sea surface temperature, with warmer mean and maximum temperatures in the southern pixels than the

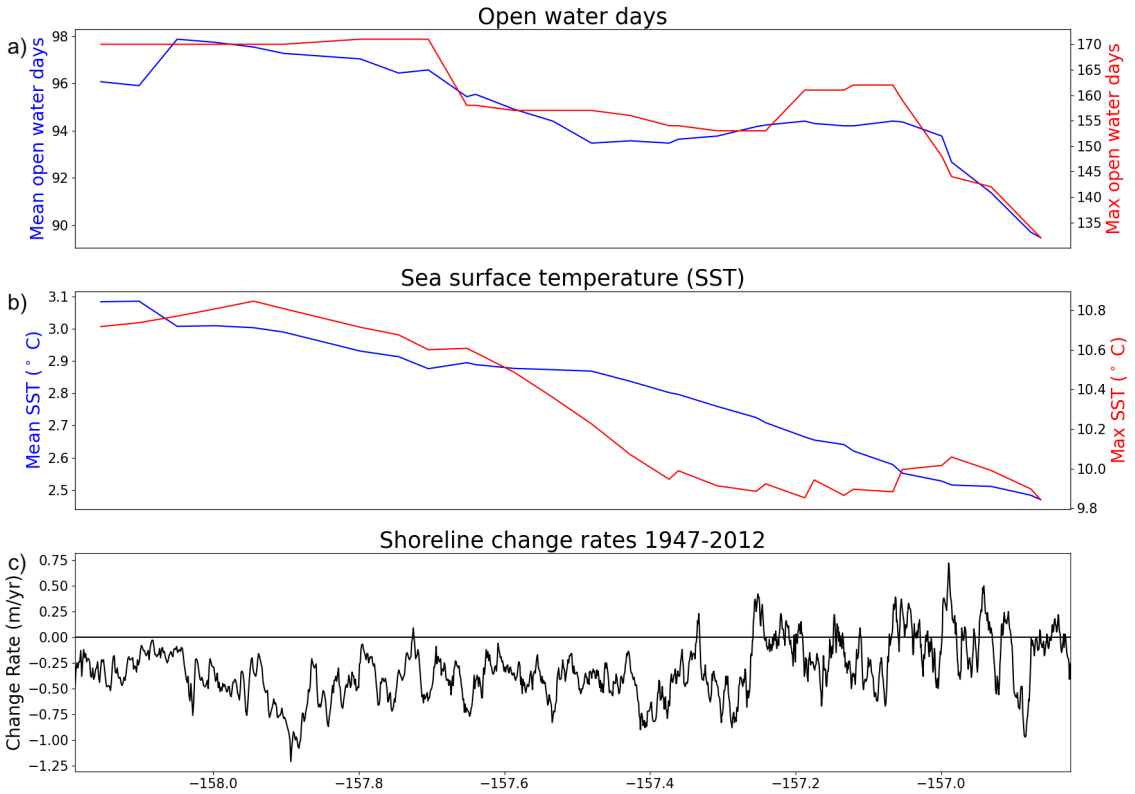


Figure 4.3: Alongshore distribution of 30-year statistics from CARRA2: a) The mean and maximum number of open water days (owd) per year b) The mean and maximum annual sea surface temperature (SST) in the open-water season, and c) USGS shoreline change rates for reference

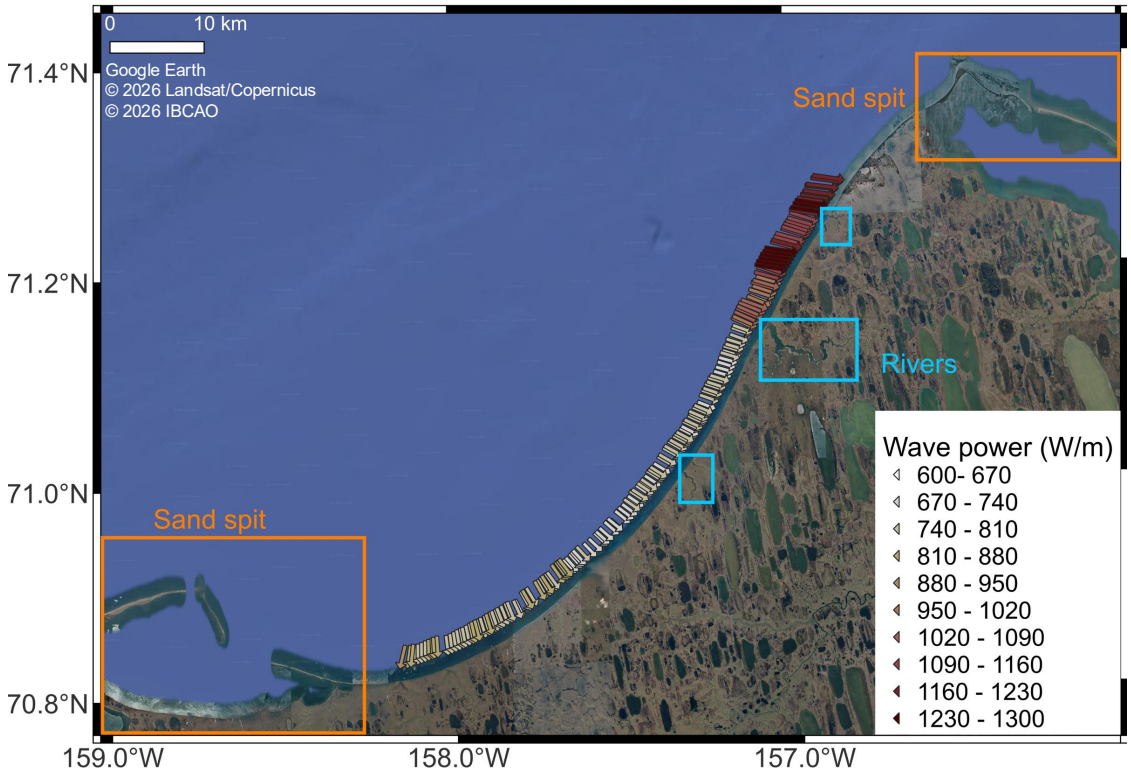


Figure 4.4: The characteristic wave field estimated from the USGS DWDB, plotted according to the 30-year omnidirectional energy and direction of maximum energy. The location of the largest rivers and sand spits along the coastline are indicated.

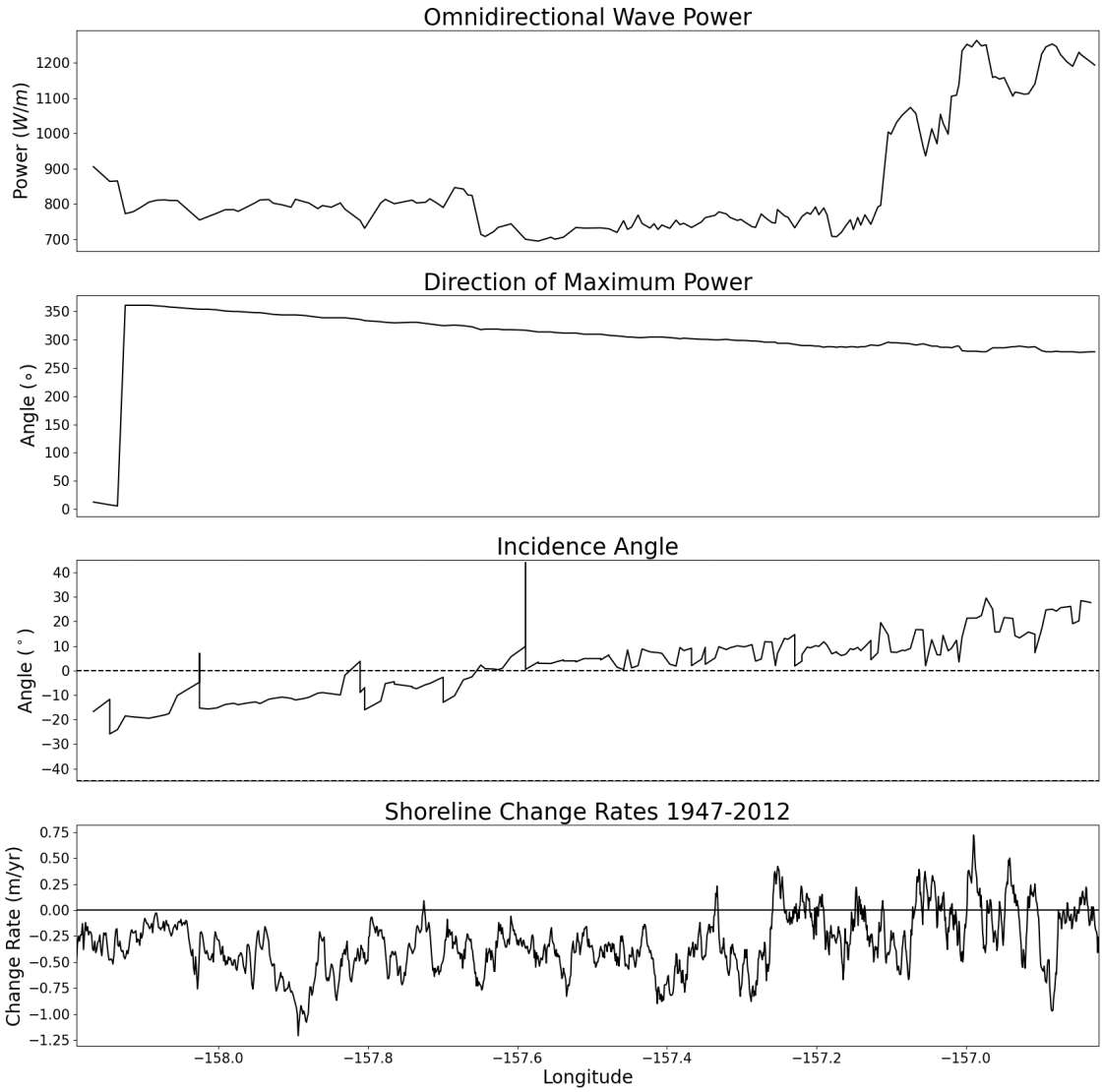


Figure 4.5: Summary of metrics derived from the USGS downscaled wave database: a) Omnidirectional power. b) Direction of maximum wave power θ_{max}, with respect to north. c)Mean incidence angle between θ_{max} and the 5-m isobath, which runs roughly parallel to the shore. d) The shoreline change rates from USGS are plotted for comparison.

northernmost pixel. We note the variation is small, with the mean temperature varying between 2.47 ° C and 3.09 ° C and the max temperature varying from 9.84 ° C and 10.85 ° C across the study area.

Based on the 30-year mean wave power (Figure 4.4 and Figure 4.5 a)), the most energetic waves (with a 30-year omni-directional wave power of up to 1263 W/m) occur in the northeast region, the least energetic waves (with a 30-year omni-directional wave power as low as 695 W/m) occur at intermediate longitudes, and the southwestern region has low-intermediate wave energy values. The mean wave direction (Figure 4.4 and Figure 4.5 b)) and resulting indigence angle with the 5-m isobath (Figure 4.5 c)) vary across the study area, with waves coming from the north in the south and from the southwest in the north. The incidence angle transitions from negative in the south to positive in the north and is closest to shore-normal at intermediate latitudes.

The average summer air temperature and rainfall from DAYMET (Figure 4.6) shows a trend towards warmer and wetter conditions in the southwest. The mean summer air temperature is 0.7 ° C higher at the southernmost point of the study region compared to the northernmost point, while mean annual precipitation is 12.7 mm higher.

4.3.3 Shoreline composition

The composition of both the supratidal and intertidal zones is highly variable, with some large-scale spatial patterns. There are a total of 35 detailed material classes between the two zones, although most of these classes are highly localized, accounting for less than 10% of the shoreline each (Supplementary Figure 4.19). The supratidal zone is primarily clastic in the northeast (Figure 4.7ca)), consisting largely of pebbles, sand and diamicton, or poorly sorted mud and sediment (Figure 4.8 a)). The southwest is primarily biogenic (Figure 4.7ca)), and dominated by organic litter and peat (Figure 4.7a)). While there are short ($\sim$ 10s of m to a few km) segments without visible signs of permafrost, permafrost is largely present across the study area in the supratidal zone (Figure 4.9 a)). The intertidal zone is predominantly clastic (Figure 4.7 b)), with pebbles and sand prevailing in the northeast, and cobbles, pebbles, and sand comprising most of the shoreline in mid

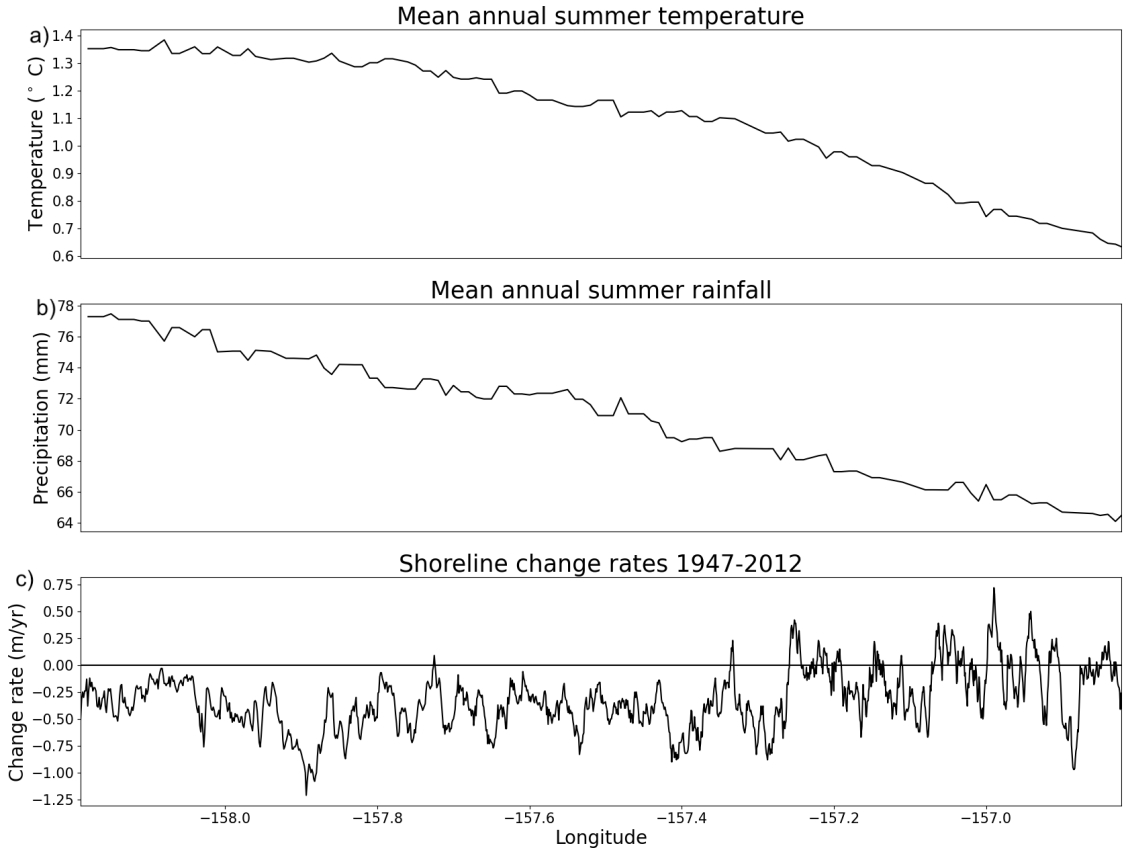


Figure 4.6: Mean summer temperature (a) and rainfall (b) averaged from June 1st-October 31st average over 1980-2010. c) The shoreline change rates are plotted for comparison.

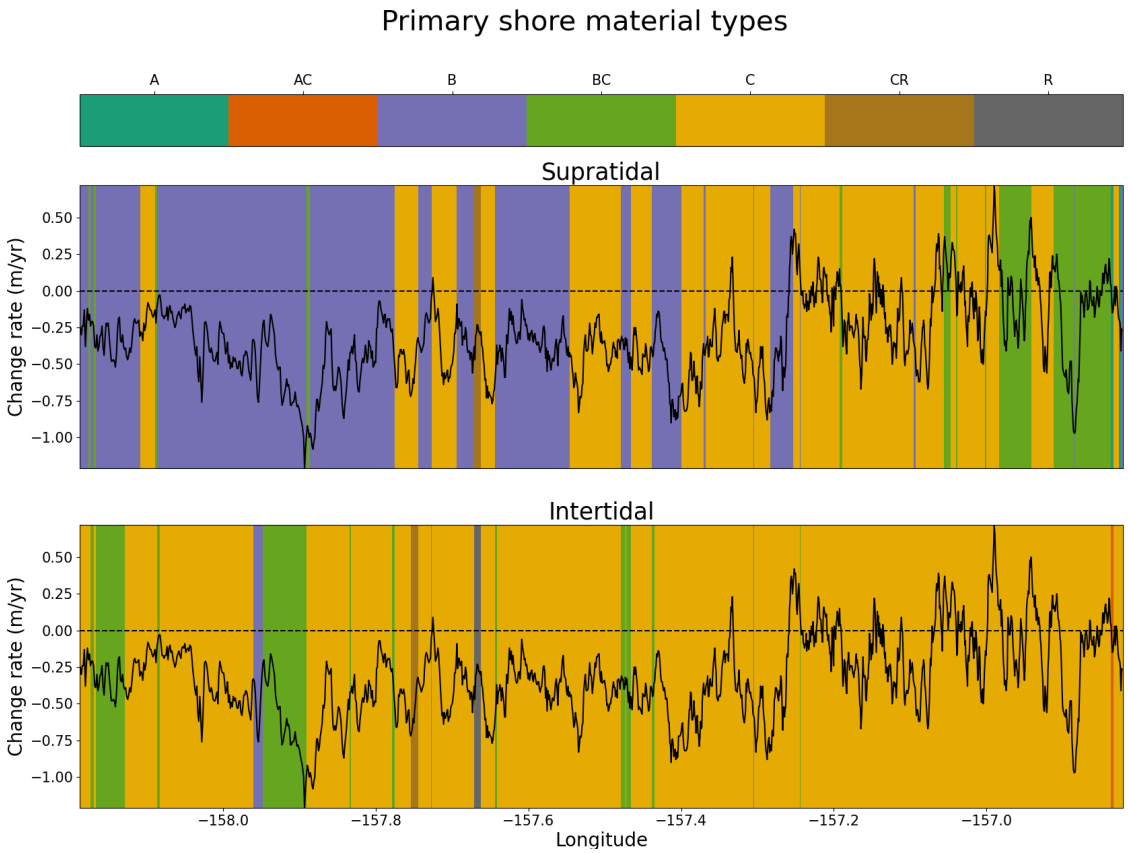


Figure 4.7: The primary material types of a) the supratidal zone and b) the intertidal zone. Historic shoreline change rates from USGS are also plotted for reference.

longitudes (Figure 4.8 b)). The southwest is highly variable, featuring a combination of diamictoms, pebbles, sand, and biogenic materials. Visible permafrost is observed in the southwest, but not in the central and northern portions of the study area (Figure 4.9 b)).

4.3.4 Shoreline change across different shore types

Differences between form classes

Statistical comparisons between Form Class 0 and Form Class 1 reveal different shoreline change patterns across the two shore forms. Transects classified as Form Class 1 (Figure 4.10 b)), the downwards-sloping hydrologic land forms, exhibit more negative shoreline change rates (with a median value of -0.37 m/yr) than transects classified as Form Class 0 (cliff-like features), which have a median change rate of -0.31 m/yr (Figure 4.10 a)). Comparisons of their 95% confidence intervals shows no overlap, and a 2-sample KS test shows that the two sets of samples likely come

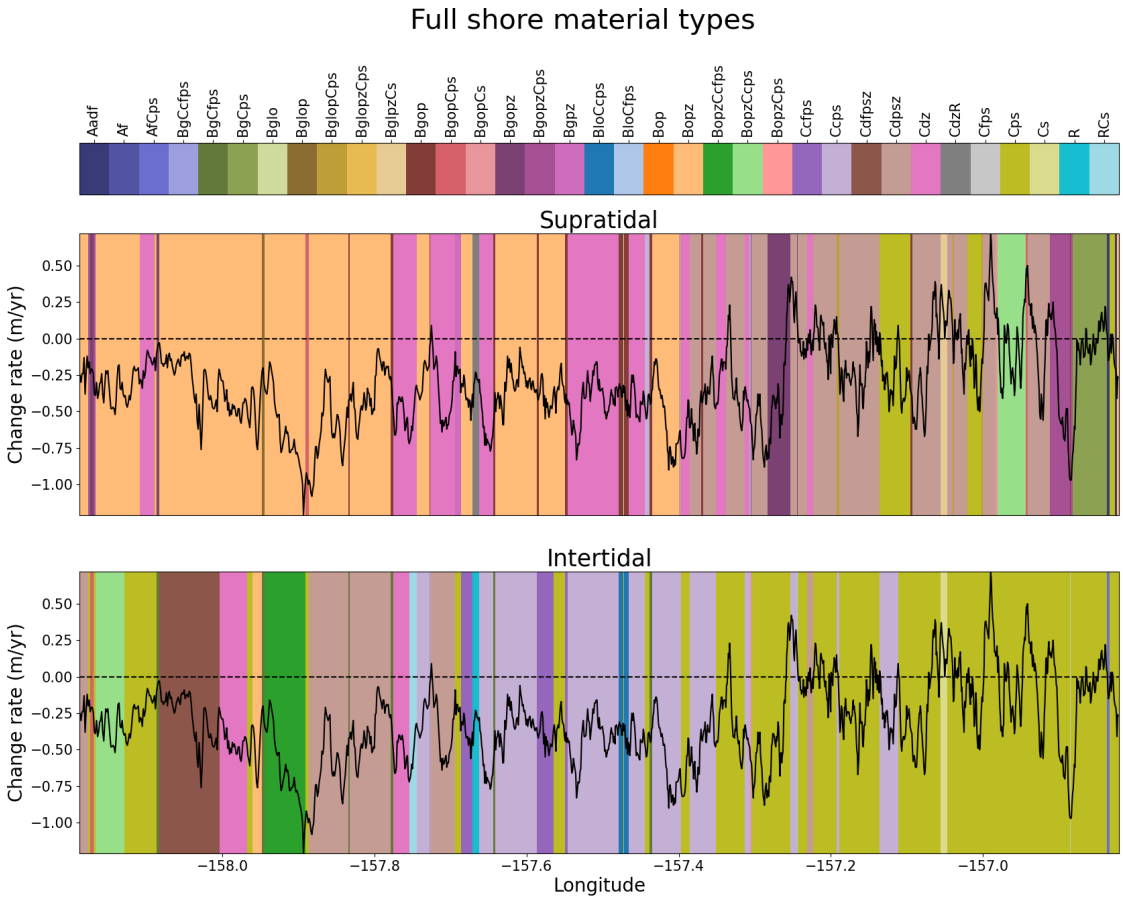


Figure 4.8: The full material types of a) the supratidal zone and b) the intertidal zone. See table 4.2 for the letter code definitions. Historic shoreline change rates from USGS are also plotted for reference.

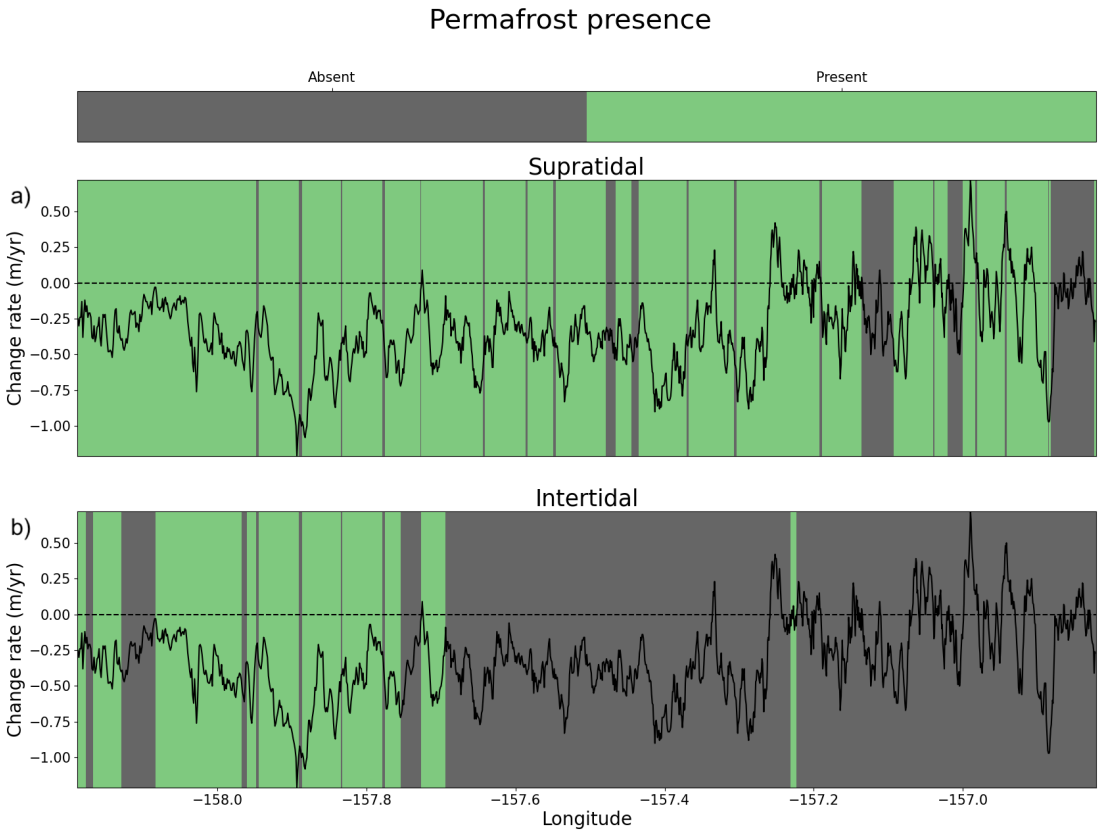


Figure 4.9: Permafrost presence from ShoreZone for a) the supratidal and b) the intertidal zone. Historic shoreline change rates from USGS are also plotted for reference.

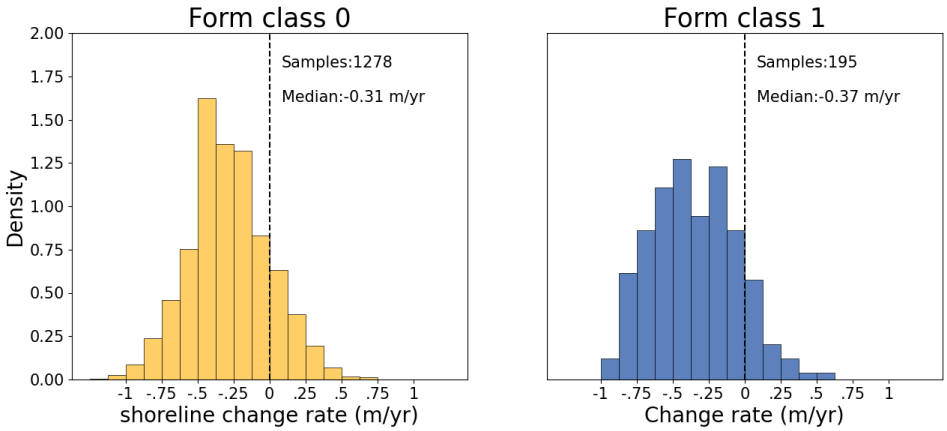


Figure 4.10: The distribution of shoreline change rates for transects classified as a) Form Class 0 and b) Form class 1. The number of sampled transects and median for each class is shown.

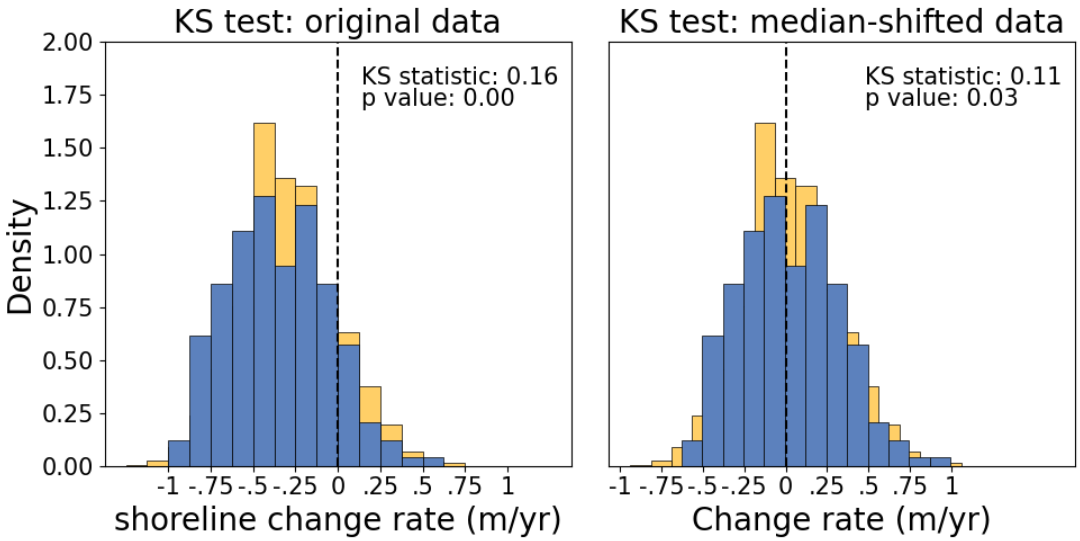


Figure 4.11: Comparisons of the distribution of shoreline change rates across both classes with the KS test statistic and p-value for a) the original distributions and b) the distributions after removing the median.

from two different distributions (KS statistic = .16, p <<.05, Figure 4.11 a)). After centering both distributions around their respective medians (Figure 4.11 b)), the KS-statistic is still significant (p = .03), suggesting that the distribution of shoreline change rates across these two classes differ in terms of their shapes as well as their medians. Form Class 0 has a higher range of shoreline change values (-1.1 m/yr to 0.72 m/yr), but is more densely distributed around the median, while Form Class 1 has a higher proportion of transects with high (> -.5 m/yr) shoreline change.

Differences between parameter classes

Our parameter classes show a wide variance in the median (Figure 4.12 b)) and apparent shapes (Figure 4.13) of their distributions. Based on our comparison of the medians and our KS tests, we come to the following conclusions:

1. Parameter Classes 02 and 11 (the wide shorelines) have significantly smaller median change rates (-.01 m/yr) than all other parameter classes, but do not differ significantly from each other in terms of their median (21p = 14.1; Figure 4.12 b), Figure 4.14) or shape (21p = 14.1; Figure 4.15).

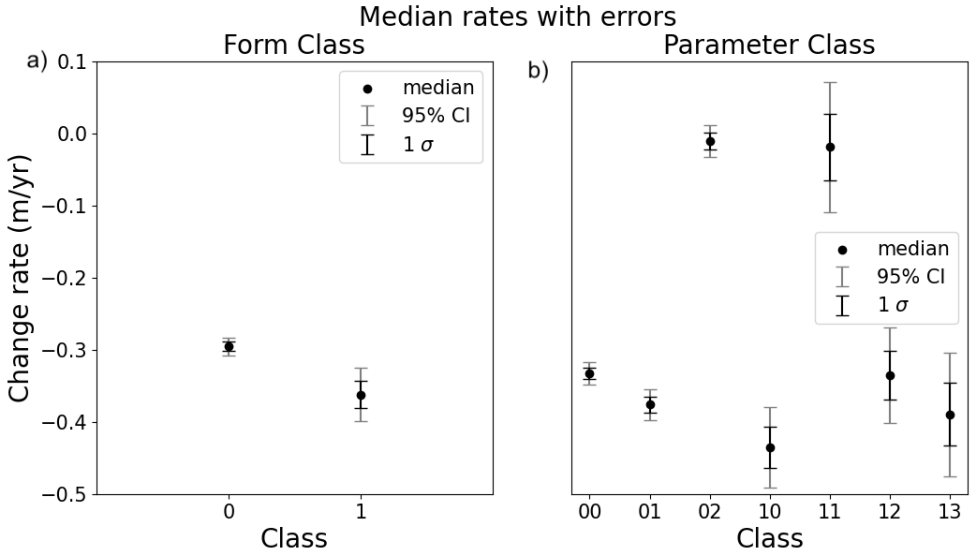


Figure 4.12: The estimated median shoreline change rates and their propagated uncertainties for a) The form classes and b) the parameter classes. The standard deviation (σ) and 95% confidence interval are shown.

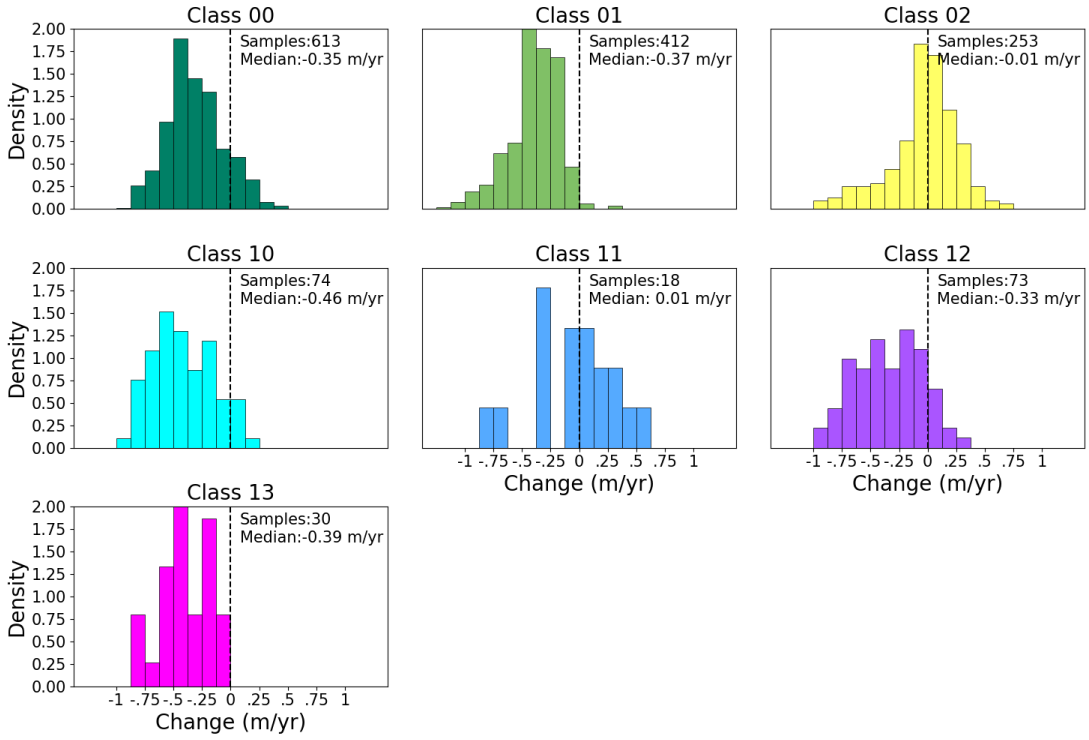


Figure 4.13: Shoreline change rate distributions across our parameter classes. The number of sampled transects and median for each class is shown.

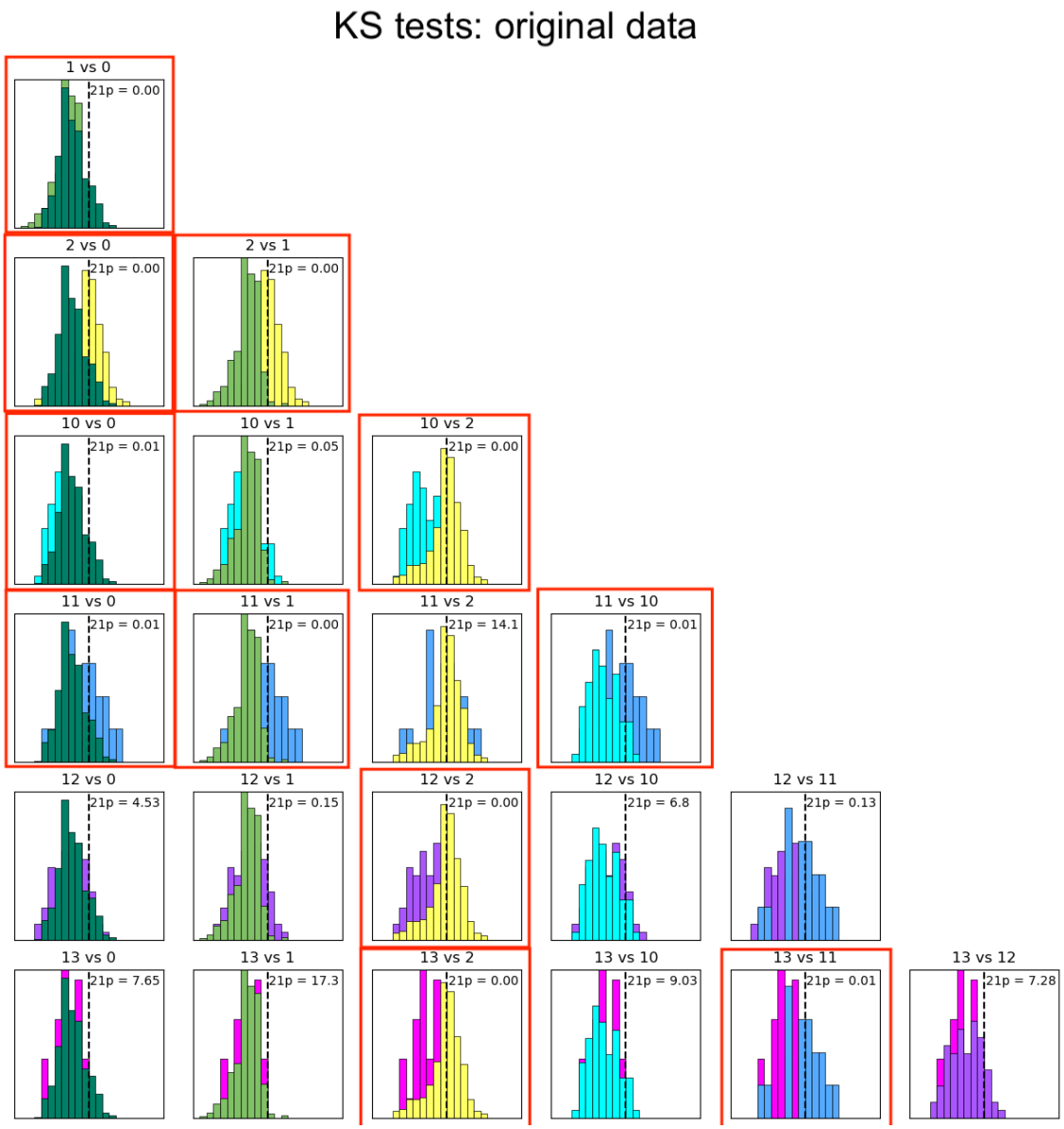


Figure 4.14: Pairwise comparisons of shoreline change rates between different parameter classes. The p-value from a 2-sample KS test (modified using Bonferroni correction) is shown. Pairs with significantly low p-values are highlighted.

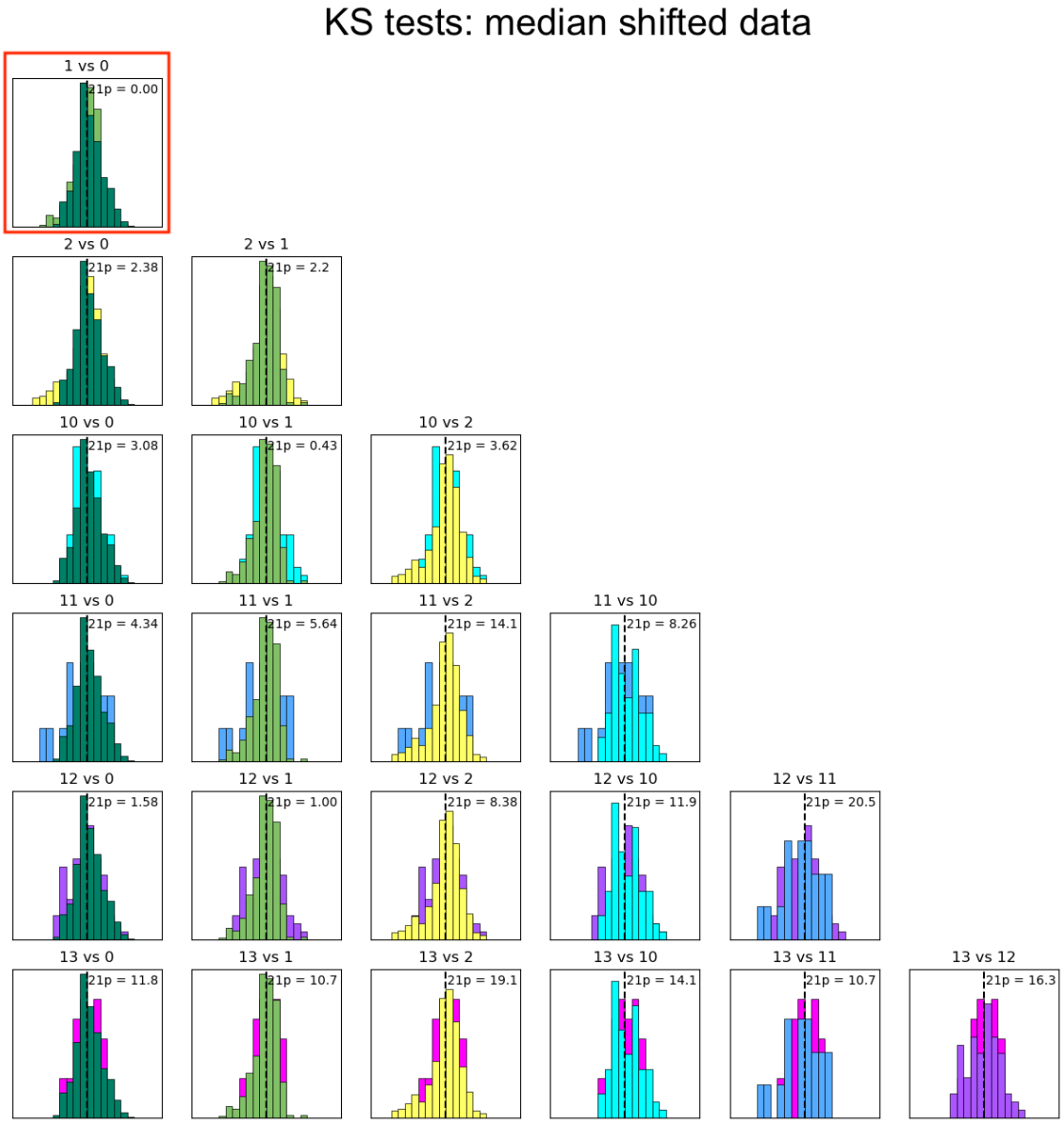


Figure 4.15: Pairwise comparisons of shoreline change rates between different parameter classes after removing their medians. The p-value from a 2-sample KS test (modified using Bonferroni correction) is shown. The one pair with a modified p-value $<.05$ is highlighted.

2. Parameter Classes 00 (low-intermediate cliffs) and 01 (high cliffs) have significantly differently median change rates (Figure 4.12 b), Figure 4.14), with high cliffs retreating more rapidly (-.37 m/yr) than lower cliffs (-0.35 m/yr). Their distributions also have different shapes, with change rates in Parameter Class 01 skewing more negative than 00 ($21p << 0$; Figure 4.13, Figure 4.15).

3. While Parameter Class 13 (high cliffs with drainage channels) has a larger median shoreline change rate (-.39 m/yr) than Parameter Class 12 (low-intermediate cliffs with drainage channels), there is significant overlap in the 95% confidence intervals on their medians (Figure 4.12 b)), and the KS tests between their unshifted ($21p = 7.28$) and shifted distributions ($21p = 16.3$) are not statistically significant.

4. While Parameter Class 10 (river mouths) has the largest median retreat (-0.46 m/yr), it is only significantly higher (in terms of the 95% confidence interval and KS tests) than Parameter Classes 00, 02, and 11. The shape of its distribution does not significantly differ from any other parameter class (Figure 4.15).

4.4 Discussion

4.4.1 Meteorological drivers of large-scale variations in shoreline change

The shoreline is subject to spatially variable air and ocean conditions that likely impact shoreline change rates. More open water days and higher ocean temperatures (Figure 4.3) may contribute to higher retreat rates in the southeast compared to the northwest as the increased exposure of the shoreline to warmer water can lead to increased thawing of the beach and cliff base. While these differences are small, the cumulative impact over decadal time scales could be significant. The presence of visible nearshore permafrost in the intertidal zone in the southwest may mean that the southwest is more susceptible to thermal abrasion than further east. However, we note that the transition from visible permafrost presence to no visible presence does not correspond to an along-shore shift in shoreline change rates (Figure 4.9 b)), meaning that intertidal permafrost presence alone can't explain the observed spatial patterns.

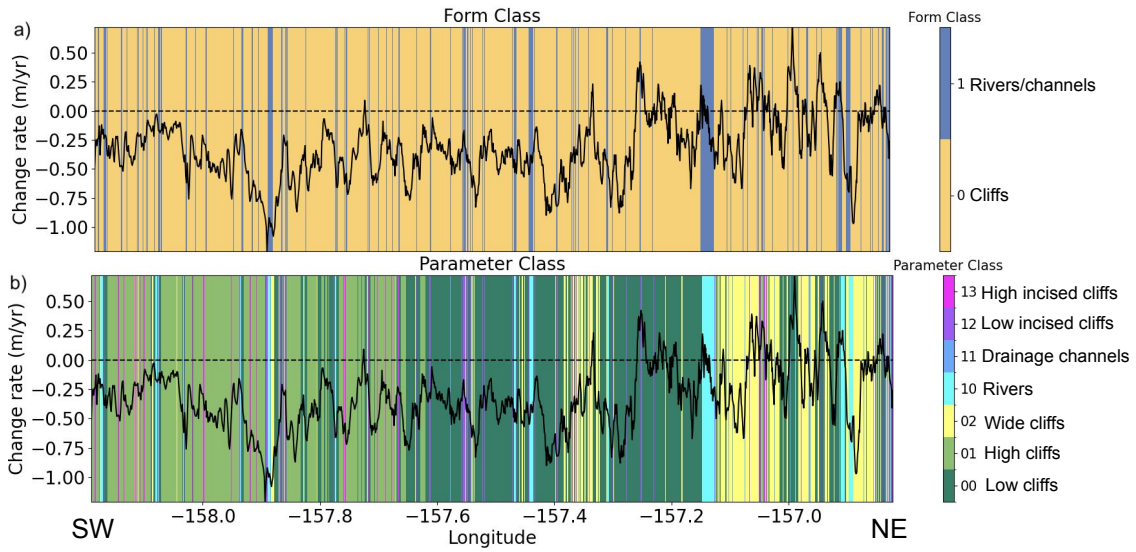


Figure 4.16: Along-shore shoreline change rates overlain over our a) form classes and b) parameter classes.

The impact of waves on the shoreline is less straightforward. While we would expect more energetic waves to correspond to higher retreat, we observe lower retreat and some accumulation in the northeast where wave power is the highest (Figure 4.5). There are a few reasons why this may occur. First of all, the decrease in open water days in the northeast relative to the southwest means that, while the shoreline is exposed to more energetic waves, it is exposed less often, such that the cumulative energy acting on the shoreline is lower. Beach shoreline change rates are also dependent on sediment grain size (Kriebel and Dean, 1985), so the heterogeneous intertidal composition (Figure 4.8 b)) may contribute to a varying rates of retreat and long-shore transport that offset differences in wave energy. Finally, the wide rivers present in the northeast (as can be seen in the satellite imagery in Figure 4.4 and Parameter Class 10 in Figure 4.16) likely provide additional sediment (Tian et al., 2026) that could nourish beaches locally. The oblique incidence angles of incoming waves may drive northwards along-shore transport, nourishing the local beaches as well as the large spit north of the study area (Figure 4.4). The oblique angle in the southwest and presence of a spit south of the site (Figure 4.4) suggest that there may be southwards sediment transport in the southwest portion of our study site, but there are fewer rivers to provide shoreline nourishment and offset losses from erosion.

Spatial patterns in shoreline retreat are also likely driven by atmospheric variations. Warm air and precipitation can both transfer heat into the soil, leading to an increase in the seasonal top-down thaw depth. Thawing of the upper layer of the shoreline can lead to retreat of the back shore via slumping and wind-driven erosion (Günther et al., 2013; Rolph et al., 2022) and the transfer of sediment from the backshore to the beach. Soil thaw depth also effects the rate of retreat due to oceanic conditions by impacting the convective heat transfer across the backshore. Rolph et al. (2022) model the retreat rate $\frac{\partial R}{\partial t}$ of cliffs exposed to seawater as dependent on the overall cliff height H and the thaw depth B_C:

$$\frac{\partial R}{\partial t} \propto \frac{1}{H - B_C} \tag{4.10}$$

Thus, for a given cliff height, an increased thaw depth, driven by increased air temperatures and precipitation, will lead to increased rates of retreat. However, we note that the spatial variations in the composition of the supratidal zone (Figure 4.7 a), Figure 4.8 a)) will also affect the porosity and thermal conductivity of the soil, which will in turn impact the thaw depth. A more in-depth analysis of the soil composition would be needed to properly resolve spatial variations in seasonal thaw depths.

4.4.2 Variations in shoreline change rates between topographic classes

Our analysis suggests that transects classified as Form Class 1, corresponding to river mouths and drainage channels, have retreated at a higher rate than transects classified as Form Class 0, our cliff-like class. This difference is not consistent with the large-scale north-south distribution of shoreline change rates, as both form classes are present along the full length of the shoreline, and Form Class 1 is more common in the northeast, where there is less retreat and more accumulation (Figure 4.16 a)). Therefore, the difference in change rates between these two classes can not be explained solely by spatial variations in meteorological conditions, and is likely in part due to different physical processes occurring across these different landforms. While it is expected that there is inland sediment supply from rivers, it may be that this sediment is transported alongshore

rather than accumulating at the river mouths, leading to less net erosion at surrounding cliffs and beaches relative to the river mouths (Parameter Class 10). While we might expect drainage channels to increase the local thaw depth and therefore contribute to higher retreat rates, the medians (Figure 4.12) and distributions (Figure 4.14) of our cliffs intersected by drainage channels (Parameter Class 12 and Parameter Class 13) are comparable to their non-incised counterparts (Parameter Class 0 and Parameters Class 1). We therefore conclude that the difference between shoreline change rates in Form Cluster 0 and Form Cluster 1 is primarily driven by increased rates across active river mouths, and that there is not evidence of small drainage channels impacting shoreline retreat rates.

Comparisons between parameter classes show some difference between shore forms of different heights and widths. The low retreat rates and high advancement rates of our wide parameter classes 02 (Figure 4.13 c) and 11 (Figure 4.13 e) is expected, as these profiles are likely wide as a results of sediment accumulation or lack of erosion over the 65-year measurement period. Parameter Class 02 is located primarily in the northeast, where average retreats rates are lower and where sediment supply from rivers is likely higher. It may be that these areas are local hotspots of accretion from along-shore transport.

We also find that high cliffs (Parameter Class 01) have significantly more retreat than low-intermediate cliffs (Parameter Class 00). This is contrary to what we would expect based on 4.10, which models retreat as inversely proportional to cliff height. It may be that the increase in height in the southwest is offset by the higher air and ocean temperatures and precipitation. It is difficult to attribute the difference between high and low cliffs to their shore form specifically, as they occur in different locations, meaning that they are subject to different external forcings and have different material compositions that could also influence shoreline change rates. While high cliffs with drainage channels (Parameter Class 13) similarly have a higher median retreat rate than lower cliffs with drainage channels, the high overlaps in their 95% confidence intervals (Figure 4.12) and lack of significant KS test results (Figure 4.14, Figure 4.15) means that we can not confidently conclude that there is a significant difference in channel-incised cliffs of different heights. It may be that the sediment types and ground ice conditions around drained channels are different than undisturbed

tundra.

Our lack of significant differences between certain parameter classes pairings may be in part due to low and uneven sampling rates. While all of our parameters classes associated with Form Class 0 have a large number of samples (ranging from 253-613 samples per class, Figure 4.13 a-c), We have fewer samples (74 or less, Figure 4.13 d-g) for our Form Class 1 parameter classes. Parameter Class 11 and Parameter Class 13 are particularly poorly sampled, with only 18 and 30 samples respectively. This low number of samples leads to high errors on the estimated median shoreline change rates of these classes, and means we may not have enough samples to accurately represent the underlying distribution of change rates across these features. As discussed in Section 3.4.2, small drainage channels are under sampled due to their narrow along-shore widths and our along-shore filtering. Resampling our 10m classification dataset to the 50m spacing of the USGS retreat rates exacerbates this under sampling. Obtaining a better representation of these small-scale features would require an improved classification method, a large study area, or a higher-resolution shoreline change dataset.

4.5 Conclusion

By jointly comparing retreat rates, ocean and atmospheric data, sediment data, and topographic shore types across the Chukchi Sea coast, we were able to analyze how shoreline change depends on both meteorological and morphologic drivers. The large-scale trend of more advancement in the northeast and more retreat in the southwest is broadly consistent with warmer temperatures, higher precipitation, and more open water days in the southwest and cooler, drier conditions coupled with higher sediment supply in the northeast. Trends in shoreline change, meteorological conditions, and shoreline composition are coupled with a trend of wider, shorter shore forms in the northeast and higher, narrower forms in the southwest. We hypothesize that that the wide, more stable portions of the shoreline in the northeast are due to the alongshore transport of sediment from rivers. Beaches in front of rivers tend to erode faster than cliffs, possibly due to along-shore transport patterns. We observe higher rates of retreat among tall cliffs than

lower cliffs, but it is hard to determine if this is due to physical differences in the shore types or spatial differences in meteorological forcings and shoreline composition. No other significant differences were found between other parameter classes. We note that our analysis is limited by the low sampling rate of more localized shore types and our inability to separate the impacts of spatial variability in meteorological conditions, shoreline composition, and topographic shore type. In order to isolate the impacts of shoreline morphology, future work should either focus on a study area where conditions are more uniform, or take a more comprehensive approached to jointly estimate the impacts of meteorological forcings, morphology, and sediment composition on shoreline change.

4.6 Acknowledgments

This work was supported by NASA grant no. 80NSSC24K0019. This work is based on unpublished research done in collaboration with A. Borsa and A. Young. The dissertation author was the primary researcher on this project.

4.7 Supplementary material

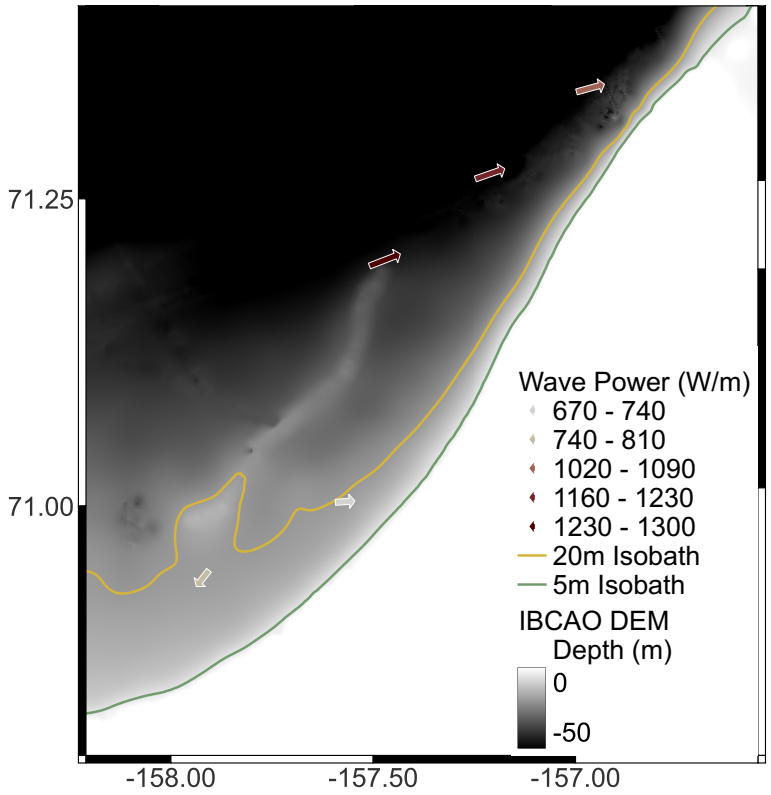


Figure 4.17: Inputs used for the USGS Downscaled Wave Database. Wave data from CMIP-6 (represented here in terms of their aggregated omnidirectional power and direction of maximum energy) and bathymetry from IBCAO are used as inputs for SWAN, which generates waves at the 20-m isobath and propagates them to the 5-m isobath

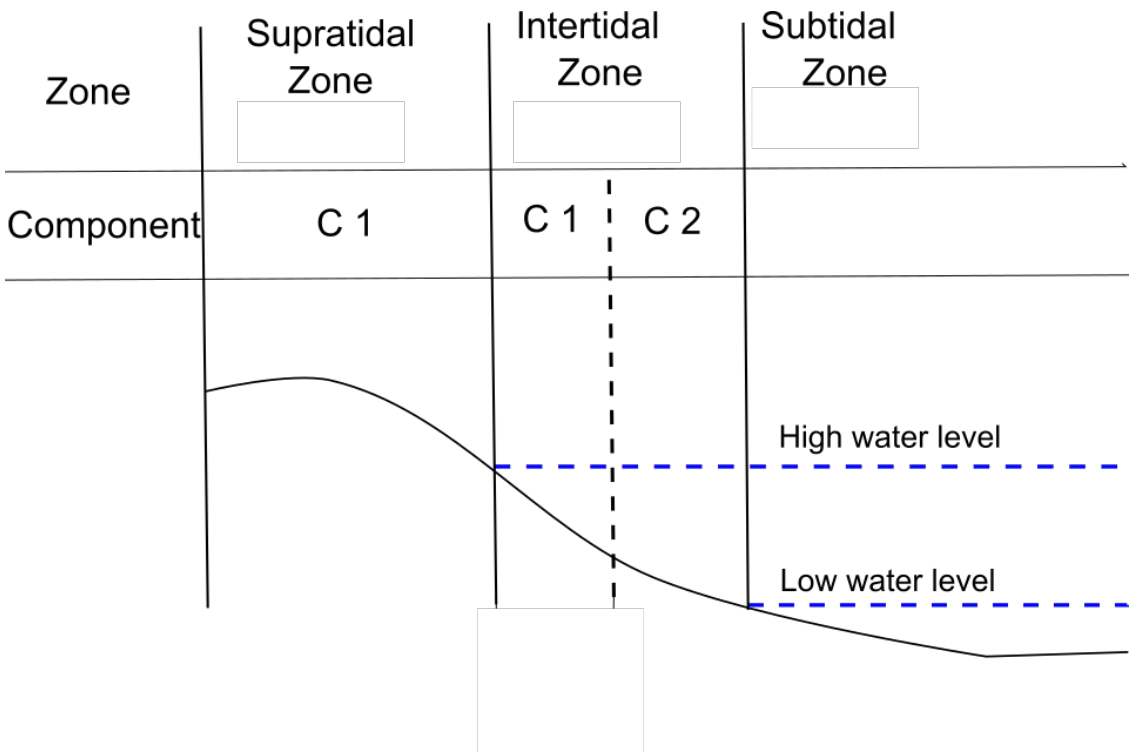


Figure 4.18: An overview of the cross-shore segmentation from ShoreZone

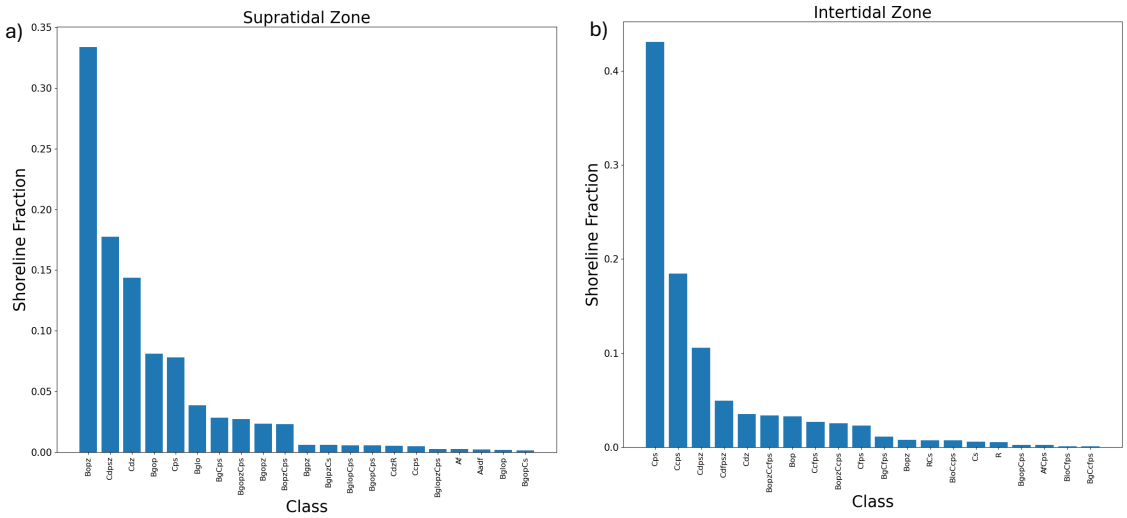


Figure 4.19: The relative fraction of the shoreline that is composed of each sediment class in a) the supratidal zone and b) the intertidal zone.

References

Ahn, S., Neary, V. S., and Ha, T. (2023). A practical method for modeling temporally-averaged ocean wave frequency-directional spectra for characterizing wave energy climates. *Renewable Energy*, 207:499–511.

Aré, F. E. (1988). Thermal abrasion of sea coasts (part I). *Polar Geography and Geology*, 12(1):1–1.

Baranskaya, A., Novikova, A., Shabanova, N., Belova, N., Maznev, S., Ogorodov, S., and Jones, B. M. (2021). The Role of Thermal Denudation in Erosion of Ice-Rich Permafrost Coasts in an Enclosed Bay (Gulf of Kruzenstern, Western Yamal, Russia). *Frontiers in Earth Science*, 8.

Booij, N., Ris, R. C., and Holthuijsen, L. H. (1999). A third-generation wave model for coastal regions: 1. Model description and validation. *Journal of Geophysical Research: Oceans*, 104(C4):7649–7666.

Dingemans, M. W. (1997). *Water Wave Propagation over Uneven Bottoms*, volume 13 of *Advanced Series on Ocean Engineering*. World Scientific Publishing Company.

Engelstad, A. C., Erikson, L. H., Reguero, B. G., Gibbs, A. E., and Nederhoff, K. (2024a). Database and Time Series of Nearshore Waves Along the Alaskan Coast from the United States-Canada Border to the Bering Sea. Open-File Report 2023-1094, U.S. Geological Survey.

Engelstad, A. C., Erikson, L. H., Reguero, B. G., Gibbs, A. E., and Nederhoff, K. (2024b). Nearshore wave time-series along the coast of Alaska computed with a numerical wave model. U.S. Geological Survey data release, https://doi.org/10.5066/P931CSO9.

Farquharson, L., Mann, D., Swanson, D., Jones, B., Buzard, R., and Jordan, J. (2018). Temporal and spatial variability in coastline response to declining sea-ice in northwest Alaska. *Marine Geology*, 404:71–83.

Gibbs, A. E., Ohman, K. A., Coppersmith, R., and Richmond, B. M. (2024). National Assessment of Shoreline Change: A GIS compilation of updated vector shorelines and associated shoreline change data for the north coast of Alaska, U.S. Canadian border to Icy Cape (ver. 2.0, September 2024).

Gibbs, A. E. and Richmond, B. M. (2015). National assessment of shoreline change—Historical shoreline change along the north coast of Alaska, U.S.–Canadian border to Icy Cape. Open-File Report, U.S. Geological Survey.

Gibbs, A. E. and Richmond, B. M. (2017). National Assessment of Shoreline Change—Summary Statistics for Updated Vector Shorelines and Associated Shoreline Change Data for the North Coast of Alaska, U.S.-Canadian Border to Icy Cape. Open-File Report, US Geological Survey.

Günther, F., Overduin, P. P., Sandakov, A. V., Grosse, G., and Grigoriev, M. N. (2013). Short- and long-term thermo-erosion of ice-rich permafrost coasts in the Laptev Sea region. *Biogeosciences*, 10(6):4297–4318.

Harper, J. and Morris, M. C. (2014). Alaska ShoreZone Coastal Habitat Mapping Protocol. Technical Report, Nuka Research and Planning Group, LL.

Irrgang, A. M., Lantuit, H., Manson, G. K., Günther, F., Grosse, G., and Overduin, P. P. (2018). Variability in Rates of Coastal Change Along the Yukon Coast, 1951 to 2015. *Journal of Geophysical Research: Earth Surface*, 123(4):779–800.

Jakobsson, M., Mohammad, R., Karlsson, M., Salas-Romero, S., Vacek, F., Heinze, F., Bringensparr, C., Castro, C. F., Johnson, P., Kinney, J., Cardigos, S., Bogonko, M., Accettella, D., Amblas, D., An, L., Bohan, A., Brandt, A., Bünz, S., Canals, M., Casamor, J. L., Coakley, B., Cornish, N., Danielson, S., Demarte, M., Di Franco, D., Dickson, M.-L., Dorschel, B., Dowdeswell, J. A., Dreutter, S., Fremand, A. C., Hall, J. K., Hally, B., Holland, D., Hong, J. K., Ivaldi, R., Knutz, P. C., Krawczyk, D. W., Kristofferson, Y., Lastras, G., Leck, C., Lucchi, R. G., Masetti, G., Morlighem, M., Muchowski, J., Nielsen, T., Noormets, R., Plaza-Faverola, A., Prescott, M. M., Purser, A., Rasmussen, T. L., Rebesco, M., Rignot, E., Rysgaard, S., Silyakova, A., Snoeijs-Leijonmalm, P., Sørensen, A., Straneo, F., Sutherland, D. A., Tate, A. J., Travaglini, P., Trenholm, N., Van Wijk, E., Wallace, L., Willis, J. K., Wood, M., Zimmermann, M., Zinglersen, K. B., and Mayer, L. (2024). The International Bathymetric Chart of the Arctic Ocean Version 5.0. *Scientific Data*, 11(1):1420.

Kriebel, D. L. and Dean, R. G. (1985). Numerical simulation of time-dependent beach and dune erosion. *Coastal Engineering*, 9(3):221–245.

Overeem, I., Anderson, R. S., Wobus, C. W., Clow, G. D., Urban, F. E., and Matell, N. (2011). Sea ice loss enhances wave action at the Arctic coast: Sea ice loss enhances erosion. *Geophysical Research Letters*, 38(17).

Pelt, S., Støylen, E., Schyberg, H., Yang, X., Dahlgren, P., Ødegaard Køltzow, M., Bojarova, J., Nielsen, K., and Peralta, C. (2025). Pan-Arctic regional reanalysis daily and monthly data from 1986 to present. Copernicus Climate Change Service (C3S) Climate Data Store (CDS). Accessed 2026-08-05.

Piliouras, A., Jones, B. M., Clevenger, T., Gibbs, A. E., and Rowland, J. C. (2023). Variability in terrestrial characteristics and erosion rates on the Alaskan Beaufort Sea coast. *Environmental Research Letters*, 18(11).

Rolph, R., Overduin, P. P., Ravens, T., Lantuit, H., and Langer, M. (2022). ArcticBeach v1.0: A physics-based parameterization of pan-Arctic coastline erosion. *Frontiers in Earth Science*, 10.

Scoccimarro, E., Bellucci, A., and Peano, D. (2017). CMCC CMCC-CM2-VHR4 model output prepared for CMIP6 HighResMIP. Earth System Grid Federation. 10.22033/ESGF/CMIP6.1367.

Thornton, M. and Devarakonda, R. (2011). Daymet Single Pixel Extraction Tool. ORNL DAAC. 10.3334/ORNLDAAC/2361.

Thornton, M., Shrestha, R., Wei, Y., Thornton, P., and Kao, S.-C. (2022). Daymet: Daily Surface Weather Data on a 1-km Grid for North America, Version 4 R1 (Version 4.1). ORNL Distributed Active Archive Center. 10.3334/ORNLDAAC/2129.

Tian, S., Li, D., Zhang, T., McClelland, J. W., Overeem, I., Lane, S. N., Spencer, R. G. M., Wohl, E., Sha, A., Zhao, Y., Miao, C., Ning, M., Yuan, L., and Ni, J. (2026). Increasing river sediment concentration and flux across the pan-Arctic. *Nature Geoscience*.

Zwieback, S., Kokelj, S. V., Günther, F., Boike, J., Grosse, G., and Hajnsek, I. (2018). Sub-seasonal thaw slump mass wasting is not consistently energy limited at the landscape scale. *The Cryosphere*, 12(2):549–564.

Chapter 5

Conclusions

5.1 Summary of findings

We have utilized both airborne and spaceborne lidar in tandem with satellite imagery, aerial photography, and a suite of environmental datasets to highlight diverse patterns of shoreline change over both the Alaskan Beaufort Sea coast (Chapter 2) and the Western Chukchi Sea coast (Chapter 4). In Chapter 2, we found that different topographic shore types on the Beaufort Sea Coast showed different patterns of shoreline change over a 3-year period, illustrating the potential importance of morphology in controlling local, short-term retreat. We also established that ICESat-2 can be used to capture these short-term dynamics and estimate retreat rates that are comparable to those obtained from satellite imagery. In Chapter 3, we developed a method to systematically classify cross-shore elevation profiles into different shore types based on k-means clustering of both their shape and dimensions, and demonstrated that these classes represent physically meaningful differences in shore types. In Chapter 4, we compared historic retreat rates across the different classes derived in Chapter 3 along with spatial patterns in sea ice coverage, air and ocean temperatures, precipitation, and shoreline composition. We found that between 1947 and 2012 river channels retreated at a higher rate than cliffs, wide classes were the most stable, and that higher cliffs retreated at a higher rate than lower cliffs. However, it is challenging to isolate the importance of our topographic classes in determining retreat given that the meteorological and sedimentary conditions are also highly variable across our study area. More research is needed that considers morphology jointly with

other drivers of shoreline change.

5.2 Looking forward: large-scale morphologic monitoring from space

While Chapters 3 and 4 focused on a one-time characterization of shore types and shoreline change with airborne lidar, these methods can be expanded on to track shoreline evolution over time using satellite elevation datasets. Regular repeat monitoring will allow us to not only track shoreline change rates, but to identify areas of both short and long-term morphologic transitions, and identify the impact these transitions have on shoreline change rates. Chapter 2 used ICESat-2 to demonstrate that it is feasible to quantify and monitor shoreline morphology from space. However, there are large gaps in the ground coverage between ICESat-2 beams, limiting the potential for ICESat-2 to provide true pan-Arctic morphology estimates. The upcoming NASA Earth Dynamics Geodetic Explorer mission (EDGE) will address these limitations by providing elevation measurements with comparable vertical accuracy ($\sim$ 8 cm on low slopes) and greater ground coverage. EDGE will use 5 120-m 'miniswaths' to provide more continuous ground coverage, especially at high latitudes. Even when operating in an off-pointing mode, there will be overlap between swaths from different cycles over the Alaskan coastline, as shown in Figure 5.1. Thus, EDGE will facilitate regular, repeat measurements of shoreline morphology and change over much large areas than is possible with ICESat-2. In order to utilize observations from EDGE and other satellite missions, the classification scheme introduced in Chapter 3 should be tested on a variety of airborne and satellite-based datasets to understand the impact of varying resolution, revisit times, ground conditions, and data sources on our ability to accurately identify different shore types.

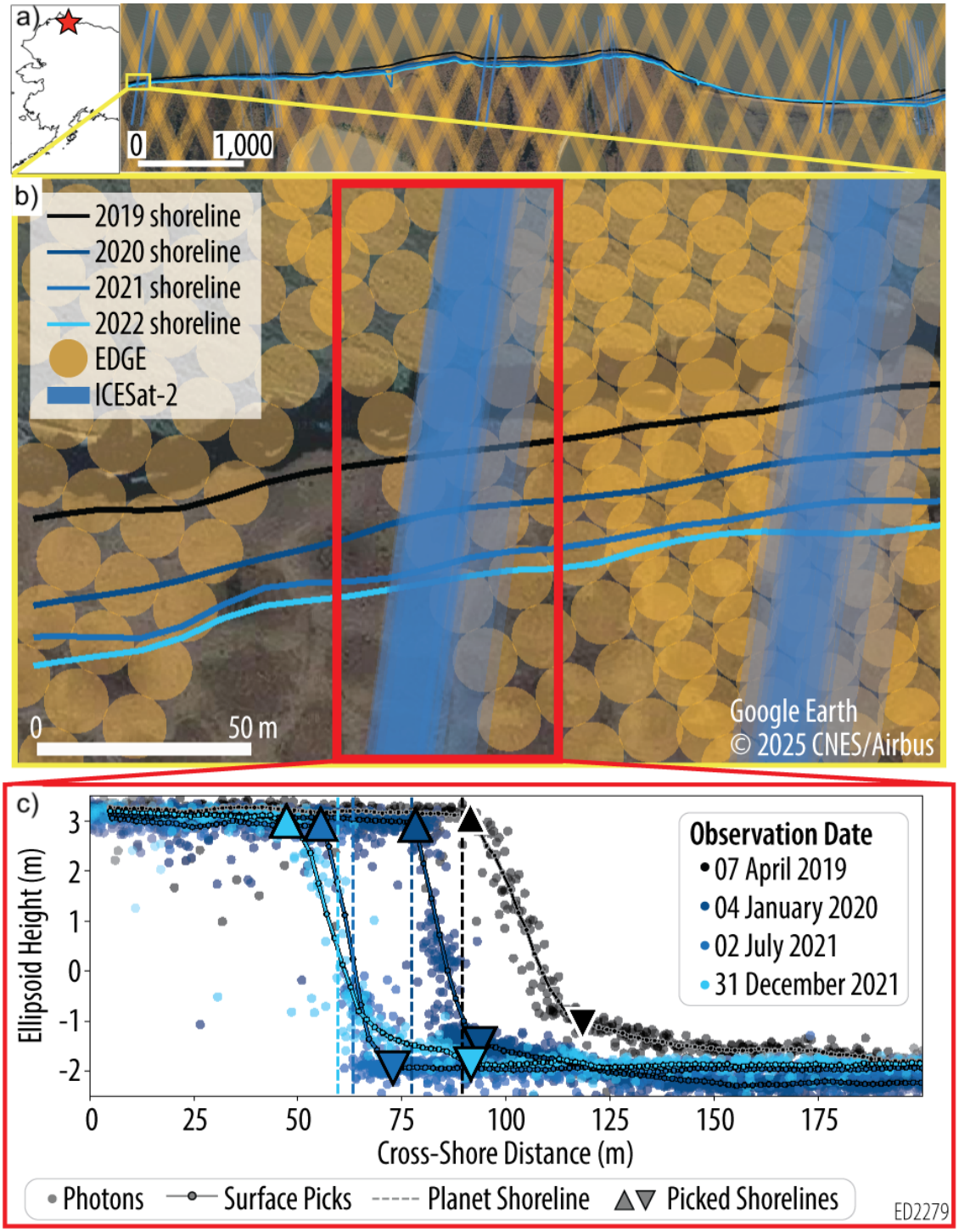


Figure 5.1: EDGE's dense sampling transforms observations of permafrost-driven shoreline erosion events, offering new insight into the processes behind these high-impact, episodic events. a) An overview of the study area from Chapter 2, with the 3-year ground coverage of ICESat-2 and EDGE shown for comparison. b) A close-up of a single repeated ICESat-2 track (ground track 3r from chapter 2), again with EDGE coverage for comparison. c) Coastal cliff retreat observed with ICESat-2, demonstrating the short-term change that can be observed more frequently with EDGE. Originally produced for the EDGE Concept Study Report.

5.3 Closing remarks

In this dissertation, I have established the potential for remotely sensed elevation data to be used to classify shoreline morphology and monitor shoreline change over time. Over small areas and short time intervals, as covered in Chapter 2, we observed distinct differences in shoreline change between different shoretypes. Over large areas and long time intervals, as covered in Chapter 4, understanding shoreline change across different shore types required accounting for other factors, such as spatial variations in environmental forcings and material composition. It's important to note that the topographic classes defined here are not intended to provide a comprehensive description of the shoreline, but to help quantify one aspect (the topographic shape) in a way that can be integrated with other datasets to provide a more complete picture of shoreline vulnerability and improve our ability to understand and predict shoreline evolution in a changing Arctic.